POLITECNICO DI MILANO

Scuola di Ingegneria Industriale e dell'Informazione

Corso di Laurea Magistrale in Automation and Control Engineering

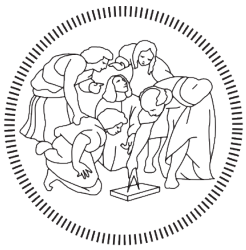

POLITECNICO
MILANO 1863

INTERIOR PERMANENT MAGNET MOTORS: SENSORLESS CONTROL

Relatore: Prof. Ferdinando MAPELLI

Correlatrice: Ing. Maria Laura BACCI

Tesi di Laurea Magistrale di:

Stefano MOSSINA

Matr. 883653

Anno Accademico 2017–2018

"Se insisti e resisti raggiungi e conquisti."

(Trilussa)

Ringraziamenti

Sono passati ben cinque anni da quando il mio percorso universitario è iniziato. Non mentirò dicendo che "sembra ieri", anzi ammetto che sia stato un percorso lungo e faticoso, pieno di ostacoli e che ha richiesto molti sacrifici. Tirandone le somme non posso che giungere alla conclusione che ne sia valsa la pena, in quanto durante questi anni sono cresciuto come persona, arricchendomi di molte conoscenze scientifiche e formando un pesante bagaglio culturale. Tutto ciò non sarebbe stato possibile senza la presenza, l'aiuto e soprattutto il supporto di alcune persone, che ci tengo molto a ringraziare.

In primis il ringraziamento più grande va ai miei genitori, papà Fiorenzo e mamma Laura. Grazie per avermi concesso l'immensa opportunità di studiare ingegneria e di seguire la mia grande passione. Grazie per avermi ascoltato parlare per anni di cose incomprensibili, avendo la pazienza di sopportarmi in ogni momento e di trovare sempre il modo per motivarmi ed incoraggiarmi.

Un doveroso ringraziamento va anche a mio fratello Marco, sempre presente nel momento del bisogno ed alla nonna Ines, sempre pronta a mostrarmi un sorriso sincero qualora gli esami andassero bene ed a preparare un bel piatto di pasta per consolarmi in caso contrario.

Grazie di cuore a Laura, mio sostegno nei momenti difficili e mia più grande motivazione. Sei senza dubbio la persona che mi abbia fatto crescere di più a livello umano nella mia vita. Il pensiero che tu fossi al mio fianco mi ha sempre spinto a fare meglio e non mollare di un centimetro, con la speranza che questo possa continuare ancora a lungo.

Grazie al professor Ferdinando Mapelli per avermi concesso l'opportunità di svolgere questo lavoro, credendo in me dal primo momento e fornendomi delle spiccate competenze pratiche. Lei è sempre stato disposto ad ascoltare le mie idee ed a correggere la mia rotta qualora fossi fuori strada; credo che questa sia la vera essenza dell'essere un professore: suggerire una corretta via e lasciare che lo studente la esplori imparando dagli errori.

Grazie inoltre a Laura Bacci, che mi ha seguito con costanza ed interesse durante lo svolgimento della tesi, aiutandomi con delle nozioni pratiche a me sconosciute e condividendo l'entusiasmo derivante dai risultati raggiunti.

Grazie a Veronica, mia grandissima amica che crede in me fin dai tempi del Liceo. Nei tuoi occhi che brillano ho sempre visto orgoglio e dal tuo spirito combattivo ho sempre tratto ispirazione per non arrendermi.

Grazie a tutti i miei amici e compagni di studio, Seve, Jaco, Teone, Spotty, Cri ed Ale, ognuno ha contribuito a rendere unica ogni giornata passata al Politecnico ed ogni serata passata a dimenticare le piccole sconfitte.

Grazie a Mauro (Ringo), che è stato un fantastico maestro ed allievo, oltre che uno dei migliori amici che io abbia mai incontrato. Sei sempre stato pronto a rompere le scatole e strapparmi un sorriso anche nelle giornate più difficili e sei quello che più gioiva ai miei successi, a te devo moltissimo.

ABSTRACT

The aim of this work is to analyze and implement techniques which allow to run a sensorless control over an Interior Permanent Magnet (IPM) synchronous motor These methods have to be robust and precise enough to be applied to both industrial and traction applications, saving the space and fault possibility of rotational transducers and therefore saving weight and cost.

After an accurate study of the electrical machine considered, the sensorless methods for identifying the rotor position and speed available in literature will be review and analyzed, together with their strengths and weaknesses. Overall, the sensorless control can be sub-divided into two speed ranges: one including standstill and very low rotational speeds and one concerning high velocities. Methods which exploit the saliency of the IPM by means of a continuous high frequency voltage injection and those that make use of a virtual stator flux observer are considered the most suitable for each speed range, respectively.

These techniques will be implemented in a simulation environment, which will show that good results can be obtained, with a position estimation error in the range of $1 \div 5$ degrees for low speeds and of $0 \div 2$ degrees for high speeds. The methods will also be merged by means of transition algorithms to obtain a wide-speed range sensorless control until the base speed (and presumably even above).

Finally, the developed methods will be experimentally implemented and

validated to assess the feasibility of a sensorless control over an IPM motor. The test conducted will show that this is possible, at least in no load conditions, with a position estimation error in the range of $5 \div 10$ degrees. This error, together with its noisiness, of course reflect on the estimated speed, anyway not hindering too much the robustness of the control itself, which, with several further improvement, can be used without any doubt in industrial applications.

ESTRATTO IN ITALIANO

L'obbiettivo di questo lavoro è quello di analizzare ed implementare tecniche che permettano di eseguire il controllo senza sensori di un motore sincrono a magneti permanenti affogati (IPM). Questi metodi devono essere abbastanza robusti e precisi da poter essere applicati sia in ambito industriale che di trazione, risparmiando spazio ed evitando i guasti relativi all'usura dei sensori, quindi alleggerendo il peso degli azionamenti ed il loro costo.

Dopo un accurato studio della macchina elettrica considerata, i metodi sensorless per l'identificazione di posizione e velocità rotorica esistenti in letteratura saranno riassunti ed analizzati nei loro punti di forza e debolezze. In generale, i controlli sensorless possono essere suddivisi, rispetto alla velocità di rotazione, in due macro-categorie: quelli che operano a rotore fermo o a basse velocità e quelli che funzionano ad alte velocità. I metodi che sfruttano la salienza rotorica del motore IPM tramite l'iniezione di un segnale ad alta frequenza e le tecniche che fanno uso di osservatori di un flusso rotorico virtuale sono considerate le più promettenti e adatte alle due categorie, rispettivamente.

Queste tecniche verranno implementate in un ambiente di simulazione, in quale mostrerà che buoni risultati possono essere ottenuti, quali un errore di posizione di $1 \div 5$ gradi a basse velocità e di $0 \div 2$ ad alte velocità. I metodi verranno inoltre interconnessi per ottenere un controllo capace di operare su tutto il range di velocità fino alla velocità di base (e prevedibil-

mente oltre).

Infine, i metodi sviluppati saranno implementati sperimentalmente e validati per verificare l'applicabilità del controllo sensorless su di un motore IPM. I test condotti mostreranno che tutto ciò è possibile, con un errore di stima della posizione nel range di $5 \div 10$ gradi. Questo errore, insieme alla sua varianza dovuta al rumore, certamente si riflette sulla stima vi velocità, senza però intaccare fortemente la robustezza del controllo che, certamente con alcune migliorie, potrà essere utilizzato in ambito industriale.

Contents

List of Figures

List of Tables

List of abbreviations

DC	Direct Current
AC	Alternating Current
EMF	Electro-Motive Force
EV	Electric Vehicle
HEV	Hybrid Electric Vehicle
FFT	Fast Fourier Transform
IM	Induction Motor
SPM	Synchronous Permanent Magnet
PMSM	Permanent Magnet Synchronous Motor
IPM	Interior Permanent Magnet
IPMSM	Interior-mounted Permanent Magnet Synchronous Motor
SPMSM	Surface-mounted Permanent Magnet Synchronous Motor
RM	Reluctance machine
LUT	Look-Up Table
MTPA	Maximum Torque Per Ampere
PWM	Pulse Width Modulation
SV	Space Vector
VSI	Voltage Source Inverter
HF	High Frequency
HFI	High Frequency Injection
PLL	Phase Lock Loop
KF	Kalman Filter

List of symbols

α	Direct axis in stator reference frame
β	Quadrature axis in stator reference frame
d	Direct axis in rotor reference frame
q	Quadrature axis in rotor reference frame
d^e	Estimated direct axis in rotor reference frame
q^e	Estimated quadrature axis in rotor reference frame
$\underline{v}$	Voltage vector in *abc* reference frame
v_a	*a*-axis voltage
v_b	*b*-axis voltage
v_c	*c*-axis voltage
$\underline{v}^{\alpha\beta}$	Voltage vector in $\alpha\beta$ reference frame
v_α	α-axis voltage
v_β	β-axis voltage
$\underline{v}^{dq}$	Voltage vector in *dq* reference frame
v_d	*d*-axis voltage
v_q	*q*-axis voltage
$\underline{i}$	Current vector in *abc* reference frame
i_a	*a*-axis current
i_b	*b*-axis current
i_c	*c*-axis current
$\underline{i}^{\alpha\beta}$	Current vector in $\alpha\beta$ reference frame
i_α	α-axis current

i_β	β-axis current
$\underline{i}^{dq}$	Current vector in *dq* reference frame
i_d	*d*-axis current
i_q	*q*-axis current
$\underline{\Psi}$	Magnetic flux vector in *abc* reference frame
Ψ_a	*a*-axis magnetic flux
Ψ_b	*b*-axis magnetic flux
Ψ_c	*c*-axis magnetic flux
$\underline{\Psi}^{\alpha\beta}$	Magnetic flux in αβ reference frame
Ψ_α	α-axis magnetic flux
Ψ_β	β-axis magnetic flux
$\underline{\Psi}^{dq}$	Magnetic flux in *dq* reference frame
Ψ_d	*d*-axis magnetic flux
Ψ_q	*q*-axis magnetic flux
$\underline{\Psi}_M$	PM magnetic flux vector in *abc* reference frame
Ψ_{aM}	*a*-axis PM magnetic flux
Ψ_{bM}	*b*-axis PM magnetic flux
Ψ_{cM}	*c*-axis PM magnetic flux
$\underline{\Psi}_M^{\alpha\beta}$	PM magnetic flux vector in αβ reference framex
$\underline{\Psi}_M^{dq}$	PM magnetic flux vector in *dq* reference frame
Ψ_m	Permanent magnet magnetic flux
L_{aa}	*a*-axis self inductance
L_{bb}	*b*-axis self inductance
L_{cc}	*c*-axis self inductance
$L_{\sigma s}$	Leakage inductance
L_{ms0}	Magnetizing inductance constant component
L_{ma}	Magnetizing inductance anisotropic component
L_{ab}, L_{ba}	*a* and *b* axis mutual inductances
L_{ac}, L_{ca}	*a* and *c* axis mutual inductances

L_{bc}, L_{cb}	*b* and *c* axis mutual inductances
M_s	Magnetizing inductance constant component for mutual inductances
R_s	Stotor electric resistance
T_m	Mechanical torque
P_m	Mechanical power
n_p	Number of pole pairs
J	Inertia
θ_r	Electrical angular position
θ_r	Mechanical angular position
θ_r	High frequency carrirer angular position
ω_r	Electrical angular velocity
ω_m	Mechanical angular velocity
ω_c	High frequency carrier angular velocity
T_{Clarke}	Clarke transform
T_{Park}	Park transform
$*$	Complex Conjugate
$_{hf}$	High frequency component of a signal
$_p$	Positive sequence of a signal
$_n$	Negative sequence of a signal
ϵ	Error
$\hat{}$, $_{est}$	Estimation
Φ	Phase shift
$\|\ \|$	Magnitude
$\angle$	Phase
j	Imaginary unit

INTRODUCTION

The majority of industrial applications that involve motion is nowadays achieved with electrical machines, which make use of electro-magnetic effects to generate high density power with little losses. Besides, due to pollution constraints, also electric traction applications are taking over the research activities and a big attention from factories is starting to being given. Although DC motors were very common in past years, most of the motion control is now achieved with three-phase AC systems, such as induction machines (IM), permanent magnet synchronous motors (PMSM) and reluctance machines (RM). This thesis will focus on the synchronous motor because, further than not needing brushes and having a high precision capability in torque control, elements which are in common with IMs, they bring the advantages of having an high efficiency, an high ratio between generated torque and inertia and an high accuracy possibility in position and speed control. These advantages are even more highlighted by the fact that the control of PMSM is even easier with respect to those of different motor technologies. The only weakness they present is the cost: high performing PM are limited to find in nature, so as rare heart materials they could be synthetized from, but this drawback is not hindering their growing application in EV and HEV in a large variety of fields, from automotive to aeronautics, from agriculture to marine, without of course forgetting of industrial high precision and high torque demanding applications.
In the topic of synchronous motor two macro-categories exist: those with

the PM mounted on the rotor surface and those with PM buried inside it. The former requires an high number of magnets for performing operation, but its model is quite simple and well-studied. The latter on the opposite have the advantage of being cheaper but their behavior is highly non-linear and their control hugely depends on the identified parameters. Additionally, while SPM synchronous machines can only count on the torque generated by the interaction of the PM with the stator currents (magnetic torque), IPM motors also exhibit a reluctance torque component deriving from the inductance difference between its axis. This feature allows buried-magnets motors to perform better and provide higher torque, especially over the base speed in the field weakening region, which is a big concern in automotive applications.

Recently, due to space, cost and hardware reliability constraints there is a trend in of avoiding the usage of position, speed and torque sensors. Of course, the control of any kind of electrical machine can not make without the position information for operating in the maximum torque condition by means of the MTPA controls, which allows to optimize the usage of batteries internal energy; furthermore, a speed feedback is required in a wide range of applications. A solution to this demanding request is represented by the developing of sensorless controls, which only require the knowledge of the voltages applied to the motors and the measurement of the currents generated from them. By means of specific estimators it is possible to retrieve mechanical informations about the rotor with the only usage of electrical quantities. In the wide variety of electrical machines only IPM motors and reluctance motors, in both their switched reluctance (SRM) and synchronous reluctance (SynRM) configurations, are the ones that can undergo a wide speed range sensorless control. This is because in the actual state of art all the control methods based on traditional observers fail at standstill or very low speeds due to the barely null back-EMF and very low

flux linkage present. The above mentioned motors, on the contrary, thanks to their constructive intrinsically generated saliency, are feasible of being applied methods for the precise estimation of the rotor position and speed. The aim of this thesis is therefore to study and implement the techniques allowing the sensorless control of an IPM synchronous motors and develop an application based on the introduced methods capable of satisfying strict accuracy constraints, while providing an high torque.

This thesis is structured in this way:

In *chapter 1* the main features of the IPM motor will be described and compared to those of classical SPM machines. The mathematical modelling used in the following chapters will also be introduced and explained.

In *chapter 2* the state of art in sensorless identification methods will be reported, together with a comparison between the better-promising techniques. High frequency injection methods and flux reconstructors will be chosen among all.

In *chapter 3* the development of a sensorless algorithm combining the chosen methods will be described and a model will be set up with the help of MAtlab and Simulink. The results obtained from simulations will be analyzed and the expectation from the experimental implementation introduced.

In *chapter 4* the hardware setup used in a practical implementation of the sensorless control will be described and several tests will be performed to assess its performances in both unloaded and loaded operation.

At last, conclusion from the work will be drawn, together with possible future developments proposals.

Chapter 1

INTERIOR PERMANENT MAGNET MOTOR

In this chapter the permanent magnet synchronous motor (PMSM) will be described in both its constructive and electrical features. The focus will be on the internal permanent magnet (IPM) configuration of the rotor, whose properties will be analyzed.

1.1 Introduction

The synchronous PM machine is constituted by a stator and a rotor. The stator is, as in IMs, a piece of ferromagnetic material which exhibits slots on its surface, filled with distributed three phase windings. Those are fed by sinusoidal currents generated by a current-controlled voltage source inverter (VSI) in order to give rise to a continuously rotating magnetic field, which is revolving at the so called *synchronous speed*. The rotor, also made of ferromagnetic material, is equipped with permanent magnets (PM), that introduce the advantage of requiring little space for the creation of a dense magnetic field; their presence introduce barely null losses in rotor iron magnetization, contrary to what happens with rotor windings in IMs, resulting

in higher torque density and efficiency. Furthermore, the PMs own a high energy density and thus require very small space for the magnetization of the rotor with a dense magnetic field capable of sustaining high coercive torque. In addition to that, the cost of PM in recent years is continuously decreasing, which combined to an high attention to energy saving application, is pushing PMSM to being increasingly studied and developed.

1.2 Constructive feature

The PM on the synchronous machine's rotors can be positioned in various manners, defining the behavior and the characteristics of the machine; the main configurations are showed in figure 1 and can be classified into two classes which the name of surface-mounted PM (SPM) and internal-mounted PM (IPM).

Figure 1.1 shows a cross-section of a 4-poles SPM machine with the PM

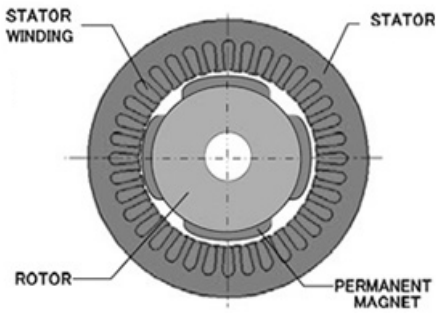

Figure 1.1: SPM 4-poles motor [2]

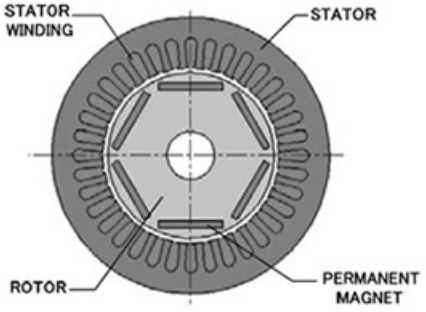

Figure 1.2: IPM 6-poles motor [2]

attached on the external surface of the rotor. The magnetic flux generated by the PM crosses the same amount of steel, air and magnets along the d and q axes, making this machine isotropic. This means that its properties are independent with respect to the direction in which the magnetic phenomena are considered and in particular that the inductance L is constant

and independent on the rotor position. This kind of motors are employed in low speed application because at high speeds the magnets would tend to fly apart due to the centrifugal force.

Figure 1.2 shows a cross-section of a 6-poles IPM rotor, in which the PM are buried inside the ferromagnetic core with alternating polarity. It can be noticed that the magnetic flux along the d axis crosses the PM, whose permeability is close to that of the air, while the flux along the q axis does not. This results in a difference of magnetic inductances on the axis, in particular to the inductance L_d to be noticeably lower than L_q, leading the motor to be anisotropic. This configuration has the drawback of requiring a more complex and accurate parameter identification concerning the inductance difference, to the aim of control, but on the other hand it is mechanically stronger and can undergo higher velocities without the risk of the PM flying apart from their position. IPM motors also have the capability of generating higher torque with respect to SPM motors, being it composed by two terms: the PM torque (present in the SPM as well) and the reluctance torque given by the dq axis inductance difference.

From an electro-magnetic point of view it is important to emphasize that burying the PM inside the rotor introduces a saliency in the machine, feature that is not present in any other motor. The saliency can be better explained and understood by looking at the interaction between the PM flux and the magnetic field produced by the stator currents. First of all it is necessary to recall that we are dealing with a 2-axis system obtained by means of Clarke-Parke transformation (see section 1.3) and that the d and q axis are shifted by $\frac{90^o}{n_p}$, where n_p is the number of pole pairs. As it can be seen in figure 1.3, in a SPM machine both the flux generated by the PM and the one generated by the current i_d are aligned on the d axis (they will thus be summed), while the quadrature component generated by the q axis current is shifted by 45 electrical degrees (for a 4-poles machine). Being the PM at-

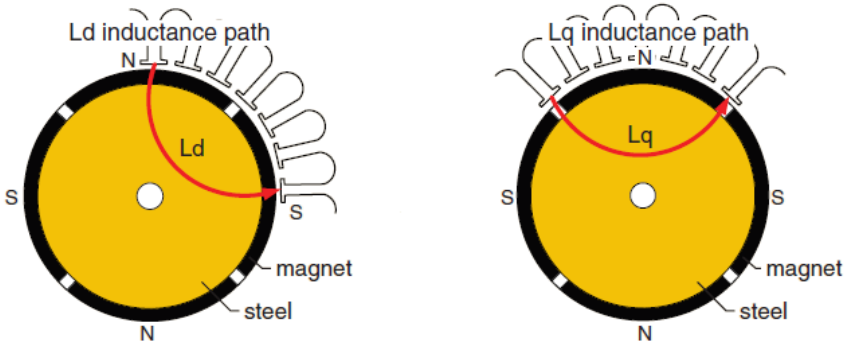

Figure 1.3: SPM 4-poles motor flux lines [3]

tached on the periphery of the rotor the flux on both axes sees the same path at each rotor position, resulting in an inductance L which is constant. The situation is different in a IPM motor: figure 1.4 shows how the mag-

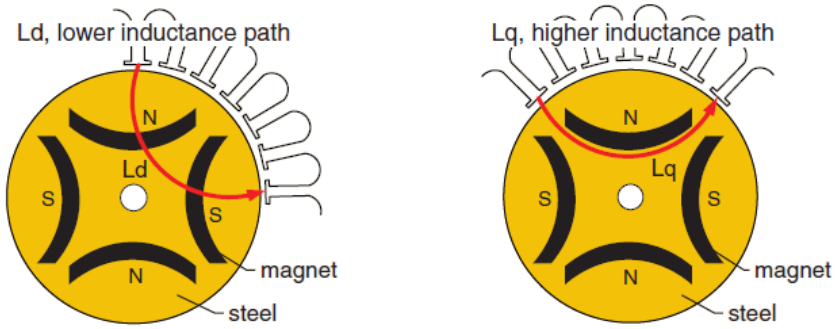

Figure 1.4: IPM 4-poles motor flux lines [3]

netic flux along the d axis has to cross, in addition to two air gaps between stator and rotor, also 2 magnets. Recalling that the ceramic and rare earth magnets permeability is close to the one of air, it follows that the d axis flux path must pass through a considerably large air gap. Looking at the q axis path it can be noticed instead that the flux can avoid passing through the magnets and only crosses the two air gaps between stator and rotor and the ferromagnetic material. This results in a difference of the flux path seen by the axis and more precisely an higher magnetic inductance with q axis rotor orientation.

1.3 Model of the motor

1.3.1 Three-phase electrical model

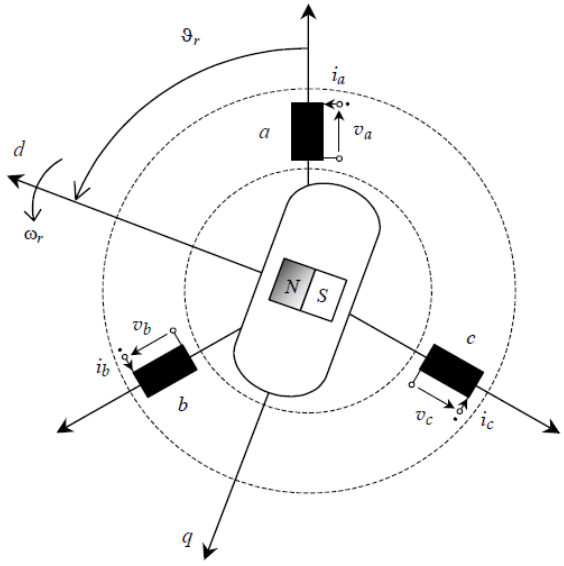

Figure 1.5: Schematic IPM synchonous machine in *abc* reference frame [4]

The synchronous IPM motor is shown schematically in figure 1.5. It consists of a stator with three windings, a, b and c, phase shifted by $\frac{2}{3}\pi$ and a rotor. The latter is represented as a salient pole magnet in order to outline the magnetic anisotropy caused by the PM buried in the iron. The magnetic flux provided by the PM is considered constant and equal to Ψ_m.
The quantities of our interest are the electrical position (θ_r) and speed, which is defined as:

$$\omega_r = \frac{d\theta_r}{dt} \tag{1.1}$$

They are linked to the periodicity by which the angular position affects the stator windings, while the mechanical ones actually describe the movement and are calculated as $\theta_m = p\theta_r$ and $\omega_m = p\omega_r$. The rotor absolute position is measured between the *a* stator phase axis and the *d* rotor magnetic axis. Throughout this thesis it will be assumed that the inductance on the *d* axis

is smaller than the one on q axis, as it is in nowadays practice and in most physical realizations more common.

Given the previous assumptions and applying the Kirchhoff's second law to the stator windings, the following system of equations is obtained (for simplicity in notation the dependence on time of the voltage $V(t)$, current $i(t)$ and flux linkage $\Psi(t)$ will be omitted):

$$\begin{cases} v_a = R_a i_a + \frac{d\Psi_a}{dt} \\ v_b = R_b i_b + \frac{d\Psi_b}{dt} \\ v_c = R_c i_c + \frac{d\Psi_c}{dt} \end{cases} \tag{1.2}$$

Assuming that there is symmetrical construction of the machine, the phase resistances R_a, R_b and R_c will be all considered equal to R_s.

To better exploit the behavior of the machine, under the hypothesis of linearity in the magnetic circuits, each phase's flux linkage component can be re-written as:

$$\begin{cases} \Psi_a = L_{aa} i_a + L_{ab} i_b + L_{ac} i_c + \Psi_{aM} \\ \Psi_b = L_{ba} i_a + L_{bb} i_b + L_{bc} i_c + \Psi_{bM} \\ \Psi_c = L_{ca} i_a + L_{cb} i_b + L_{cc} i_c + \Psi_{cM} \end{cases} \tag{1.3}$$

where:

- The self-inductances L_{aa}, L_{bb} and L_{cc} take into account the flux linkage of each winding with itself, arising due to the current flowing into each winding. They are function of the rotor position because of its saliency:

$$\begin{cases} L_{aa} = L_{\sigma s} + L_{ms0} + L_{ma}\cos\left(2\theta_r\right) \\ L_{bb} = L_{\sigma s} + L_{ms0} + L_{ma}\cos\left(2\theta_r + \frac{2}{3}\pi\right) \\ L_{cc} = L_{\sigma s} + L_{ms0} + L_{ma}\cos\left(2\theta_r - \frac{2}{3}\pi\right) \end{cases} \tag{1.4}$$

  being:

- $L_{\sigma s}$ the leakage induction, meaning the amount of the flux that can't make it through the iron and reach the rotor;
- L_{ms0} the constant component of the magnetizing induction;
- L_{ma} the anisotropy component of the magnetizing induction, function of twice the angular position.

– The mutual-inductances take into account the flux linkage of a winding arising from the current flowing in the other two windings. They are still function of twice the rotor angle as follows:

$$\begin{cases} L_{ab} = L_{ba} = M_s + L_{ma}\cos\left(2\theta_r - \frac{2}{3}\pi\right) \\ L_{bc} = L_{cb} = M_s + L_{ma}\cos\left(2\theta_r + \frac{2}{3}\pi\right) \\ L_{ac} = L_{ca} = M_s + L_{ma}\cos\left(2\theta_r\right) \end{cases} \tag{1.5}$$

with

$$M_s = L_{ms0}\cos\left(\frac{2}{3}\pi\right) = -\frac{L_{ms0}}{2}$$

being the fraction of the constant magnetizing component obtained considering the phase shifting between the axis.

– The stator flux linkage components due to the permanent magnets are function of the rotor position:

$$\begin{cases} \Psi_{aM} = \Psi_m\cos\left(\theta_r\right) \\ \Psi_{bM} = \Psi_m\cos\left(\theta_r - \frac{2}{3}\pi\right) \\ \Psi_{cM} = \Psi_m\cos\left(\theta_r + \frac{2}{3}\pi\right) \end{cases} \tag{1.6}$$

To ease the notation and allow for a faster understanding, the previously explained model can be re-written in matrix form as follows:

$$\begin{cases} \underline{v} = [R_s]\underline{i} + \frac{d\underline{\Psi}}{dt} \\ \underline{\Psi} = [L_{ss}(2\theta_r)]\underline{i} + \underline{\Psi}_M(\theta_r) \end{cases} \tag{1.7}$$

where

$$\underline{v} = \begin{bmatrix} v_a \\ v_b \\ v_c \end{bmatrix} \quad [R_s] = \begin{bmatrix} R_s & 0 & 0 \\ 0 & R_s & 0 \\ 0 & 0 & R_s \end{bmatrix} \quad \underline{i} = \begin{bmatrix} i_a \\ i_b \\ i_c \end{bmatrix} \quad \underline{\Psi} = \begin{bmatrix} \Psi_a \\ \Psi_b \\ \Psi_c \end{bmatrix} \tag{1.8}$$

The PM flux linkage and the inductance matrix read:

$$\underline{\Psi}_M = \Psi_m \begin{bmatrix} \cos\left(\theta_r\right) \\ \cos\left(\theta_r - \frac{2}{3}\pi\right) \\ \cos\left(\theta_r + \frac{2}{3}\pi\right) \end{bmatrix} \tag{1.9}$$

$$L_{ss} = [L_{ss0}] + [L_{sm}(2\theta_r)] \tag{1.10}$$

From equations (1.4) and (1.5) it also follows that:

$$[L_{ss0}] = \begin{bmatrix} L_{ms0} + L_{\sigma s} & -\frac{1}{2}L_{ms0} & -\frac{1}{2}L_{ms0} \\ -\frac{1}{2}L_{ms0} & L_{ms0} + L_{\sigma s} & -\frac{1}{2}L_{ms0} \\ -\frac{1}{2}L_{ms0} & -\frac{1}{2}L_{ms0} & L_{ms0} + L_{\sigma s} \end{bmatrix} \tag{1.11}$$

and

$$[L_{sm}] = L_{ma} \begin{bmatrix} \cos\left(2\theta_r\right) & \cos\left(2\theta_r - \frac{2}{3}\pi\right) & \cos\left(2\theta_r + \frac{2}{3}\pi\right) \\ \cos\left(2\theta_r - \frac{2}{3}\pi\right) & \cos\left(2\theta_r + \frac{2}{3}\pi\right) & \cos\left(2\theta_r\right) \\ \cos\left(2\theta_r + \frac{2}{3}\pi\right) & \cos\left(2\theta_r\right) & \cos\left(2\theta_r - \frac{2}{3}\pi\right) \end{bmatrix} \tag{1.12}$$

1.3.2 Clarke transform and model in stator $\alpha\beta$ reference frame

Once the motor model has been found starting from the electrical equivalent circuit and all its component has been described, it is convenient for simplicity to move from a three-phase reference system to a two-axis frame. This is possible by applying the so-called Clarke transform, consisting in a transformation matrix allowing to shift the electrical quantities without modifying their amplitude:

$$T_{Clarke} = \frac{2}{3} \begin{bmatrix} 1 & -\frac{1}{2} & -\frac{1}{2} \\ 0 & \frac{\sqrt{3}}{2} & -\frac{\sqrt{3}}{2} \\ \frac{1}{2} & \frac{1}{2} & \frac{1}{2} \end{bmatrix} \tag{1.13}$$

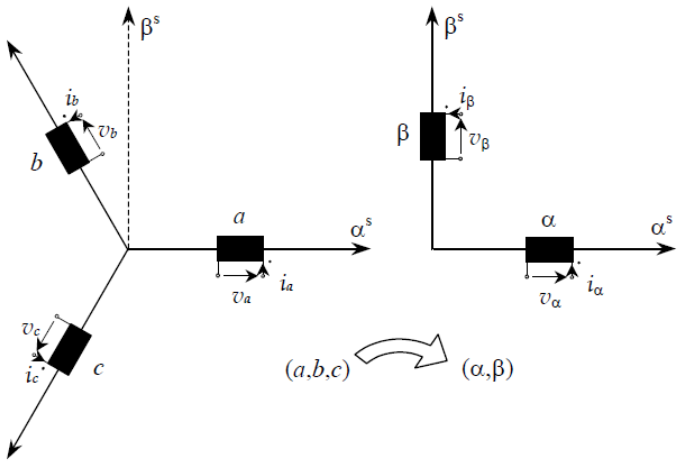

Figure 1.6: Clarke transform [4]

The α axis of the transformed system is chose to coincide with the a axis of the original reference frame, while the β axis will be orthogonal to it.

Applying the transformation to the original system (matrix notation is used):

$$\underline{v}^{\alpha\beta} = [T_{Clarke}]\underline{v} \quad \underline{i}^{\alpha\beta} = [T_{Clarke}]\underline{i} \quad \underline{\Psi}^{\alpha\beta} = [T_{Clarke}]\underline{\Psi} \tag{1.14}$$

The following model is obtained:

$$\begin{cases} \underline{v}^{\alpha\beta} = [R_s]\underline{i}^{\alpha\beta} + \frac{d\underline{\Psi}^{\alpha\beta}}{dt} \\ \underline{\Psi}^{\alpha\beta} = [L_{ss}(2\theta_r)]\underline{i}^{\alpha\beta} + \underline{\Psi}_M^{\alpha\beta}(\theta_r) \end{cases} \tag{1.15}$$

where:

$$\underline{v}^{\alpha\beta} = \begin{bmatrix} v_\alpha \\ v_\beta \\ 0 \end{bmatrix} \quad \underline{i}^{\alpha\beta} = \begin{bmatrix} i_\alpha \\ i_\beta \\ 0 \end{bmatrix} \quad \underline{\Psi}^{\alpha\beta} = \begin{bmatrix} \Psi_\alpha \\ \Psi_\beta \\ 0 \end{bmatrix} \tag{1.16}$$

The flux linkage due to the permanent magnet still keeps its dependance from rotor position but becomes:

$$\underline{\Psi}_M^{\alpha\beta} = \sqrt{\frac{3}{2}}\Psi_m \begin{bmatrix} \cos(\theta_r) \\ \sin(\theta_r) \\ 0 \end{bmatrix} \tag{1.17}$$

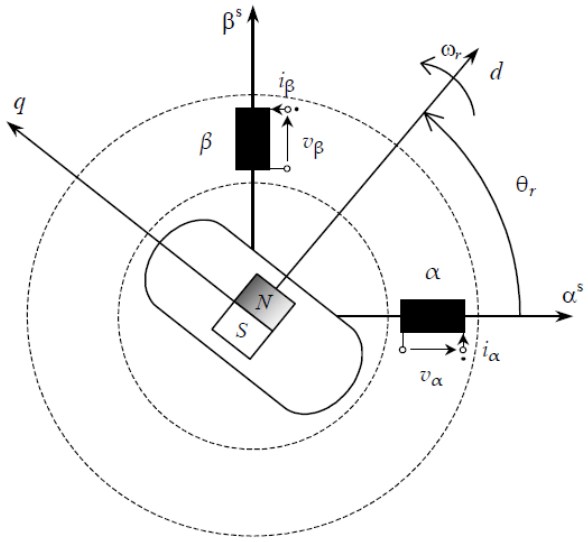

Figure 1.7: Schematic IPM synchonous machine in αβ reference frame [4]

Similarly, the two components of the inductance matrix now take the form:

$$[L_{ss0}] = \begin{bmatrix} \frac{3}{2}L_{ms0} + L\sigma s & 0 & 0 \\ 0 & \frac{3}{2}L_{ms0} + L\sigma s & 0 \\ 0 & 0 & L_{\sigma s} \end{bmatrix} \tag{1.18}$$

and

$$[L_{sm}] = \frac{3}{2}L_{ma} \begin{bmatrix} \cos(2\theta_r) & \sin(2\theta_r) & 0 \\ \sin(2\theta_r) & -\cos(2\theta_r) & 0 \\ 0 & 0 & 0 \end{bmatrix} \tag{1.19}$$

Since we assumed at first that the system is considered symmetric by construction the third row of the inductance matrix, the so-called omopolar component, can be neglected: the procedure thus transformed the three-phase machine into an equivalent two-phase one with orthogonal axes.

1.3.3 Park transform and model in rotor *dq* reference framee

To the aim of control, it is necessary not only to have the model of the machine in a 2-axis form, but to have it also in a rotating reference frame

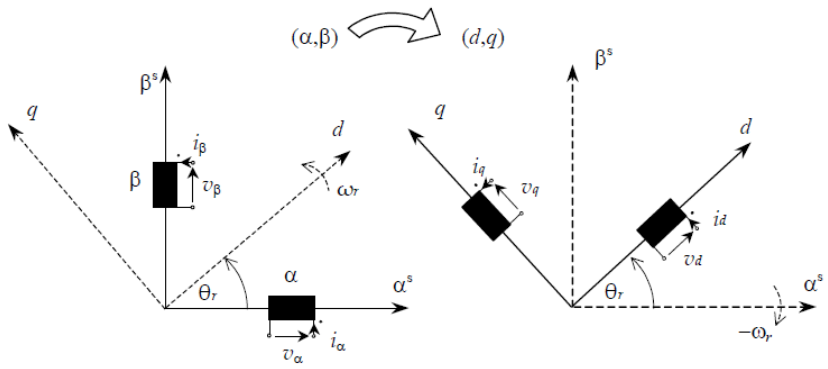

Figure 1.8: Park transform [4]

synchronous with the motor. This is achieved by means of the Park transform, a matrix operation similar to the Clark transform that shifts the orthogonal and stationary α and β axis to the rotating d and q ones. An orthogonal transformation matrix is introduced:

$$T_{Park} = \begin{bmatrix} \cos(\theta_r) & \sin(\theta_r) & 0 \\ -\sin(\theta_r) & \cos(\theta_r) & 0 \\ 0 & 0 & 1 \end{bmatrix} \tag{1.20}$$

Similarly to the Clarke transform, the Park transform is applied to the system:

$$\underline{v}^{dq} = [T_{Park}]\underline{v}^{\alpha\beta} \quad \underline{i}^{dq} = [T_{Park}]\underline{i}^{\alpha\beta} \quad \underline{\Psi}^{dq} = [T_{Park}]\underline{\Psi}^{\alpha\beta} \tag{1.21}$$

and the model rotating synchronously with the rotor is obtained:

$$\begin{cases} \underline{v}^{dq} = [R_s]\underline{i}^{dq} + \frac{d\underline{\Psi}^{dq}}{dt} + [J]\omega_r\underline{\Psi}^{dq} \\ \underline{\Psi}^{dq} = [L_{ss}]\underline{i}^{dq} + \underline{\Psi}_M^{dq} \end{cases} \tag{1.22}$$

where:

$$\underline{v}^{dq} = \begin{bmatrix} v_d \\ v_q \\ 0 \end{bmatrix} \quad \underline{i}^{dq} = \begin{bmatrix} i_d \\ i_q \\ 0 \end{bmatrix} \quad \underline{\Psi}^{dq} = \begin{bmatrix} \Psi_d \\ \Psi_q \\ 0 \end{bmatrix} \quad [J] = \begin{bmatrix} 0 & -1 & 0 \\ 1 & 0 & 0 \\ 0 & 0 & 0 \end{bmatrix} \tag{1.23}$$

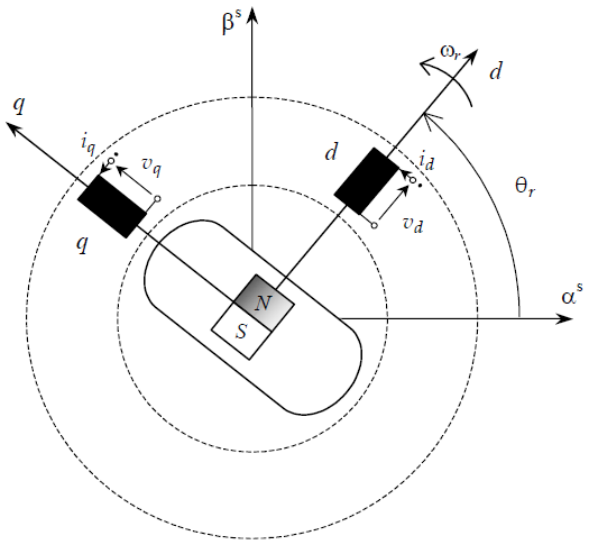

Figure 1.9: Schematic IPM synchonous machine in *dq* reference frame [4]

Note that the dependence on position is eliminated from both the PM flux linkage component and the inductance matrix, which now read:

$$\underline{\Psi}_M^{dq} = \sqrt{\frac{3}{2}} \begin{bmatrix} \Psi_m \\ 0 \\ 0 \end{bmatrix} \tag{1.24}$$

$$[L_{ss}] = [L_{ss0}] + [L_{sm}] \tag{1.25}$$

with $[L_{ss0}]$ the same as equation (1.18) and

$$[L_{sm}] = \frac{3}{2} L_{ma} \begin{bmatrix} 1 & 0 & 0 \\ 0 & -1 & 0 \\ 0 & 0 & 0 \end{bmatrix} \tag{1.26}$$

Park transform allowed to obtain a model of the IPM machine on two axis rotating synchronously with the rotor and we will see that this is a key point for designing a robust control scheme. Still there is one simplification that can be done and it regards the so-called **synchronous inductances**. Having eliminated the dependence over position from the inductance ma-

trix, equation (1.25) can be rewritten as:

$$[L_{ss}] = \begin{bmatrix} L_d & 0 & 0 \\ 0 & L_q & 0 \\ 0 & 0 & L_{\sigma s} \end{bmatrix} \tag{1.27}$$

where

$$L_d = L_{\sigma s} + L_{md} \qquad L_q = L_{\sigma s} + L_{mq} \tag{1.28}$$

are, respectively, the synchronous inductance of the direct and quadrature axis, with

$$L_{md} = \frac{3}{2}(L_{ms0} + L_{ma}) \qquad L_{mq} = \frac{3}{2}(L_{ms0} - L_{ma}) \tag{1.29}$$

the coresponding magnetizing inductances.

1.3.4 Model simplification for high frequency injection

In the following a further simplification for the model described above will be reported. It is a topic case in which the machine is operating under high frequency excitation. A preliminary assumption has to be made and it is that the motor windings resistance and inductance are supposed to be constant in the whole frequency range. The simplification consists of cancelling the terms of the model that at high enough frequencies become negligible with respect to others. The simplified equations of the model will be very useful in the following of this thesis when sensorless algorithms will be employed for running the control of the machine.

Each of the three phases of the machine windings can be seen as a transfer function from voltage to current. These transfer function are very likely to be low-pass filters of first order, being the inductance impedance proportional to the frequency. These transfer function have time constant $\tau_{RL} = \frac{\Sigma L}{R}$ so, for frequencies $\omega_{hf} >> \frac{1}{\tau_{RL}}$ resistive losses can be neglected, so as the PM flux linkage. The model described by equation (1.22) will thus

become:

$$\begin{cases} \underline{v}^{dq} = \frac{d\underline{\Psi}^{dq}}{dt} + [J]\omega_r \underline{\Psi}^{dq} \\ \underline{\Psi}^{dq} = [L_{ss}]\underline{i}^{dq} \end{cases} \tag{1.30}$$

Applying the Park anti-transform to the least obtained system or, alternatively, neglecting the same terms in equation (1.15), it can be found that this simplification is even more appreciable in the stator reference frame, leading the system to be:

$$\begin{cases} \underline{v}^{\alpha\beta} = \frac{d\underline{\Psi}^{\alpha\beta}}{dt} = [L_{ss}(2\theta_r)]\frac{d\underline{i}^{\alpha\beta}}{dt} \\ \underline{\Psi}^{\alpha\beta} = [L_{ss}(2\theta_r)]\underline{i}^{\alpha\beta} \end{cases} \tag{1.31}$$

For what concerns the interaction with the mechanical system, the injection of signals (be them currents or voltages) at high frequencies will not disturb it and their effects will be neglected. This is understandable thinking that usually the mechanical time constants are much greater than the electrical ones. So, applying signals at a frequency higher than the cut-off frequency of the electrical system, would mean to apply to the mechanical system a disturbance at a huge frequency, where it is more likely to attenuate any input. To sum up, in presence of a high frequency signal injection the mechanical speed and acceleration of the rotor can be considered null.

1.3.5 State-space models

To implement a control scheme and work out control algorithms it is convenient to re-write the previously obtained Park model into state-space form, highlighting the dependence of flux or current over voltage. Doing so will also ease the tuning of the controllers, being the transfer function from voltage to flux or current easily available from this representation.

Manipulating equation (1.22) a more explicit notation can be found as:

$$\begin{cases} v_d = R_s i_d + \frac{d\Psi_d}{dt} - \omega_r \Psi_q \\ v_q = R_s i_q + \frac{d\Psi_q}{dt} + \omega_r \Psi_d \\ \Psi_d = L_d i_d + \Psi_m \\ \Psi_q = L_q i_q \end{cases} \tag{1.32}$$

In the following two models will be considered, taking as state variables the fluxes or the currents.

Fluxes as state variables

The first step is to work out the current dependence over the fluxes, from the latter's equations:

$$i_d = \frac{\Psi_d - \Psi_m}{L_d} \qquad i_q = \frac{\Psi_q}{L_q} \tag{1.33}$$

Substituting them into the voltage equation gives:

$$\begin{aligned} v_d &= \frac{R_s}{L_d}(\Psi_d - \Psi_m) + \frac{d\Psi_d}{dt} - \omega_r \Psi_q \\ v_q &= \frac{R_s}{L_q}\Psi_q + \frac{d\Psi_q}{dt} + \omega_r \Psi_d \end{aligned} \tag{1.34}$$

Finally, re-arranging the fluxes derivatives can be found

$$\begin{aligned} \frac{d\Psi_d}{dt} &= -\frac{R_s}{L_d}\Psi_d + \omega_r \Psi_q + v_d + \frac{R_s}{L_d}\Psi_m \\ \frac{d\Psi_q}{dt} &= -\omega_r \Psi_d - \frac{R_s}{L_q}\Psi_q + v_q \end{aligned} \tag{1.35}$$

In matrix form this system takes the form

$$\dot{\underline{x}} = [A]\underline{x} + [B]\underline{v} + [C] \tag{1.36}$$

where

$$[A] = \begin{bmatrix} -\frac{R_s}{L_d} & \omega_r \\ -\omega_r & -\frac{R_s}{L_q} \end{bmatrix} \quad [B] = \begin{bmatrix} 1 & 0 \\ 0 & 1 \end{bmatrix} \quad [C] = \begin{bmatrix} \frac{R_s}{L_d}\Psi_m \\ 0 \end{bmatrix} \tag{1.37}$$

One can notice that matrix [A] is not constant but depends on the rotor velocity, which can be also considered as a state variable in a mechanical equation, resulting in a non-linear model. One last remark should be done on this representation and it is the presence of the [C] matrix, giving a constant contribute to the first equation: this may at first seem not to be a big concern, but when dealing with mathematical integration in the control scheme it turns out to be very uncomfortable (and tricky to remember) to set the integrator initial value to avoid spikes in the first instants. For this reason taking the currents as state variables is preferable.

Currents as state variables

Building a state-space model that takes the currents as state variables is very easy and consist of directly substituting the fluxes equations into the voltage ones:

$$\begin{aligned} v_d &= R_s i_d + \frac{d}{dt}(L_d i_d + \Psi_m) - \omega_r L_q i_q \\ v_q &= R_s i_q + \frac{d}{dt}(L_q i_q) + \omega_r (L_d i_d + \Psi_m) \end{aligned} \tag{1.38}$$

Being the flux given by the PM constant its derivative can be considered null and the differential equation can be found rearranging:

$$\begin{aligned} \frac{di_d}{dt} &= \frac{1}{L_d}(-R_s i_d + \omega_r L_q i_q + v_d) \\ \frac{di_q}{dt} &= \frac{1}{L_q}(-R_s i_q - \omega_r L_d i_d + v_q - \omega_r \Psi_m) \end{aligned} \tag{1.39}$$

In matrix form this system takes again the form

$$\dot{\underline{x}} = [A]\underline{x} + [B]\underline{v} + [C] \tag{1.40}$$

where

$$[A] = \begin{bmatrix} -\frac{R_s}{L_d} & \omega_r \frac{L_q}{L_d} \\ -\omega_r \frac{L_d}{L_q} & -\frac{R_s}{L_q} \end{bmatrix} \quad [B] = \begin{bmatrix} \frac{1}{L_d} & 0 \\ 0 & \frac{1}{L_q} \end{bmatrix} \quad [C] = \begin{bmatrix} 0 \\ -\omega_r \frac{\Psi_m}{L_q} \end{bmatrix} \tag{1.41}$$

This model still yields the same consideration done for the fluxes one about non-linearity of the [A] matrix and the need of one more mechanical equation for accounting the speed. On the other hand the [C] matrix is not constant anymore but it is also dependent on speed; this means that, considering the motor starting from null steady state, the issues given by the integrators are avoided in the control scheme.

1.3.6 Torque production

As said in the introduction of this chapter the main feature of the IPM synchronous machine is having a much higher torque production due to the magnetic anisotropy with respect of both induction machines and SPM synchronous motors. To better analyze this feature an energy balance has to be performed (for simplicity over the model in the synchronous rotor reference frame), obtaining the following equation:

$$\mathbb{R}e(\underline{v}\underline{i}^*) = R_s i^2 + \mathbb{R}e(\underline{i}^* \frac{d}{dt}\underline{\Psi}) + \mathbb{R}e(j\omega_r \underline{\Psi}\underline{i}^*) \tag{1.42}$$

The left-hand side term represents the total active energy entering the system, while the righ-hand side terms are, respectively, the Joule losses, the variation of the internal magnetic energy stored into the system in the inductances L_d and L_q and the mechanical power. Going into deeper level of detail the latter can be expressed as:

$$\begin{aligned} P_m &= \mathbb{R}e(j\omega_r \underline{\Psi}_s \underline{i}^*) = -\omega_r \, \mathbb{I}m(\underline{\Psi}\underline{i}^*) \\ &= -\omega_r \, \mathbb{I}m[(L_d i_d + \Psi_m + jL_q i_q)(i_d - i_q)] \\ &= \omega_r[(L_d - L_q) i_d i_q + \Psi_m i_q] \end{aligned} \tag{1.43}$$

Now, recalling that the electrical and mechanical velocities are linked by the relation $\omega_r = n_p \omega_m$ (where n_p is the number of pole pairs), the mechanical torque can be expressed as:

$$T_m = \frac{P_m}{\omega_m} = n_p \frac{P_m}{\omega_r} = n_p[(L_d - L_q) i_d i_q + \Psi_m i_q] \tag{1.44}$$

It is evident how torque is composed by two terms; the first one is called the anisotropy component while the second takes the name of excitation component. The latter, present also in the SPM machines, denotes how the d-axis oriented flux of the permanent magnets interacts with the q-axis stator current to create magnetic field alignment and therefore torque proportional to current i_q flowing into the windings. The most interesting feature of an IPM motor is represented by the anisotropy component, created by the magnetic fluxes along the *d* and *q* axes interacting with each other. This term is clearly generated because of the rotor saliency and is therefore proportional to the difference of inductances $(L_d - L_q)$

Chapter 2

SENSORLESS DRIVING TECHNIQUES

In this chapter the main sensorless control techniques for driving an IPM synchronous motor will be listed and analyzed, evaluating their strengths and drawbacks. At first the main difficulties in sensorless control will be described and a subdivision into different categories will be made. Secondly each technique will be explained and a comparison between them will be performed.

2.1 Overview

Nowadays synchronous machines are becoming more and more popular both in industrial and HEV or EV applications. This growth is associated with a major desire of system's reliability and with a big concern on costs reduction, both at first in the constructive phase and secondly in the maintenance period. Under this view the most problem-causing devices are without any doubt the sensors measuring the position and speed of the motors and the torque produced by them: they are very expensive and fragile, other than requiring additional space in the drive and constant maintenance. Anyway the measure of physical quantities is something of

which it can't be done without in control system, due to the need of information on the state of the machine to close a control loop. The goal of research in the last decade has therefore focused on developing algorithms able to estimate more or less precisely the physical quantities related to the machine at any time during its operation, so as to avoid mounting expensive and fragile sensors on the newly developed drivers.

At first model-based techniques have been developed, rapidly followed by observers. These techniques allowed to run both the synchronous and the asynchronous motor at medium and high speeds with little errors in the position and speed estimation; however, since their operating principle is to make use of flux and back-EMF reconstructions to identify the position of the rotor, they fail at zero or very low speeds, where no back electromotive force is generated and little magnetic flux is present. It is in fact very difficult to derive a precise information about the rotor angular displacement when the measured voltages and currents are very little, due both to microprocessors limitations and intrinsic uncertainty. To this aim IPM synchronous motors, which present a magnetic saliency, started to be studied and developed because their anisotropy could be used to retrieve information both at standstill and at very low speeds. In the following a subdivision into two macro-categories will be made, basically to distinguish techniques that operate at zero or low speed, the so-called *Saliency based methods*, from those which need higher rotational speeds, called *Traditional and model based methods*. Figure 2.1 better explains this subdivision and also describes the sub-categories that come from them.

At first saliency based methods will be analyzed, starting from the most popular high frequency continuous signal injection techniques, which consist of superimposing a carrier signal at high frequency over the fundamental excitation of the motor. An overview on methods based on discontinuous injection will also be made, in addition to techniques that try to esti-

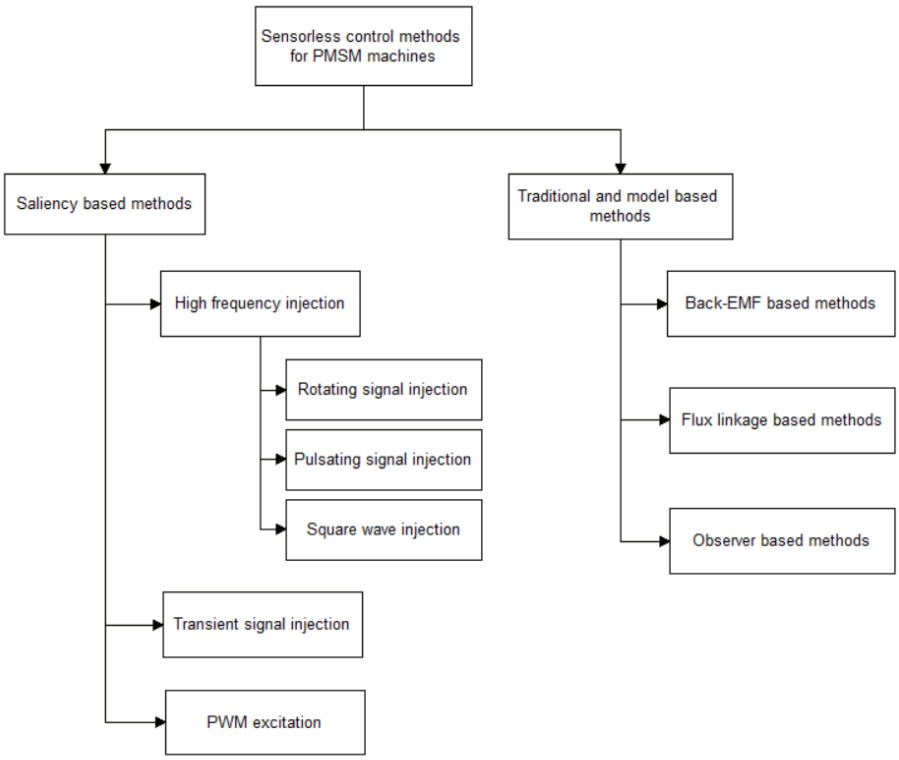

Figure 2.1: Categories of sensorless algorithms

mate the position of the rotor without injecting any signal but retrieving information from the so-called 0 sequence in fundamental excitation. Secondly high speed techniques will be described, such as traditional methods based on a model of the machine, estimators which make use of the magnetic fluxes of the machine and observers of various kinds.

2.2 Saliency based methods

In order to run a control over the PMSM there is the need of a continuous knowledge of the rotor angle. This is due to the fact that the most effective controls work in dq rotating reference frame, thus employing Park conversions that require the rotor angle. In sensorless control the only mea-

sured variables are voltages and currents fed to the motor, from which the necessary informations are taken to retrieve the rotor's angular position. Since the contro has to act from the first moment at which the machine is switched on, but electromotive force is not present at standstill or very low speeds, a difficulty in identifying the mechanical variables arises. Methods based on magnetic saliency, which is an intrinsic characteristic of IPM machines, are then used to overcome this problem.

2.2.1 High frequency continuous signal injection techniques

The most studied and used techniques for identifying the rotor angle at zero or very low speeds is the injection of a high frequency signal, that can be either a voltage or a current (see paragraph 2.2.2), superimposed to the fundamental excitation used to drive the machine. The injected voltage (or current) interacts with the saliency of the machine, generating a current (or voltage) at the same frequency which contains information about the position of the saliency in its phase. In the following voltage injection will be taken as reference as it is the most commonly used signal.
Considering only carrier excitation, the model of the machine is that described in paragraph 1.3.4, in which resistive drops and back-EMF are neglected respectively because of their small amplitude compared to inductive losses and slow rotational velocity. The behavior of the machine in both rotor and stator reference frame can be seen therefore as a purely inductive load with induction matrices given by equations 2.1 and 2.2 depending on the reference frame considered:

$$L_{dq} = \begin{bmatrix} L_d & 0 \\ 0 & L_q \end{bmatrix} \tag{2.1}$$

$$L_{\alpha\beta} = \begin{bmatrix} \Sigma L + \Delta L \cos(h\theta_r) & -\Delta L \sin(h\theta_r) \\ -\Delta L \sin(h\theta_r) & \Sigma L - \Delta L \cos(h\theta_r) \end{bmatrix} \tag{2.2}$$

where

$$\Sigma L = \frac{L_q + L_d}{2} \qquad \Delta L = \frac{L_q - L_d}{2} \tag{2.3}$$

are the avarage and differential stator transient inductances and h is the spatial harmonic order of the magnetic saliency, which is $h = 2$ for an IPM. It is worth to notice that the stator induction matrix 2.2 is just a manpulation of 1.18 and 1.19 by means of equations 1.28 and 1.29.

Two kinds of injection can be applied and take the name of *Rotating injection* and *Pulsating injection*, depending whether the HF signal is superimposed onto stator or rotor reference frame; moreover a variety of signals can be injected, but the most common ones are sines or cosines and square waves.

Rotating injection

The most common approach consists in injecting in stator reference frame a balanced polyphase vector continuously rotating at a high frequency $\omega_c = 200 \div 2000$Hz:

$$\underline{v}_{hf}^{\alpha\beta} = V_{inj} e^{j\theta_c} = V_{inj} e^{j(\omega_c t + \phi)} = V_{inj}(\cos(\omega_c t) + j \sin(\omega_c t)) \tag{2.4}$$

The phase shift ϕ can be any multiple of $\frac{\pi}{2}$.

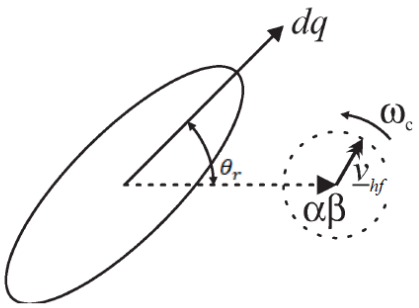

Figure 2.2: Rotating injection method [7]

This voltage injection interacts with the IPM saliency and gives rise to

position-dependent stator currents at the same frequency that can be obtained through mathematical substitutions in the previously recalled model:

$$\underline{i}_{hf}^{\alpha\beta} = I_p e^{j(\omega_c t - \frac{\pi}{2})} + I_n e^{j(-\omega_c t + 2\theta_r + \frac{\pi}{2})} \tag{2.5}$$

It can be noticed that the high frequency currents are made of two components, called *positive* and *negative sequence*, whose coefficients are function of, respectively, the mean and differential stator inductance:

$$I_p = \frac{V_{inj}}{\omega_c} \frac{\Sigma L}{\Sigma L^2 - \Delta L^2} \qquad I_n = \frac{V_{inj}}{\omega_c} \frac{\Delta L}{\Sigma L^2 - \Delta L^2} \tag{2.6}$$

The *positive sequence* component does not contain any useful information about rotor position, while the *negative sequence* is phase modulated by the saliency angle and is therefore employed by several methods to extract an error signal. The more remarkable ones are heterodyning techniques and synchronous filtering; the former make use of frequency multiplication in order to change the frequency of a signal and obtain a better isolation from other spectral components, while the latter consist in transforming the HF measured currents into differently rotating frames, filtering off each time a component of the signal not containing spatial information. The remaining current negative sequence $\underline{i}_{HFn}^{\alpha\beta}$ and the rotor estimated position $\hat{\theta}_r$ are then used to form a phase error by means of vector cross-product

$$\begin{aligned} \epsilon_{\Delta\theta} &= -i_{\alpha HFn} \cos(2\hat{\theta}_r - \omega_c t) - i_{\beta HFn} \sin(2\hat{\theta}_r - \omega_c t) \\ &= I_n \sin(2(\hat{\theta}_r - \theta_r)) \approx 2 I_n \Delta\theta \end{aligned} \tag{2.7}$$

where $\Delta\theta = \hat{\theta}_r - \theta_r$ is the angular error and the last approximation holds for small values of it.

The phase error is fed to a Phase Lock Loop (PLL) or an observer to recursively retrieve the angular position of the rotor.

Pulsating injection

The second class of HF injection consists in superimposing a HF signal over an estimated axis rotating synchronously with the rotor: the corre-

sponding signal vector then appears as it oscillates in a specific direction in space. An arbitrary axis can be chosen between the estimated d^e or q^e, but the d^e axis is commonly preferred because of its lower inductance due to larger air gap, leading to a smaller perturbation of the stator flux and smaller torque ripple. Coherently to this the injected voltage takes the form

$$\underline{v}_{hf}^{dq} = V_{inj} \begin{bmatrix} \cos(\omega_c t + \phi) \\ 0 \end{bmatrix} \tag{2.8}$$

where ϕ can be again any multiple of $\frac{\pi}{2}$.

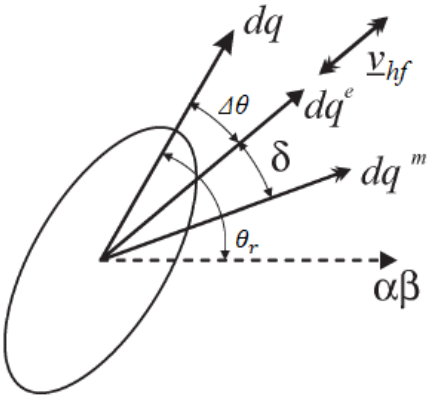

Figure 2.3: Pulsating injection method [7]

The most common injection scheme is the *orthogonal current method*, consisting in taking as measurement frame dq^m the one on which the signal is injected, as depicted in figure 2.3 (with $\delta = 0$). Due to HF impedance difference of d and q axes, if the signal is injected in an estimated frame dq^e which is different from the actual dq one, the voltage component will result not only in the injection axis but also in the other one. Consequently, the generated HF current vector will not be in phase with the injected HF voltage and a current component can be detected on the axis orthogonal to the injection axis (i.e. the q axis for d axis injection). The carrier HF currents are obtained from the interaction between the stator voltage and the spatial

saliency as

$$\underline{i}_{hf}^{dq} = \begin{bmatrix} I_p + I_n \cos(2\Delta\theta) \\ I_n \sin(2\Delta\theta) \end{bmatrix} \sin(\omega_c t) \tag{2.9}$$

The q axis component, which is similar to the error signal found in equation 2.7, is then fed to a PLL to force it to 0, which is equivalent to adjusting the direction of the voltage injection until no current is found in the axis orthogonal to the injection one.

An alternative to the *orthogonal method* described above is the *quadrature method*, consisting in measuring the HF current in a reference frame dq^m shifted by 45° from the estimated injection one, thus with $\delta = 45°$ in figure 2.3. Not many benefits come from this method, which for sure introduces several complications in demodulation.

Rotating synchronous injection

This method is a combination between the two introduced above; it consists in injecting a rotating carrier voltage into the estimated rotor reference frame:

$$\underline{v}_{hf}^{dq^e} = V_{inj} e^{j\theta_c} = V_{inj} e^{j(\omega_c t + \phi)} = V_{inj}\big(\cos(\omega_c t) + j \sin(\omega_c t)\big) \tag{2.10}$$

where $\phi = n\frac{\pi}{2}$, with n integer number.

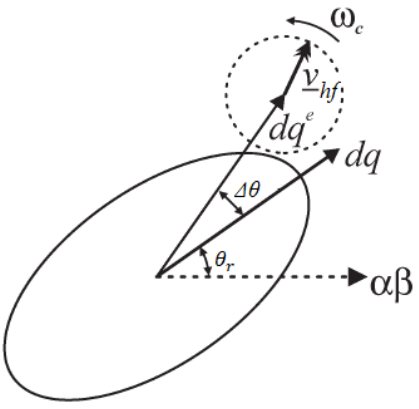

Figure 2.4: Synchronous rotating injection method [7]

The generation of HF currents and their demodulation to obtain an error signal are similar to those described for rotating stationary injection, with the only difference that a position error signal is directly driven from them

$$\underline{\epsilon}_{\Delta\theta}^{dq} = \begin{bmatrix} I_n \cos(2\Delta\theta) \\ -I_n \sin(2\Delta\theta) \end{bmatrix} \tag{2.11}$$

and the estimated position error $\hat{\Delta\theta}$ is obtained through the arctangent function:

$$\hat{\Delta\theta} = \frac{1}{2}\tan^{-1}\left(-\frac{\epsilon_{\Delta\theta}^{q}}{\epsilon_{\Delta\theta}^{d}}\right) \tag{2.12}$$

It is remarkable to notice that this method yields a pair of quadrature position-error signals, hence maximizing the information for a harmonic compensator [7]

Pulsating square wave injection

At last it is worth analyzing one signal injection technique which is not based on sine/cosine waves in order to appreciate the difference with other signals. The second more commonly injected waveform is square wave voltage injectio[11][15]n; current square wave injection is feasible but very uncommon do to the difficulty in generating and managing it. This injection can be done both in stationary and synchronous estimated reference frames, but in this case the reference frame of injection is not relevant as the square wave signal is injected only on one axis (commonly the α axis for stationary and d^e axis for synchronous injection) and the generated current response analyzed on the orthogonal one. In the following synchronous injection will be analyzed in order to remain coherent with the name of this section. The injected voltage can be expressed as follows:

$$v_{hf}^{d^e} = \begin{cases} V_{inj} & 0 < t \leqslant \frac{T_{inj}}{2} \\ -V_{inj} & \frac{T_{inj}}{2} < t \leqslant T_{inj} \end{cases} ; \qquad v_{hf}^{q^e} = 0 \tag{2.13}$$

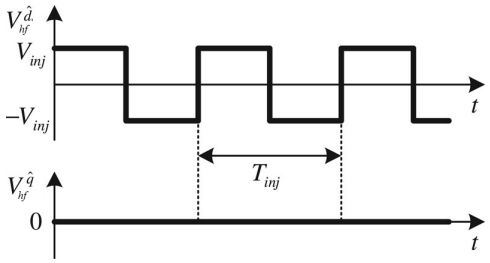

Figure 2.5: Injected square wave [11]

Again neglecting resistive losses and electromotive force and under the assumption that

$$\underline{i}_{hf}^{dq^e} \approx \int \begin{bmatrix} L_d & 0 \\ 0 & L_q \end{bmatrix}^{-1} \underline{v}_{hf}^{dq^e} \tag{2.14}$$

holds, the HF currents can be expressed in stator reference frame as:

$$\underline{\Delta i}_{hf}^{\alpha\beta} = V_{inj} T_{inj} \begin{bmatrix} \frac{\cos(\theta_r)\cos(\Delta theta)}{L_d} + \frac{\sin(\theta_r)\sin(\Delta\theta)}{L_q} \\ \frac{\sin(\theta_r)\cos(\Delta\theta)}{L_d} - \frac{\cos(\theta_r)\sin(\Delta\theta)}{L_q} \end{bmatrix} \tag{2.15}$$

The polarity of injected voltage is hidden in mathematical calculation that have been omitted. Note that the notation Δi implies the current difference over the sampling period, thus implying a derivative operation which is in practice not easy to be realized and has the drawback of being very sensible to noise and disturbances. Finally, under the hypothesis of small errors equation 2.15 can be simplified as

$$\underline{\Delta i}_{hf}^{\alpha\beta} = V_{inj} T_{inj} \begin{bmatrix} \frac{\cos(\theta_r)}{L_d} \\ \frac{\sin(\theta_r)}{L_d} \end{bmatrix} \tag{2.16}$$

leading to an easy calculation of the rotor angle via the arctangent function:

$$\theta_{cal} = \tan^{-1}\left(\frac{\Delta i_{hf}^{\beta}}{\Delta i_{hf}^{\alpha}}\right) \tag{2.17}$$

From this calculation an error signal can be generated and fed to an observer or a PLL in order to minimize it and get a more accurate estimation of the saliency position:

$$\epsilon_{\Delta\theta} = \theta_{cal} - \hat{\theta}_r = \frac{L_q - L_d}{L_q}\Delta\theta \tag{2.18}$$

Using 2.17 and 2.18, θ_{cal} and $\epsilon_{\Delta\theta}$ can be obtained at every sampling instant, with no filtering process. This means that the error signal could be obtained without time delay, which is crucial for extending the bandwidth of a sensorless control. Hence, position estimation performance can be enhanced remarkably [11].

2.2.2 Polarity detection at standstill

The above mentioned methods allow to identify the rotor position at very low rotational speed, but still present a weakness in detecting the right rotor orientation at standstill. In fact, they estimate the position of the saliency quite precisely without giving any information about the polarity, resulting in a possible $\pm$180ř error: the estimation can therefore converge either to the correct $+d$-axis or to the opposite $-d$-axis, which would cause instability in the control of the machine. To overcome this problem and get a correct initial angle estimation a compensation scheme based on stator iron magnetic saturation is needed. The idea behind this compensation is that when the north pole of the PM is aligned with the stator coil, the injected current increases the magnetic flux linked with that coil, which increases stator magnetic saturation and therefore slightly decreases the d-axis inductance; on the opposite, when the current in injected in the south pole, and therefore on the opposite of the d-axis, magnetic saturation decreases and inductance decreases [31]. This phenomenon can be described by considering a saturated flux linkage model of the motor, which simply consists in modelling non-linear d-axis flux linkage or current, depending weather one is injecting a current or voltage signal, respectively. For the first case the flux linkage is approximated by the Taylor series expansion and neglecting terms of order higher than two reads

$$\Psi_d \approx \Psi_m + L_d i_d + \frac{1}{2}\frac{d^2\Psi_d}{di_d^2}(0)i_d^2 + \cdots = \Psi_m + \frac{d\Psi_d}{di_d}(0)i_d + \frac{1}{2}\frac{d^2\Psi_d}{di_d^2}(0)i_d^2 \quad (2.19)$$

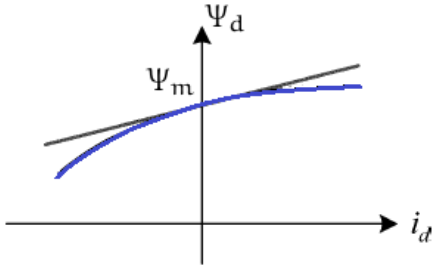

Figure 2.6: Linear (black) and saturated (blue) *d*-axis magnetic flux behaviour [30]

where $\frac{d^2\Psi_d}{di_d^2}(0) < 0$.

When a high frequency current is injected a standstill, neglecting resistance losses, the stator voltages at the positive and negative poles are

$$v_{\pm d} \approx \left(\frac{d\Psi_d}{di_d}(0) \pm \frac{1}{2}\frac{d^2\Psi_d}{di_d^2}(0) i_{\pm d} \right) \frac{di_{\pm d}}{dt} \tag{2.20}$$

In the case of voltage injection, of much more interest in this thesis, it is better to expand in Taylor series the *d*-axis current to highlight the effect of flux linkage

$$i_d \approx \frac{1}{L_d}(\Psi_d - \Psi_m) + \frac{1}{2}\frac{d^2 i_d}{d\Psi_d^2}(\Psi_m)(\Psi_d - \Psi_m)^2 + \dots \tag{2.21}$$

where $\frac{d^2 i_d}{d\Psi_d^2}(\Psi_m) > 0$.

When a high frequency voltage is injected at standstill, the generated current at both poles become

$$i_{\pm d} \approx \frac{1}{L_d}\int v_{\pm d}\, dt \pm \frac{1}{2}\frac{d^2 i_d}{d\Psi_d^2}(\Psi_m)\left(\int v_{\pm d}\right)^2 \tag{2.22}$$

In both current and voltage injection cases the polarity identification can be performed by looking at the sign of the second order terms in eq. 2.20 and 2.22. Notice that the *q*-axis has not been taken in consideration for polarity detection since, assuming zero as the center of its operating point, the related flux linkage is an odd function of the current and therefore has no even-order terms when expressed by the Taylor series with center the origin [28].

Given the above modelling representing the stator iron magnetic saturation, the processing of the generated currents due to a high frequency voltage injection remains the same in order to extract the negative sequence component, carrying the information about the rotor position. The only modification in the algorithm comes from a compensation to the estimation based on the polarity information. In the case of rotating injection, the current bringing this information is obtained by a heterodyning demodulation in the estimated rotor reference frame and reads

$$\begin{aligned} i_{pol} &= 2LPF(BPF(i_{d,est})\cos(2\omega_c t - \hat{\theta}_r) \\ &= -\frac{V_{inj}^2}{8\omega_c^2}\frac{d^2 i_d}{d\Psi_d^2}(\Psi_m)\cos\big(2(\hat{\theta}_r - \theta_r)\big)\cos(\hat{\theta}_r - \theta_r) \end{aligned} \tag{2.23}$$

The sign of this current component depends on the tracked polarity and is used to eventually compensate of $+\pi$ the angle estimation.
In case of pulsating injection, the current component holding the information about the magnetic polarity can be extracted as

$$\begin{aligned} i_{pol} &= 2LPF(BPF(i_{d,est})\cos(2\omega_c t)) \\ &= -\frac{V_{inj}^2}{8\omega_c^2}\frac{d^2 i_d}{d\Psi_d^2}(\Psi_m)\cos^2(\hat{\theta}_r - \theta_r)\cos(\hat{\theta}_r - \theta_r) \end{aligned} \tag{2.24}$$

and it is used the same way as in rotating injection.

2.2.3 Issues caused by non-ideal physical attributes

Now that the main HF injection methods have been described in both their theoretical and practical realization features, an overview about their weaknesses has to be made in order to point out where they could fail during operation and how these lacks can be fixed. In literature the most studied and analyzed weakness is the rising of multiple saliencies in the machine due to constructive features and heavy load operation [6]. Furthermore the effect of cross-saturation and non-negligible stator resistance are considered [8] and their influence on the above introduced methods explained, together with techniques to overcome the related problems [7].

Multiple saliencies

As it has been explained above the injection of a carrier voltage produces a position dependent spatial saliency current. However several factors may interact with the voltage injection, producing additional saliencies that may ruin the behavior of the PLL or the observer and thus the position estimation. Taking as example a voltage injection on induction machines, the presence of multiple saliencies can be represented by the sum of complex current vectors:

$$\underline{i}_{hf} = I_p e^{j(\omega_c t - \frac{\pi}{2})} + \sum_k I_n e^{j(-\omega_c t + k\theta_r + \Phi_k)} \tag{2.25}$$

Odd saliencies ($k = \pm 1, 3, 5 \dots$) have been explained as caused by physical asymmetries in stator windings, eccentricity of the rotor, inverter switching harmonics, aliasing effects in current measurement and other nonlinearities in hardware construction. They are anyway not relevant in magnitude compared to even saliencies ($k = 0, \pm 2, 4 \dots$) induced by magnetic saturation and additional physical spatial saliencies.

To go deeper in detail for an IPM, current components generated by rotating and pulsating voltage injection can be modelled as:

$$\underline{i}_{hf}^{\alpha\beta} = I_p e^{j(\omega_c t - \frac{\pi}{2})} + \sum_k I_{n,2k} e^{j(-\omega_c t + 2k\theta_r + \Phi_k)} \tag{2.26}$$

$$\underline{i}_{hf}^{dq} = \sum_k I_{p,2k} e^{j(\omega_c t + 2k\Delta\theta)} + \sum_k I_{n,2k} e^{j(-\omega_c t + 2k\Delta\theta)} \tag{2.27}$$

In both cases the DC saliency ($k = 0$) is an offset arising from unbalanced current measurement. The main saliency, which is caused by spatial difference between d and q axis inductance, is identified by $k = 1$ and is therefore the one of interest for tracking. The source of all the other saliency ($k = -1, \pm 2, 3 \dots$) with their respective harmonics are asymmetries in machine construction and loaded machine operation. It is worth noticing that the presence of these saliencies also alters the amplitude of positive and

negative current sequences; this amplitude modulation will anyway not affect position estimation as it will cancel out when building the error signal. Although modelling this non-linearity of the IPM is very useful, it is not enough for improving the position estimation and reduce the disturbance on the PLL or the observer. To this means two main processes for saliency decoupling (or harmonic compensation) are employed. The first one is called Space Modulation Profiling (SPM) and consists of storing the corrupting harmonics profile over one full electrical cycle of the rotor at different load condition. This procedure is carried out over time domain and this is helps also to include inverter non-linearities. Once the profiles are identified for different values of the load currents they are simply employed to compensate the error signals during real-time operation. This method is largely employed in rotating carrier injection but presents several difficulties in pulsating injection as the compensation would be function of the angle estimation error, which is continuously updated. To decouple the useless saliencies components in the second kind of injection Kalman filtering is used, with the only requirement of knowing which are the main corrupting harmonics (in literature it is reported that these are the 6^{th} and 8^{th} ones).

Cross-saturation effects

Another non-linearity which affects the behavior of the signal injection is the cross-coupling between the axes of the machine. This effect can be modelled by modifying the high-frequency inductance matrices reported in equation 2.1 and 2.2 as:

$$L_{dq} = \begin{bmatrix} L_d & L_{dq} \\ L_{dq} & L_q \end{bmatrix} \tag{2.28}$$

$$L_{\alpha\beta} = \begin{bmatrix} \Sigma L + \Delta L\cos(h\theta_r) + L_{dq}\sin(h\theta_r) & -\Delta L\sin(h\theta_r) + L_{dq}\cos(h\theta_r) \\ -\Delta L\sin(h\theta_r) + L_{dq}\cos(h\theta_r) & \Sigma L - \Delta L\cos(h\theta_r) - L_{dq}\sin(h\theta_r) \end{bmatrix} \tag{2.29}$$

The cross-coupling matrix in stationary reference frame can be viewed as a special case of multiple saliency as it introduces a current component that travels at the same speed of the HF injection, but with 90^o lag. This results in an angular offset that translates in a mean estimation error between the actual and estimated rotor position. Furthermore, because of the fact that the cross-coupling between the machine axes is load dependent, the estimation error will be itself load dependent:

$$\Delta\theta(i_{load}) = \frac{1}{h}\sin^{-1}\left(\frac{L_{dq}(i_{load})}{\Delta L}\right) \tag{2.30}$$

Stator resistance effect and carrier voltage distortion

At the very begin of this section the assumption of negligible stator resistance under high frequency operation has been made, which is acceptable but not true, as it can be shown that stator resistance affects the rotor position estimation. Furthermore, several researches model the inverter non-linearities as a resistance [13] that corrupts the estimation. To this means it is worth analyzing the effect of such non-ideality on both rotating and pulsating carrier signal injection. Voltage injection will be taken as reference for coherence with the above, but same results hold for current injection.

In case of rotating injection the induced currents in the motor take the form

$$\underline{i}_{hf}^{\alpha\beta} = I_p e^{j(\omega_c t - \frac{\pi}{2} + \phi_p)} + I_n e^{j(-\omega_c t + 2\theta_r + \frac{\pi}{2} - \phi_n)} \tag{2.31}$$

Their amplitude and phase are not function of inductance and rotor speed only, but also include the resistance terms; the following equation are to be

compared with (2.6) for appreciating the difference.

$$I_p = \frac{V_c}{2}\sqrt{\left(\frac{\omega_c L_d}{R_s^2+\omega_c^2 L_d^2}+\frac{\omega_c L_q}{R_s^2+\omega_c^2 L_q^2}\right)^2+\left(\frac{R_s}{R_s^2+\omega_c^2 L_d^2}+\frac{R_s}{R_s^2+\omega_c^2 L_q^2}\right)^2} \tag{2.32}$$

$$I_n = \frac{V_c}{2}\sqrt{\left(\frac{\omega_c L_d}{R_s^2+\omega_c^2 L_d^2}-\frac{\omega_c L_q}{R_s^2+\omega_c^2 L_q^2}\right)^2+\left(\frac{R_s}{R_s^2+\omega_c^2 L_d^2}-\frac{R_s}{R_s^2+\omega_c^2 L_q^2}\right)^2} \tag{2.33}$$

$$\phi_p \approx \frac{R_s(L_d^2+L_q^2)}{\omega_c L_d L_q (L_d+L_q)} \tag{2.34}$$

$$\phi_p \approx \frac{R_s(L_d+L_q)}{\omega_c L_d L_q} \tag{2.35}$$

Because the non-zero stator resistance affects both magnitude and phase of the stator induced currents and the position information is retrieved from the phase of the negative sequence component, the position estimation error results to be a function or the resistance itself

$$\Delta\theta \approx \frac{1}{2}\arctan\left(\frac{R_s(L_d+L_q)}{\omega_c L_d L_q}\right) \tag{2.36}$$

Concerning pulsating injection a carrier current vector can be obtained by superimposing the effects of d and q axis injected voltage as

$$\underline{i}_{hf,v_d}^{dq} = \frac{I_p}{2}e^{j(\omega_c t-\frac{\pi}{2}+\phi_p)}+\frac{I_n}{2}e^{j(-\omega_c t+2\theta_r-2\hat{\theta}_r+\frac{\pi}{2}-\phi_n)} \tag{2.37}$$

$$\underline{i}_{hf,v_q}^{dq} = \frac{I_p}{2}e^{j(-\omega_c t+\frac{\pi}{2}-\phi_p)}+\frac{I_n}{2}e^{j(\omega_c t+2\theta_r-2\hat{\theta}_r-\frac{\pi}{2}+\phi_n)} \tag{2.38}$$

$$\underline{i}_{hf}^{dq} = \underline{i}_{hf,v_d}^{dq}+\underline{i}_{hf,v_q}^{dq} = I_p\sin(\omega_c t+\phi_p)+I_n e^{j2\Delta\theta}\sin(\omega_c t+\phi_n) \tag{2.39}$$

The above equations differ from (2.9) only in the phase shift introduced by the accounting of the stator resistance. The tracking observer used to retrieve the angular position is then driven by the error signal

$$\epsilon_{\Delta\theta} \approx I_n\cos(\phi_n)\sin(2\Delta\theta) \tag{2.40}$$

which is affected by the phase shift only in its magnitude, thus not introducing any position estimation error. This holds true only if a correct extraction of the position information from (2.31) and (2.32) was performed,

using two unit vectors $u_p = e^{j(\omega_c t - \frac{\pi}{2})}$ and $u_n = e^{j(-\omega_c t + \frac{\pi}{2})}$ rotating at the same speed but in different directions. If only one was used the error signal would contain the phase shift induced by the stator resistance in its phase, corrupting the position estimation and resulting in an error way larger than the one obtained with rotating injection.

2.2.4 Comparison between rotating, pulsating and square wave signal injection

In order to assess which injection method is better to apply for performing a sensorless control over an IPM motor, a quick comparison between the above mentioned methods must be performed. The detection algorithms are assessed to be mostly influenced by the number of poles of the machine, magnetic saturation effect, current measurement noise (in case of voltage injection) and time delay into signal demodulation process [21]. The following considerations are obtained with of the same control parameters among different techniques, same injection frequency and magnitude. Concerning the number of pole pairs of the machine, it can be noticed that as they increase the response to the speed estimation becomes faster but in general more oscillating; the rotating injection is the only which shows a better intrinsic damping and less oscillating response. The most critical point for signal injection arises when magnetic saturation occurs, causing the machine saliency ratio to be nearly equal to one ($L_d \approx L_q$) and therefore the loss of the basic principle on which this kind of techniques are based on. It is shown that pulsating and square wave injection become hugely unstable, while rotating injection manages to keep a stable behavior. Concerning measurement noise in current measurement the behavior of rotating and pulsating injection is very likely the same, degrading the estimation as noise increases; square wave injection instead shows a largely worst dependency, due to the differentiation operations needed to extract the po-

sition information. It is remarkable to notice that measurement noise can be almost eliminated by using filtering techniques, like analog filter, which introduce a time delay, and Kalman filters, which are considered the optimal solution. The time delay introduced by current filters, combined with that carried by the demodulation process is also investigated to assess the stability of speed estimation: again, rotating signal injection shows the better performance, while pulsating and square wave injection exhibit an increase of oscillations. Regarding the position estimation, well-tuned *dq* axis injection, either sine wave or square wave, performs better that rotating injection, as it is less influenced non-ideal physical attributes [22]. The difference between injection methods amplifies with the increase of injection frequency. Table 2.1 resumes the comparison between different techniques.

Table 2.1: High frequency injection methods comparison

	Rotating injection	**Pulsating injection**	**Square wave injection**
Implementation	easy	difficult	medium
Pole number effect	small	medium	medium
Saliency effect	medium	high	high
Measurement noise effect	small	medium	high
Time delay effect	less sensible	mid-sensible	very sensitive
Non-ideal physical attributes effect	high	low	medium
Feasible injection frequencies	small	small	high
Accuracy	medium	high	high
Bandwidth	high	medium	medium

2.2.5 Comparison between voltage and current injection

As said above the signal injected into the SPM motor can be either a voltage or a current [12]. Intuitively the two methods are not equivalent in terms of performance and implementation complexity: a voltage injection is easier to produce because the motors are generally driven by three-phase inverters, which can easily implement the injection; the only drawback consists in the fact that the bandwidth of the current regulators must be kept smaller than the carrier frequency in order to not introduce distortion. On the other hand, a current injection has the advantage of producing a larger voltage signal containing spatial information, thanks to the increase in magnitude of impedance with frequency. The latter seems to be a nice feature, but it's important to remark that injecting a high frequency carrier requires a hardware capable to cope with it in terms of generation and acquisition. The current injection therefore must be applied only at high frequencies because of the null advantage brought at low ones, also causing an elevated torque ripple. Other criticalities of current injection are the very tiny spectral separation, which makes the negative component extraction from the fundamental one tough and the need of a very well working regulator capable to precisely regulating the small but high frequency carrier currents further than the fundamental ones. In fact, if the latter is not performed properly, the carrier currents themselves will have both positive and negative components, resulting in a loss of spatial information contained in the generated voltage. To overcome this problem, three solutions can be adopted: increase the control bandwidth, decrease the carrier frequency or adopt a very complex regulating scheme. The first and second are unfeasible due to the too high bandwidth required and loss of effectiveness described above. The third solution appears to be the only applicable one; it consists of splitting the regulation of fundamental and carrier currents, performed by three independent regulators acting respectively on

the synchronous, positive carrier and negative carrier frame. This solution can be slighty simplified by using just one regulator for both the positive and negative carrier sequence. Given the above, the comparison between voltage and current injection techniques comes down to three main points: *processing requirements*, *estimation bandwidth* and *accuracy*.

Processing requirements

To better highlight the processing complexity of the two methods it is useful to describe how the extraction of the information from the generated high frequency currents or voltages is performed. In case of voltage injection and current injection without the complex regulation structure, the negative sequence is extraction is performed as in figure (2.6): firstly the signal is rotated onto the fundamental synchronous frame and an high-pass filter is applied to filter off the fundamental frequency; then the signal is rotated again to the positive sequence carrier synchronous frame and another high pass filter is applied to eliminate the positive sequence. Finally the signal containing only the negative sequence component is rotated back to the stationary reference frame, where the effects of multiple saliencies can be better decoupled. In case of signal injection with the complex regulation scheme the main difference is that one more regulator is used, but the signal used is the voltage command from the output of the carrier current regulator, thus making the filtering of the fundamental frequency unnecessary. After the extraction of the negative sequence has been performed, both injection methods make use of a PLL or an observer to retrieve the angular information. The processing requirements for voltage and current injection are thus very similiar, with no significant difference between them.

Estimation bandwidth

For the case of voltage injection, the estimation bandwidth is directly limited by the observer bandwidth, while one has to remind to set the control bandwidth to be insensible to the carrier injection. Note that a too high estimation bandwidth does not introduce an advantage, also leading to an unstable or more oscillating response. On the other hand, the bandwidth of the observer for the current injection is limited by the carrier current regulators bandwidth: even if the observer was tuned to be faster than the regulation, no appreciable benefit could be noticed. The only way to make the estimation faster would be to increase also the control speed, but a too high carrier control bandwidth negatively affects the fundamental regulator, distorting its bandwidth. To sum up, the tuning of the estimation bandwidth for the current signal injection is of significative higher complexity with respect to the one of voltage injection.

Accuracy

This is probably the point of more interest when it comes to choose whether to perform a voltage or current high frequency injection. Actually, the two methods provide nearly the same results: the voltage injection seems to be the worst one, with little noise on the estimated position and greater estimation error. Current injection, on the other hand, has the advantage of being capable to produce a very clean output signal, especially when compared at non-zero rotor speed. In literature the outcome of the comparisons and the opinion of the authors largely depend on the injection frequency: thanks to the fact that at high frequencies the impedance magnitude increase, when it is possible to cope with them a current injection would be preferred. If the hardware only allows to use an injection below 1KHz probably a voltage injection would be preferable for the simplicity of implementation and tuning.

2.2.6 Transient signal injection techniques

As seen above inverter non-linearities and dead times can badly influence the behavior of continuous signal injection techniques. To this mean an alternative saliency exploiting technique has been developed and takes the name of INFORM (Indirect Flux detection by On-line Reactance Measurement) method. The idea behind it is to apply three impulse voltage vectors during the 0-sequence of a normal PWM period and measuring the corresponding current response. A couple of voltage vectors with opposite direction on the voltage phase plane are applied, so as to have null effect on the output voltage [17]; furthermore, they are not applied in a single PWM cycle because of sampling time restriction, but three PWM cycles are used for one estimation, as shown in figure 2.6.

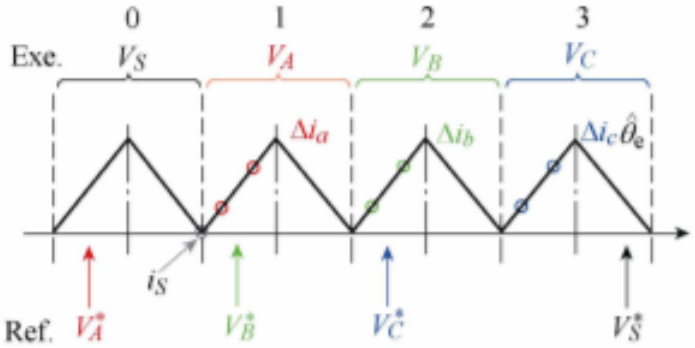

Figure 2.7: INFORM measurement cycle [16]

The current differentiation in stator reference frame is:

$$\frac{di_{\alpha\beta,n}}{dt} = \frac{di_\alpha}{dt} + j\frac{di_\beta}{dt} = \frac{V_{inj}(\Sigma L - \Delta L e^{j2(\hat{\theta}_r - 2n\pi)})}{\Sigma L^2 - \Delta L^2} e^{j\frac{2n\pi}{3}} \tag{2.41}$$

Where $n = 0, 1, 2$ represents the PWM cycles. The rotor position can finally be estimated from the combination C of the three measurements of the cur-

rent phase directions

$$C = \sum_{n=0}^{2} \left(\frac{di_{\alpha\beta,n}}{dt} e^{j\frac{2n\pi}{3}} \right) = \frac{3\Delta L}{\Sigma L^2 - \Delta L^2} V_{inj} e^{j2\hat{\theta}_r} \tag{2.42}$$

$$\angle P = 2\hat{\theta}_r \tag{2.43}$$

It is remarkable to notice that the INFORM method, further than saving inverter losses and distortion effects, also avoids the acoustic noise caused by the injection of a high frequency signal into the machine. As a drawback a very sophisticated and precise hardware is needed to calculate the current derivatives in very small time intervals.

2.2.7 Techniques without signal injection

The last method that is worth analyzing is the application of simple PWM excitation to extract from the currents generated information about the rotor position. This method is commonly applied to IM and surface mounted PMSM where there little saliency, while are generally disregarded for IPM motors because of the applicability of more suitable methods; they have the great advantage of not requiring any kind of further signal injection in the machine as they exploit the normal PWM excitation with SV modulation already applied by the inverter and avoid additional current ripple, higher switching losses and limited dwelling time of zero voltage vector. The idea behind these methods is similar to the one of transient signal injection: as the null voltage vectors $(0,0,0)$ and $(1,1,1)$ are applied during standard PWM operation, current derivative in these time instants can be computed for extracting the rotor position information. The most common approach to the problem is the *zero vector current derivative* (ZVCD) [18]. Under the assumption that there is a angular difference $\Delta\theta$ between the real and estimated *dq* reference frame, the current derivatives take the

form

$$\frac{di_d}{dt} = \frac{R}{L_d L_q}\Big(\big((L_d - L_q)\cos(\Delta\theta)^2 - L_d\big)i_{d,est} + \\ - (L_d - L_q)\sin(\Delta\theta)\cos(\Delta\theta)i_{q,est}\Big) - \frac{k_e\omega_r}{L_q}\sin(\Delta\theta) \quad (2.44)$$

$$\frac{di_q}{dt} = \frac{R}{L_d L_q}\big((L_d - L_q)\sin(\Delta\theta)\cos(\Delta\theta)i_{d,est} + \\ + ((L_d - L_q)\cos(\Delta\theta)^2 + L_q)i_{q,est}\big) - \frac{k_e\omega_r}{L_q}\cos(\Delta\theta) \quad (2.45)$$

Since in general operation the vector controller is set to force $i_{d,est}$ to zero in order to introduce only currents which produce effective torque, the previous equations become

$$\frac{di_d}{dt} = \frac{R(L_d - L_q)}{2L_d L_q}\sin(2\Delta\theta)i_{q,est} - \frac{k_e\omega_r}{L_q}\sin(\Delta\theta) \quad (2.46)$$

$$\frac{di_q}{dt} = \frac{R(L_d - L_q)}{2L_d L_q}\left(1 + \cos(2\Delta\theta) + \frac{2L_q}{L_d - L_q}\right)i_{q,est} - \frac{k_e\omega_r}{L_q}\cos(\Delta\theta) \quad (2.47)$$

Equation 2.40 is of particular interest as it show the current derivative in the estimated *d* axis depends on both the cross coupling due to the machine saliency and to the back-electromotive force. The former is proportional to $\sin(2\Delta\theta)$, the latter to $\sin(\Delta\theta)$ and both could be used to build an error signal from which to retrieve the rotor position. A very basic approach consists in forcing $\frac{di_{d,est}}{dt}$ to zero and hence lock the dq_{est} reference frame to the real rotor frame by means of a PLL.

Many other ways for building a combination of measured current derivatives in response of specific voltage vector for building an appropriate error signal exist in literature [19] [20]. An issue that all the method share is the impossibility to guarantee the minimum duration of the applied voltage vector, since the duty cycle of the PWM is dependent only on the fundamental excitation. To solve this problem several techniques has been proposed, such as edge-shifting or extended modulation.

2.3 Traditional and model based methods

In the previous section feasible methods for retrieving the rotor position at standstill and very low speed have been described in detail. Unfortunately, these methods fail in their purpose at increasing rotor speed because of the limited signal injection frequency and limited PLL and observer's bandwidths. For the high speed operation of SPM machines classical methods based on their model or recently studied observers are used, with very little difference in performance from one to another.

2.3.1 Flux linkage methods

The most classical method used to reconstruct the rotor position from the current measurement is the usage of a stator flux observer, also called *V-I* Estimator, which allows to obtain both stator flux magnitude and orientation information. Starting from equation 1.15 of the IPM in $\alpha\beta$ reference frame and inverting the relationship one obtains the stator fluxes as

$$\begin{cases} \Psi_\alpha = \int (v_\alpha - R_s i_\alpha) dt \\ \Psi_\beta = \int (v_\beta - R_s i_\beta) dt \end{cases} \tag{2.48}$$

Those can be combined to obtain the magnitude of the stator flux

$$\Psi_s = \sqrt{\Psi_\alpha^2 + \Psi_\beta^2} \tag{2.49}$$

and its position

$$\begin{cases} \cos(\theta_s) = \frac{\Psi_\alpha}{\Psi_s} \\ \sin(\theta_s) = \frac{\Psi_\beta}{\Psi_s} \end{cases} \tag{2.50}$$

Deriving the position directly from these equations would anyway lead to an imprecise estimation due to the misalignment of stator and rotor flux caused by the load angle δ. In fact the rotor flux is never perfectly aligned with the stator one, but they are linked by the relationship $\theta_s = \theta_r + \delta$ as

shown in figure 2.7.

There are several methods in literature that allow to identify the correct ro-

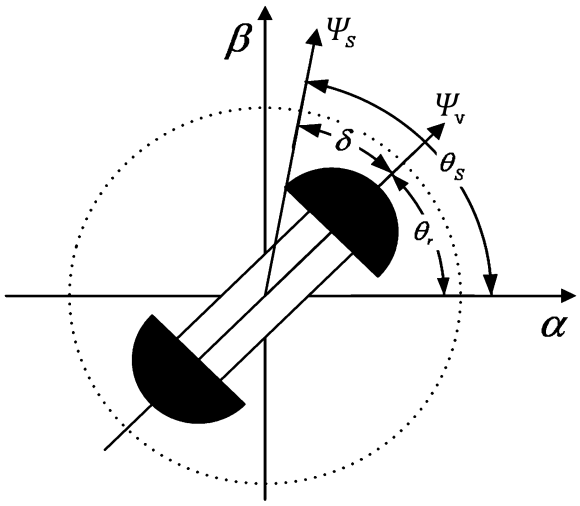

Figure 2.8: Load angle [24]

tor position starting from the reconstruction of the stator flux. One consists in calculating the position of a fictious rotor flux aligned with the permanent magnet flux along the *d* axis[23]. Defining the virtual flux

$$\Psi_v = \Psi_m + (L_d - L_q)i_d \tag{2.51}$$

the saliency of the machine can be rewritten with some manipulation in *dq* coordinates as

$$\begin{cases} v_d = R_s i_d + L_q p i_d - \omega_r L_q i_q + p\Psi_v \\ v_q = R_s i_q + L_q p i_q + \omega_r L_q i_d + \omega_r \Psi_v \end{cases} \tag{2.52}$$

with the associated magnetic fluxes

$$\begin{cases} \Psi_d = \Psi_v + L_q i_d \\ \Psi_q = L_q i_q \end{cases} \tag{2.53}$$

By applying the Park anti-transform, the above equations are translated into stationary $\alpha\beta$ reference frame

$$\begin{cases} \Psi_\alpha = \Psi_d \cos(\theta_r) - \Psi_q \sin(\theta_r) = L_q i_\alpha + \Psi_\nu \cos(\theta_r) \\ \Psi_\beta = \Psi_d \sin(\theta_r) + \Psi_q \cos(\theta_r) = L_q i_\beta + \Psi_\nu \sin(\theta_r) \end{cases} \tag{2.54}$$

and the correct angle estimation is given by

$$\hat{\theta}_r = \tan^{-1}\left(\frac{\Psi_\beta - L_q i_\beta}{\Psi_\alpha - L_q i_\alpha}\right) \tag{2.55}$$

Notice that this estimation is done recursively in open loop, thus without any corrective action on its performance. It can be therefore be schematized as the blue square of figure 2.8. In order to add a feedback for improving

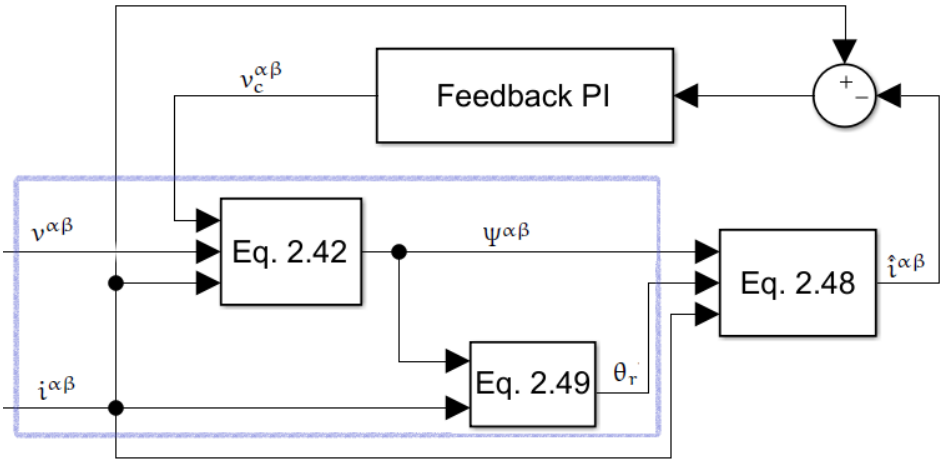

Figure 2.9: Block scheme of a stator flux observer

the rotor position estimation, a current model can be derived from eq. 2.49 and exploited to calculate an estimation of the stator currents. These will be compared with the real measured ones to form an error forced to 0 by a PI or PID regulator. The outcome of this regulator is a compensation term for the stator flux calculator, transforming eq. 2.42 into

$$\begin{cases} \Psi_\alpha = \int (v_\alpha - R_s i_\alpha + v_{c,\alpha}) dt \\ \Psi_\beta = \int (v_\beta - R_s i_\beta + v_{c,\beta}) dt \end{cases} \tag{2.56}$$

Another method used in literature does not make use of the virtual flux construction [25] and is based on a two-stage calculation instead. At first the stator flux is obtained by means of equation 2.42, with the only difference that the feedback is not given by an overall current error, but by direct comparison between the estimated flux from the voltage model $\underline{\Psi}^{\alpha\beta}$ and the one from the flux model in *dq* reference frame, transformed into the stationary frame making use of the Park anti-transform

$$\underline{\tilde{\Psi}}^{\alpha\beta} = \left[T_{Park}(\tilde{\theta}_r)\right]^{-1}\left(\left[T_{Park}(\tilde{\theta}_r)\right](\underline{i}^{\alpha\beta})L^{dq} + \underline{\Psi_M}\right) \tag{2.57}$$

where $\tilde{\theta}_r$ is obtained from

$$\tilde{\theta}_r = \tan^{-1}\left(\frac{\underline{\Psi}^{\alpha\beta} \wedge \underline{\tilde{\Psi}}^{dq}}{\underline{\Psi}^{\alpha\beta} \cdot \underline{\tilde{\Psi}}^{dq}}\right) \tag{2.58}$$

In the second stage an inverted flux model fed with the estimated stator flux is used to retrieve the stator currents, which are compared with the real measured ones to form a current error. Then a dynamical model of the permanent magnets flux linkage is derived from eq. 1.17 and an observer is build using both the current error and flux error obtained in the first stage

$$\frac{d\underline{\hat{\Psi}}_M^{\alpha\beta}}{dt} = \hat{\omega}_r J\underline{\hat{\Psi}}_M^{\alpha\beta} + K_i\underline{e}_i + K_\Psi\underline{e}_\Psi \tag{2.59}$$

where K_i and K_Ψ are 2x2 matrices and $J = \begin{bmatrix} 0 & -1//1 & 0 \end{bmatrix}$.
Finally the rotor position is derived as

$$\hat{\theta}_r = \tan^{-1}\left(\frac{\hat{\Psi}_{M,\beta}}{\hat{\Psi}_{M,\alpha}}\right) \tag{2.60}$$

One last method which can be used consists in a slight modification of the above described method, schematically depicted in figure 2.9. Instead of a constant continuous usage of the flux correction performed by means of eq. 2.51, the pole/zero couple of the feedback regulator is tuned to weight its contribution at different speeds, until the retroaction is completely eliminated over a certain rotating frequency in order to avoid the usage of the estimated rotor position information and save computations [26].

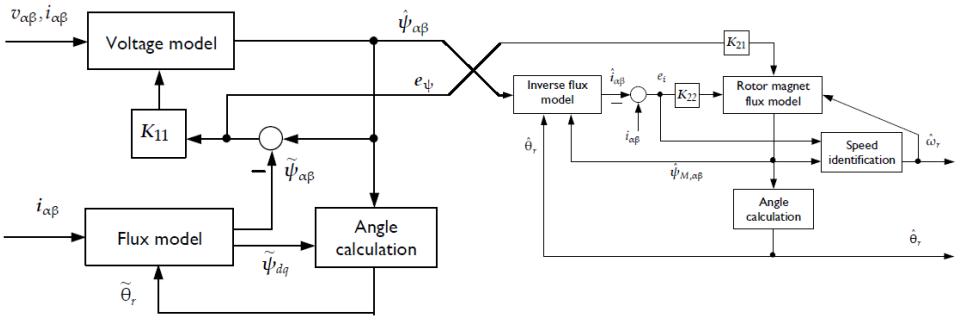

Figure 2.10: Schematic of the alternative flux observer [25]

2.3.2 Observer based methods

Beside flux linkage methods in recent years arose a new technique for estimating the stator fluxes and the rotor position and speed of a PM machine: the usage of state observers, which have their best realization in Kalman Filters (KF), for linear dynamics, and Extended Kalman Filters (EKF), for non-linear dynamics. Those observers work by replicating the system dynamics, adding a correction term proportional to the difference between the real output, given as input, and their estimated one. This closed-loop compensation makes their behavior very robust and insensitive to measurement noise and modelling errors or uncertainties. KF and EKF are moreover considered optimal predictors, in the sense that they minimize the state estimation error variance

Given a generic linear time invariant discrete-time system

$$\begin{cases} \underline{x}(k+1) = F\underline{x}(k) + G\underline{u}(k) + R\underline{v}_x(k) \\ \underline{y}(k) = H\underline{x}(k) + D\underline{u}(k) + Q\underline{v}_y(k) \end{cases} \tag{2.61}$$

where $\underline{x}$, $\underline{u}$ and $\underline{y}$ are the state, input and output vectors, $\underline{v}_x$ and $\underline{v}_y$ are the vectors of modelling uncertainties measurement noises, with associated

covariance matrices Q and R, its predictor is

$$\begin{cases} \hat{\underline{x}}(k+1|k) = F\hat{\underline{x}}(k|k-1) + G\underline{u}(k) + K(k)\underline{e}(k) \\ \hat{\underline{y}}(k|k-1) = H\hat{\underline{x}}(k\text{-}1) + D\underline{u}(k) \end{cases} \tag{2.62}$$

where $K(k)$ is a time-varying gain matrix and $\underline{e}(k) = \underline{y}(k) - \hat{\underline{y}}(k)$ is the so called *innovation* term. The estimation is then performed recursively in two steps: firstly the new state vector is predicted based on its previous value, together with the gain matrix to be applied, and secondly the state estimation is corrected by means of the innovation term, which represents the "correctness" of the estimation: in fact, if the estimated output given by the estimated state vector is close to the real output, the innovation term will be small, resulting in a barely null correction of the state prediction. In Kalman filters the gain is provided by $K(k) = F(k)P(k)H(k)^T\left(H(k)P(k)H(k)^T + R\right)$ and $P(k)$ is provided by the Riccati equation.

The above results can be generalized to a non-linear system simply by implementing time-varying matrices F, G, and H (matrix D is generally considered null) that must be evaluated at any time with the estimated state vector.

In view of the theory described above, many realizations have been performed in literature to deal with rotor position estimation. Some authors implemented a linearized system with 2 [27] or 4 [28] state equations in order to obtain a optimal estimation of the stator fluxes from which to retrieve the rotor position information. In these researches flux equations have been implemented in stator reference frame, feeding the predictors with measured currents and input voltages, leading in a very precise estimation of the stator fluxes, consequently used in flux linkage techniques to obtain the rotor position.

A different approach have been followed in [29]: the non-linear system in *dq* coordinates has been implemented beside two state equation for the prediction of rotor position and speed, scarifying computational complexity

on behalf of a more complete and precise algorithm. The overall system is described by

$$\begin{cases} \begin{bmatrix} \dot{\Psi}_d \\ \dot{\Psi}_q \\ \dot{\omega}_r \\ \dot{\theta}_r \end{bmatrix} = \begin{bmatrix} -\frac{R_s}{L_d}\Psi_d + \omega_r\Psi_q + \frac{R_s}{L_d}\Psi_m + \nu_\alpha\cos(\theta_r) + \nu_\beta\sin(\theta_r) \\ -\omega_r\Psi_d - \frac{R_s}{L_q}\Psi_q - \nu_\alpha\sin(\theta_r) + \nu_\beta\cos(\theta_r) \\ 0 \\ \omega_R \end{bmatrix} \\ \begin{bmatrix} i_\alpha \\ i_\beta \end{bmatrix} = \begin{bmatrix} \frac{\Psi_d - \Psi_m}{L_d}\cos(\theta_r) - \frac{\Psi_q}{L_q}\sin(\theta_r) \\ \frac{\Psi_d - \Psi_m}{L_d}\sin(\theta_r) + \frac{\Psi_q}{L_q}\cos(\theta_r) \end{bmatrix} \end{cases} \tag{2.63}$$

and the gradient matrices used for the implementation of the EKF are

$$\begin{aligned} F\big(\hat{x}(t),t\big) &= \left.\frac{\delta f\big(x(t),u(t),t\big)}{\delta x^T(t)}\right|_{x(t)=\hat{x}(t)} \\ &= \begin{bmatrix} -\frac{R_s}{L_d}\Psi_d & \omega_r & \Psi_q & \nu_\alpha\sin(\theta_r) + \nu_\beta\cos(\theta_r) \\ -\omega_r & -\frac{R_s}{L_q} & -\Psi_d & -\nu_\alpha\cos(\theta_r) - \nu_\beta\sin(\theta_r) \\ 0 & 0 & 0 & 0 \\ 0 & 0 & 1 & 0 \end{bmatrix} \end{aligned} \tag{2.64}$$

and

$$\begin{aligned} H\big(\hat{x}(t),t\big) &= \left.\frac{\delta h\big(x(t),t\big)}{\delta x^T(t)}\right|_{x(t)=\hat{x}(t)} \\ &= \begin{bmatrix} \frac{1}{L_d}\cos(\theta_r) & -\frac{1}{L_q}\sin(\theta_r) & 0 & -\frac{\Psi_d - \Psi_m}{L_d}\sin(\theta_r) - \frac{\Psi_q}{L_q}\cos(\theta_r) \\ -\frac{1}{L_d}\sin(\theta_r) & \frac{1}{L_q}\cos(\theta_r) & 0 & \frac{\Psi_d - \Psi_m}{L_d}\cos(\theta_r) - \frac{\Psi_q}{L_q}\sin(\theta_r) \end{bmatrix} \end{aligned} \tag{2.65}$$

Chapter 3

SIMULATIONS AND RESULTS

The aim of this chapter is to describe the setup used for running the simulations, together with its implementation and the results obtained.

3.1 Simulation components built in Simulink

In this section the models built in Simulink environment will be reported and described in order to give a full view over the control scheme adopted to run the IPM synchronous machine's simulation of the sensorless control. All the blocks adopted can be found in the Simulink Standard library, Control System toolbox and Digital Signal Processing toolbox.

3.1.1 IPM linear model

The first step was to build a model of the IPM motor. Both linear models described in section 1.3.5 were developed and tested to assess their equality. Both take as input the two phases stator voltage in rotor reference frame $\underline{v}^{dq}$ (which can be obtained by means of Park transform) and the rotor electrical speed ω_e and output the stator fluxes $\underline{\Psi}^{dq}$ and currents $\underline{i}^{dq}$. In

the simulation stage only the current model has been used thanks to its strenght of not requiring pre-charging of the integrator providing the *d*-axis flux linkage.

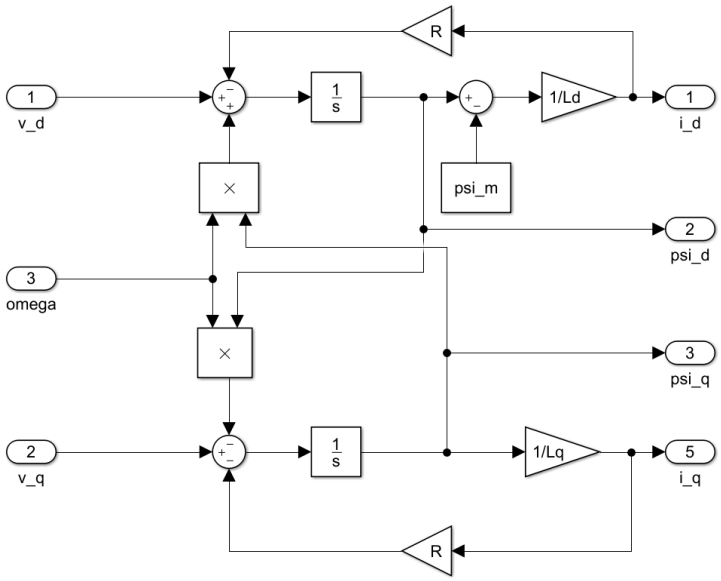

(a) *Flux model*

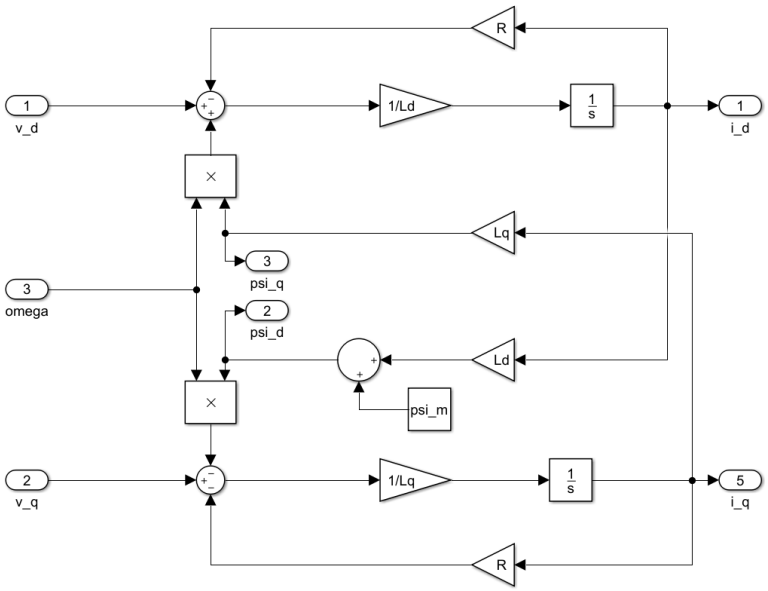

(b) *Current model*

Figure 3.1: IPM motor models

The models are built using the IPM motor characteristic equation assuming a linearity of the parameters, which are reported in table 3.1.

Table 3.1: Simulation parameters

Symbol	Description	Value
R_s	Winding resistance	$8.7[m\Omega]$
L_d	*d*-axis inductance	$65[\mu H]$
L_q	*q*-axis inductance	$150[\mu H]$
Ψ_m	Magnetic flux linkage	$9.1\left[\frac{V}{1000rpm}\right]$
$V_{s,max}$	Maximum phase voltage	$\frac{1}{\sqrt{2}\sqrt{3}}48[V]$
$I_{s,max}$	Maximum phase current	$250[A]$
ω_{max}	Maximum speed	$6000[rpm]$
n_p	Number of pole pairs	4
J	Overall inertia	$0.1[Kgm^2]$
$beta$	Friction coefficient	$0.0005\left[\frac{Kgm^2}{s}\right]$

3.1.2 IPM non-linear model

The linear model of the IPM described above allows to simulate a control over the motor, further than the sensorless identification of position and speed at both low to high speeds. In order to simulate also the standstill polarity identification of the rotor, a non-linear model of the IPM was to be designed. To this means a LUT (Look Up Table) was designed to implement a dependency of *d*-axis inductance from *d*-axis current. It's remarkable to notice that at standstill the control is not active, thus the only currents induced into the motor are driven by the high frequency voltage injection of few volts. This means that their magnitude will be small ($20-30$ [A] at maximum) and the implemented non-linearity will not be exploited completely. One should also remind that when tuning the control scheme, which will

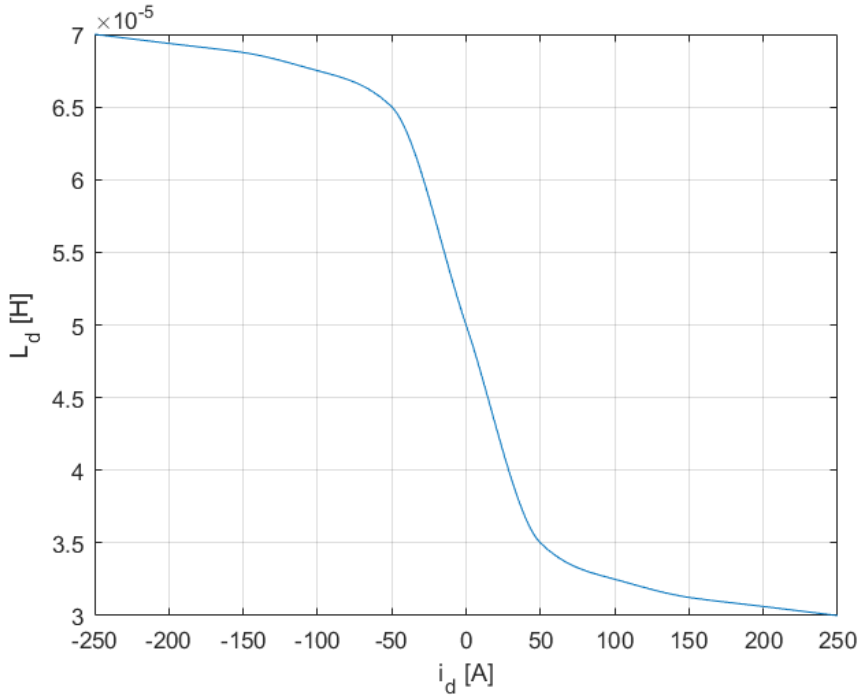

Figure 3.2: L_d dependency on *d*-axis current

be analyzed hereafter, this non-linearity must be taken into account in order for it to work effectively.

3.1.3 Coordinate transformations

The above mentioned models require as input quantities described into rotor reference frame. This choice has been done for simplification in the implementation but is actually not feasible in practice, as *dq*-axis voltages and currents are not measurable. To overcome this problem and transform physical three-phase voltages, currents and magnetic fluxes into two phase stationary or rotating orthogonal reference frames (and vice-versa), Clark and Park transforms and anti-transforms have been implemented by means of "function" blocks. This allows to feed the model with three-phase voltages and measure three-phase currents, of greater practical meaning. No-

tice that having at disposition a rotational transducer would hide the need of Clark transforms, since the rotor angle would be known precisely at any time and the control scheme could be simulated directly with the position information driven by the model. However, the aim of this work is to identify the position of the rotor without a transducer, thus the transformation by means of the estimated angle of voltages to feed the motor and of the currents measured to feedback the controls plays a crucial role to assess the performance of the studied methods.

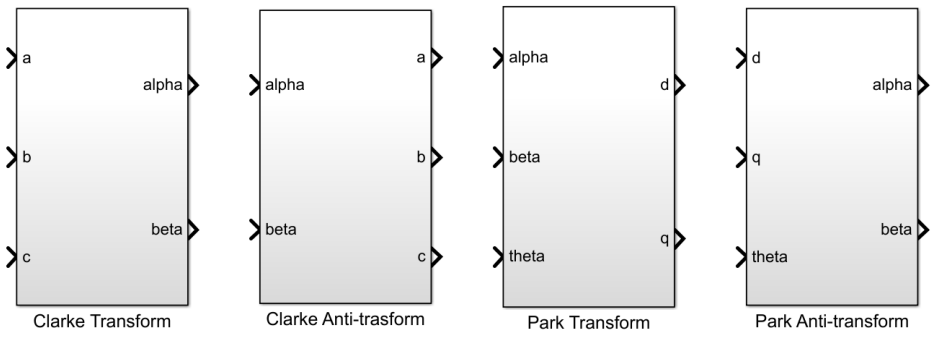

Figure 3.3: Coordinate transformations

3.1.4 Torque production model

Furthermore, two models for simulating the torque production and the operating behavior under a load torque were created and can be seen as attached in cascade to the motor model; they are reported in figure 3.2: For the first, equation 1.44 was used, while the second derives from a simple energy balance at the shaft of the motor:

$$J\dot{\omega}_m + \beta\omega_m = np(T_e - T_l) \tag{3.1}$$

where J is the rotor inertia and the parameter β represents the friction coefficient, which can be either found by a parameter identification or considered small and neglected.

Finally a last manipulation has to be made on the model in order to make it

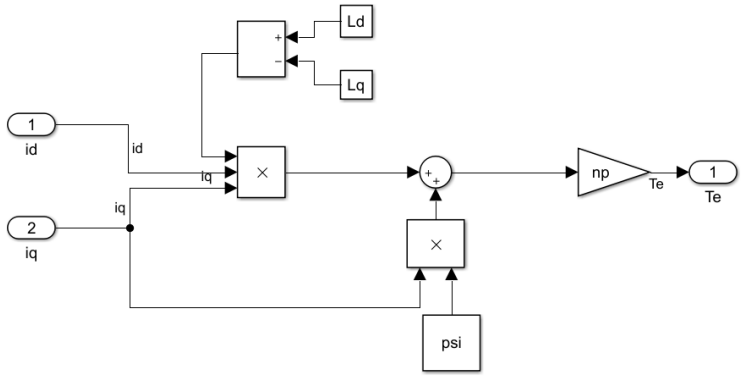

(a) *Torque model*

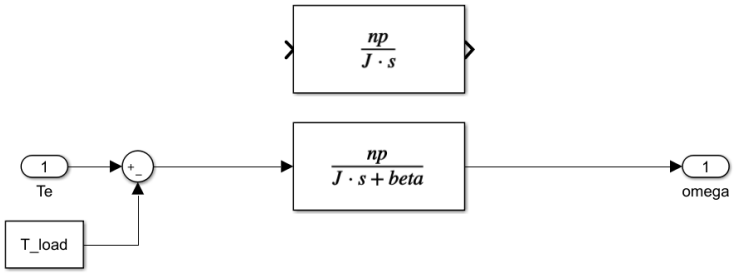

(b) *Load model*

Figure 3.4: Torque and load models

coherent with the sensorless operation: no speed, torque or position transducer is in fact available in the developed application and therefore the motor has to be fed with a three-phase voltage coming from the inverter, while the only quantities available to measure are the three-phase currents generated (or, alternatively, the quantities in $\alpha\beta$ coordinates coming from Clarke transforms); to this means the motor and torque models into *dq* reference frame have been connected and enveloped into Park transform and anti-transform, which make use of fictious and non-accessible position information coming from the speed integration. The complete machine model is therefore shown in figure 3.5, where the blu square delimits the non physically accessible variables. Note that the integrator is *wrapped*, meaning that

the position only varies between 0 and 359 degrees to better emphasize the rotation or the rotor.

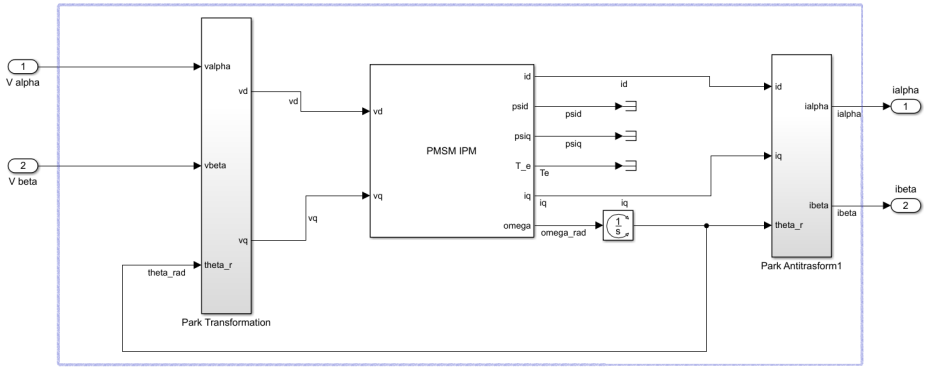

Figure 3.5: Sensorless full IPM machine model

3.1.5 Control scheme

In order to test and validate the models created for the motor, a basic control scheme has been developed and implemented in Simulink. It consists of a cascade control, with outer speed loop and inner current control loops. The former compares the electrical speed setpoint with the feedback and calculates a reference torque for the motor. This, by means of LUT compiled with the MTPA (Maximum Torque Per Ampere) theory [32], is transformed into optimal current setpoints in *dq* coordinates and fed to the inner control loop. The latter generates two current errors (one for each axis) and calculates the input voltage to be applied to the motor by the power converter stage. The transfer function from speed to torque and from currents to voltages read

$$\frac{\omega_e}{T_m} = \frac{n_p}{beta + sJ} \qquad \frac{i_d}{v_d} = \frac{1}{R_s + sL_d} \qquad \frac{i_q}{v_q} = \frac{1}{R_s + sL_q} \tag{3.2}$$

With time constant, respectively,

$$\tau_{\omega_e} = \frac{J}{beta} \qquad \tau_{i_d} = \frac{L_d}{R_s} \qquad \tau_{i_q} = \frac{L_q}{R_s} \tag{3.3}$$

Note also that the speed considered is the electrical one, linked to the mechanical speed by the relationship $\omega_e = n_p \omega_m$.

The PI regulators are tuned simply by cancelling the pole of the transfer functions and replacing it with a faster one to achieve the desired performance. Those are obtained starting from the inner loop: since the current regulators, in view of the signal injection, should be insensitive to the high frequency currents, they are tuned to have a bandwidth of 40Hz. It follows that the outer loop, which should be at least one decade slower that the inner one, is tuned to have a 0.4Hz bandwidth. As it can be noticed the performance of this control scheme has been disregarded in view of a higher robustness to signal injection. Finally, it is important to remark that all PI regulators are built using an anti-windup structure in order to avoid the over-charging of integrators during saturation and delays in the control action. A simulation of the controlled motor is reported in figure 3.6, which shows how the speed and current loops work as desired. It is remarkable to notice that the 150Hz setpoint to the electrical speed highlights how the base speed of the motor is around $120 \div 130$Hz, as one can notice from the knee in the speed response. Above that rotational velocities the control scheme should include a flux weakening, but this is not in the interest of this thesis.

The complete control scheme is reported in figure 3.7; it supposes the presence of a rotational transduced to obtain rotor position and speed and the operation is therefore non-sensorless. The sensorless identification algorithms are firstly run in parallel to this scheme and only subsequently implemented in a simulated sensorless control.

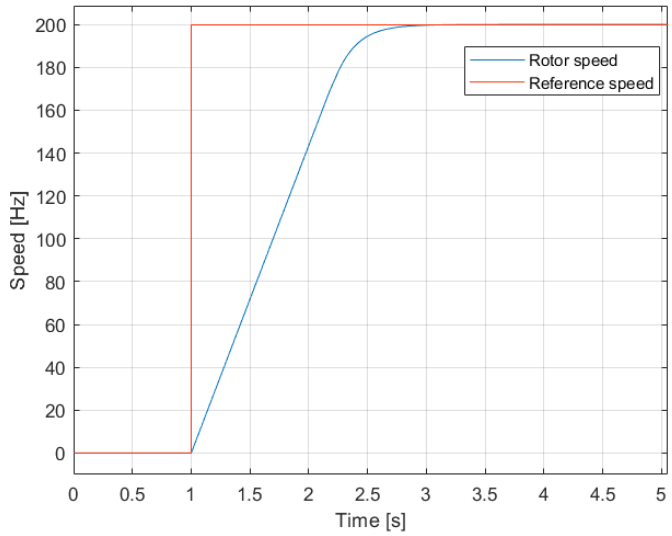

(a) *Speed response*

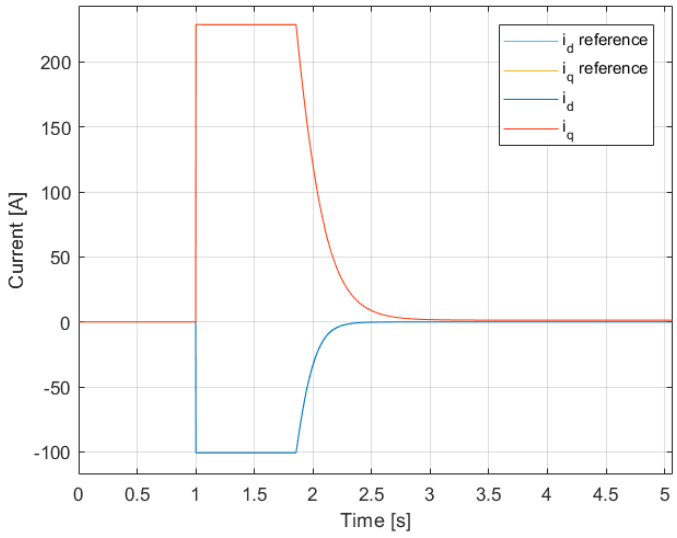

(b) *Current response*

Figure 3.6: Sensored control

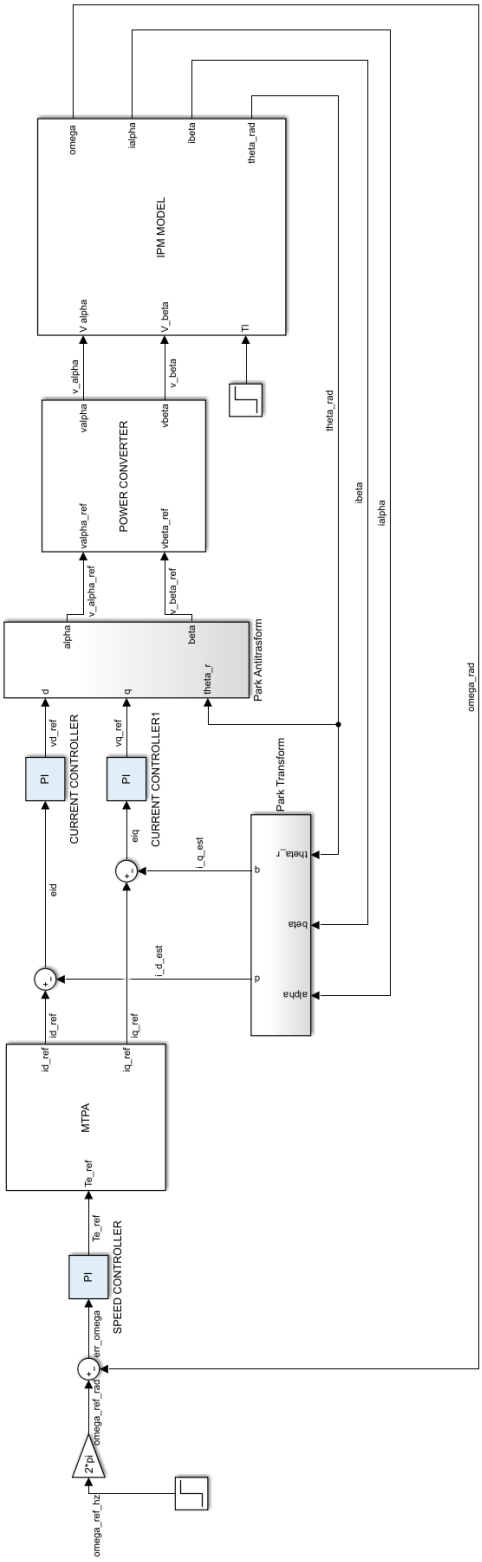

Figure 3.7: Control scheme

3.2 Sensorless control at standstill to low speeds

In this section the algorithm used to retrieve the angular position and speed of the rotor exploiting the IPM saliency will be described. The choice fell on a rotating voltage injection since from the literature research it seemed to be the best in the tradeoff between complexity, robustness and performance. The injection parameters are chosen as in table 3.2; the injection frequency is limited in view of the sampling time of the hardware that will be used in the experiments, while the amplitude is decided according by the generated currents: even though the error in the estimation is not dependent on the current amplitude, it is better for the fixed point microprocessor that will be used in experiment not to work with very small quantities. Of course, a higher voltage applied results in higher currents generated and a greater rotation of the motor, but a 90° rotation in 10 seconds has been considered acceptable, also considering that the estimation should be performed in several milliseconds.

Table 3.2: High frequency injection parameters

Parameter	Value
v_{inj}	10[V]
f_{inj}	800[Hz]

3.2.1 Signal analysis

Given the above injected signal, with no control acting over the machine, the generated currents into $\alpha\beta$ reference frame are shown in figure 3.8. It is evident how the phase of the generated currents exhibits a distortion due to the saliency; moreover, their magnitude is different due to the difference inductance on the injection axis: a lower inductance on the α-axis results in fact in a greater current. The saliency of the rotor can be analyzed

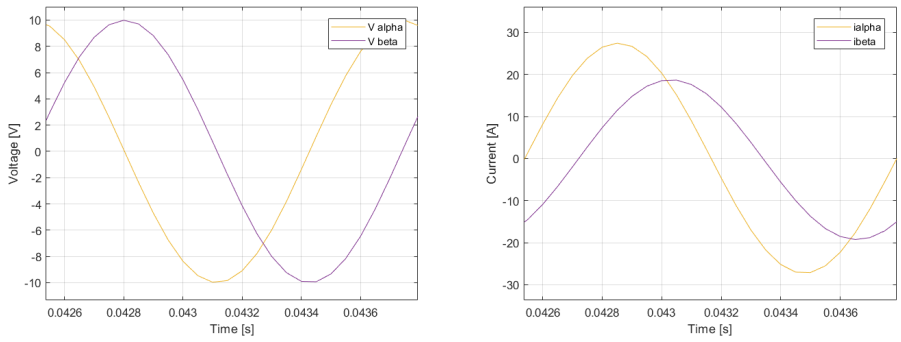

(a) *Injected voltages* (b) *Generated currents*

Figure 3.8: High frequency injection

by plotting one current versus the other for different rotor positions. Analyzing figure 3.9 one can notice that the position information is of course present in the currents generated by the high frequency injection. One last analysis must be performed on the signal before proceeding to demodulation: the spectrum of the currents must be analyzed to verify that the signal contained is at the frequency predicted by theory. To this means two set of simulation will be considered; the first one is performed at zero-speed, while in the second the rotor is brought by the control at $\omega_e = 30$Hz. The resulting spectra, obtained by means of a FFT (Fast Fourier Transform) of the signal, are reported in figure 3.10 for the current i_α.

From the spectral analysis it is evident how at standstill the current only has the high frequency injection component, while, when the motor is rotating, also lower frequencies arises (figure 3.9c) until the rotational speed. Note also from figure 3.9d that the saliency of the motor moves the high frequency component by a factor of $2\omega_e$.

3.2.2 Signal demodulation

Once that the signal carrying the position information have been analyzed, a demodulation scheme for extracting the useful components must

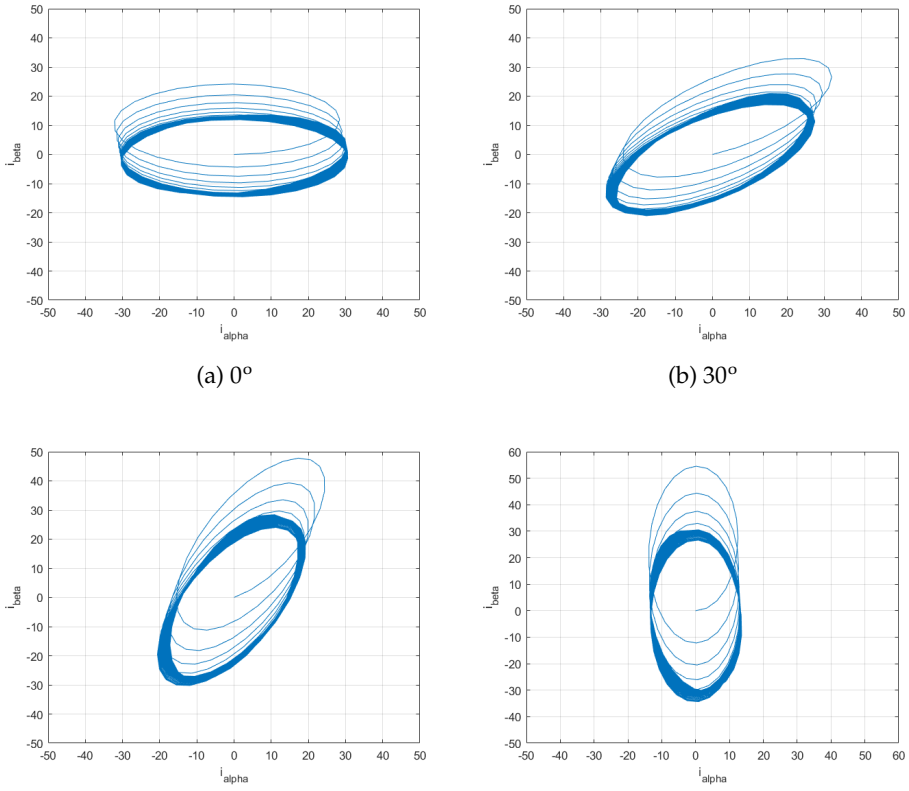

(a) 0° (b) 30°

(c) 60° (d) 90°

Figure 3.9: Saliency information contained in $i^{\alpha\beta}$ for different rotor positions

be designed.

Position information

Concerning the isolation of the signal carrying the saliency position information, the measured currents in stator reference frame are transformed into axis rotating at the frequency of injection. Doing so allows to decouple three components: the fundamental frequency introduced by the speed control, rotating at $(\omega_c - \omega_e)$Hz, and the positive and negative components introduced by the high frequency injection, respectively at 0Hz and $2(\omega_c - \omega_e)$Hz. Since the useful information is contained only in the nega-

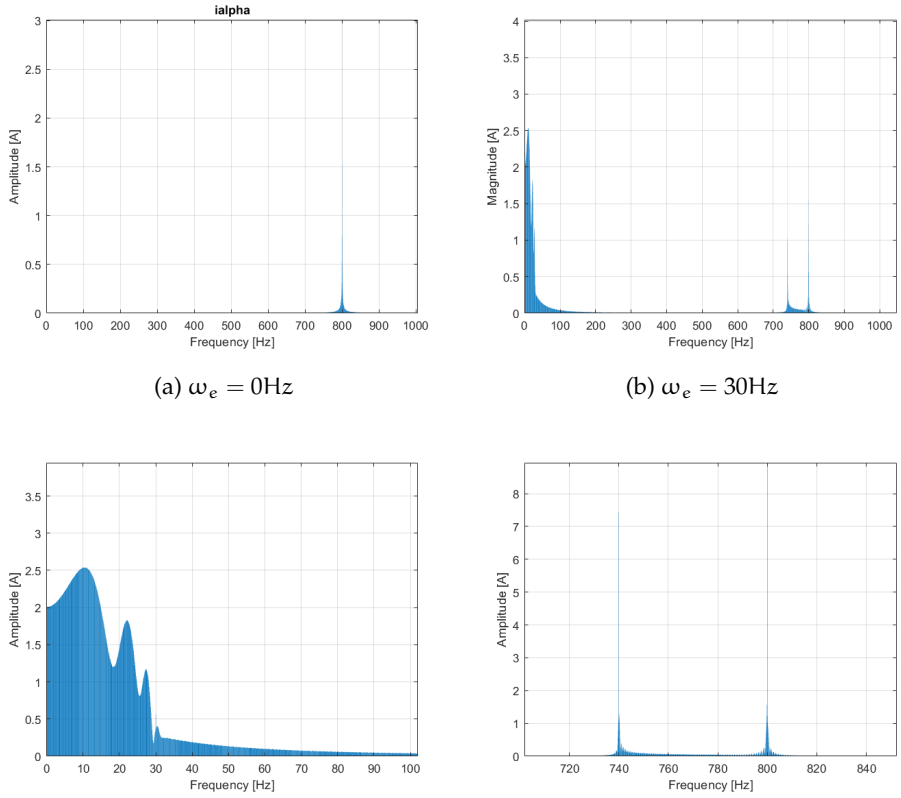

(a) $\omega_e = 0$Hz

(b) $\omega_e = 30$Hz

(c) $\omega_e = 30$Hz,
focus on low frequencies

(d) $\omega_e = 30$Hz,
focus on high frequencies

Figure 3.10: Spectral analysis of i_α under HF injection

tive sequence, a high pass filter is designed to get rid of the slow components. Alternatively, a pass-band filter can be implemented to cut-off also the high frequency harmonics of the signal, resulting in a cleaner demodulation. The frequency and order of the mentioned filters are chosen according to the desired operational range of this estimator: since the goal is to obtain the position estimation from standstill to a rotational speed high enough for the flux observer to work properly, which will be proven to be 10Hz, several simulations are carried out to explore different possibilities. Figure 3.11 shows the result of simulating the complete estimation algorithm (thus it is a tuning done at posteriori) with four different pass-band

filters at different rotational speeds. The simulations are started with the motor at standstill and every four seconds it is accelerated of 5Hz.

Results show how an increase of the pass-band towards the lower fre-

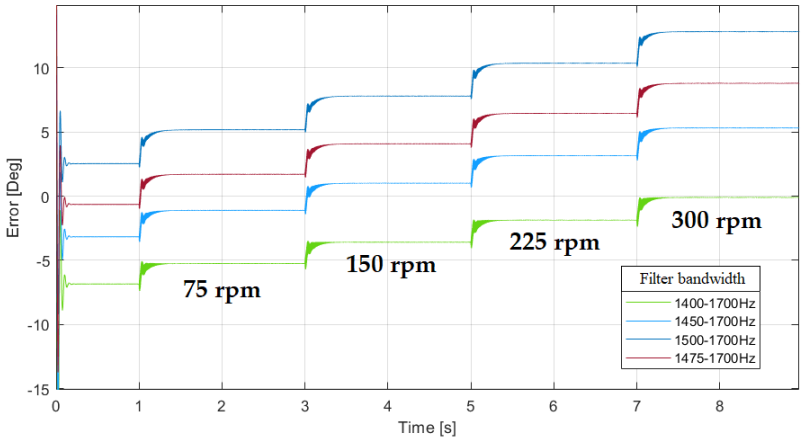

Figure 3.11: Estimation error with different pass-band filters at different speeds

quencies decrease the estimation error at lower rotational speeds. Simulations with an increase of the pass-band towards higher frequencies have not been reported because, due to the missed rejection of signal harmonics, the estimation error tends to be higher and growing faster with speed. Furthermore, higher order filters have been discarded due to the delays introduced and to the higher hardware requirements in view of experimental implementation. The final choice fell of the pass-band $1475 \div 1700$, which allows to commit an error lower that 1 degree at standstill, growing to 4 degrees at 10Hz, which seems a reasonable performance.

After the signal has been filtered, it is rotated back to the stationary reference frame, where vector cross-product is performed in order to build an error feasible of being fed to a PLL or a position observer. The overall demodulation scheme is depicted in figure 3.12; it also includes the polarity detection algorithm described hereafter.

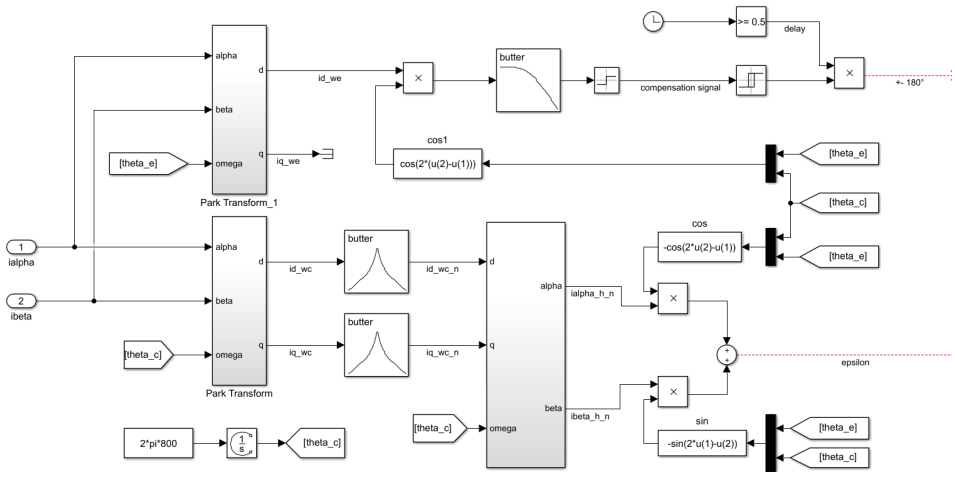

Figure 3.12: Position and polarity signal demodulation

Polarity information

As explained in chapter 2.2.2, identifying the position of the rotor is not enough for a robust control because of the 180° uncertainty about the estimated *d*-axis. To this means the current in $\alpha\beta$ reference frame are used in another demodulation algorithm, which works in parallel with respect to the previously explained one and has the aim of extracting a polarization information to correct the rotor position estimation. This demodulation consists in rotating the signal synchronous to the estimated rotor frame and apply an heterodyning technique to isolate the desired frequency, which is dependent to the difference between the real and estimated rotor position. The signal is then low-passed to discard higher frequencies and its sign contains the desired information: if it is greater than 0 the estimation should be corrected on $+\pi$, otherwise the identified saliency estimation is already correct. The low-pass filtered is tuned to cut frequencies below 5Hz in view of the fact that the estimation is corrected only after having converged to a stable value, thus the difference $(\theta_r - \hat{\theta}_r)$ is almost at zero-frequency. Mind that to simulate this part of the algorithm the implementation of the inductance non-linearity, at least on the *d*-axis is strictly necessary, as it relies on

the magnetic saturation effect to detect the sign of the higher-magnitude current peaks.

Figure 3.13 shows some example of active and inactive compensation: it

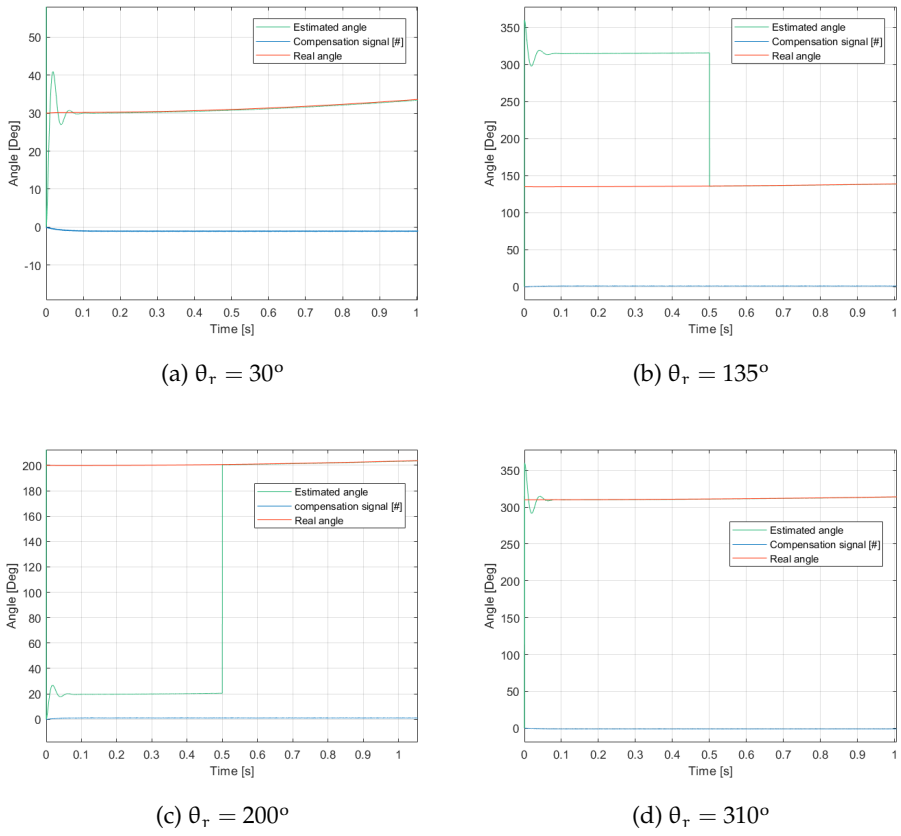

(a) $\theta_r = 30^o$ (b) $\theta_r = 135^o$

(c) $\theta_r = 200^o$ (d) $\theta_r = 310^o$

Figure 3.13: Examples of polarity correction

can be noticed that the algorithm misses the polarity identification in the second and third quarter of the Cartesian plane, while the rotor polarity is estimated correctly in the first and fourth quarters. Once that the estimation has been corrected by means of the polarity detection, the second demodulation scheme can be disregarded because the basic algorithm will manage to keep linked with the correct polarity.

3.2.3 Rotor position and speed estimation

The demodulation algorithms described in the previous paragraphs make use of a position estimation feedback. For them to work properly it is thus necessary to complete this estimation, starting from the error and compensation signals obtained in section 3.2.2. The former is fed to a PLL, which is basically a PI regulator, that outputs the rotational speed of the saliency: the position estimation is therefore achieved by integration. The latter is applied on the estimation only after it converged to a stable value. For tuning the regulator, it is convenient to analyze the spectrum of the error signal in order to assess where to place its zero. It appears that the spectrum has three main components: the first at very low frequencies $(0 \div 50\text{Hz})$, the second at $(\omega_c - \omega_e)\text{Hz}$ and the third at $2(\omega_c - \omega_e)\text{Hz}$. Since the second and third components only arise because of the frequency multiplication introduced by the cross-product used to build the error, all the useful information is contained in the first component, generated by the displacement between the real and estimated position. The zero of the PI is therefore placed by trial and error in order to obtain a time constant $\tau_z \approx 200\frac{\text{rad}}{\text{s}}$ and to avoid as much as possible oscillation in the estimation.

Concerning the speed estimation, which should be used as feedback in a sensorless control, the one obtained as output from the PLL results of being very noisy and not precise. To this means three approached have been implemented to retrieve a clean estimation: *discrete time derivative*, *cascade PLL* and *discrete-time Kalman filtering*. The former simply consists in a differentiation of the position signal, while the second consists in a second PLL connected in cascade to the first one, fed with the difference between the estimated position and a fictious position generated by himself and used as feedback. Both methods are precise but suffer of the "spiking" problem: since both position information are wrapped over the range $0 \div 360^o$ (to give it a physical meaning and in view of avoiding the problem of overflow

in the implementation on a microprocessor) and are not precisely aligned (principle on which the PLL bases its working behavior), when one jumps to 0^o the resulting error experiences an instantaneous spike of $\pm\pi$ and the speed estimation therefore tends to inf. Figure 3.14 shows this problem.

To fix this issue a discrete time function to be triggered at the desired fre-

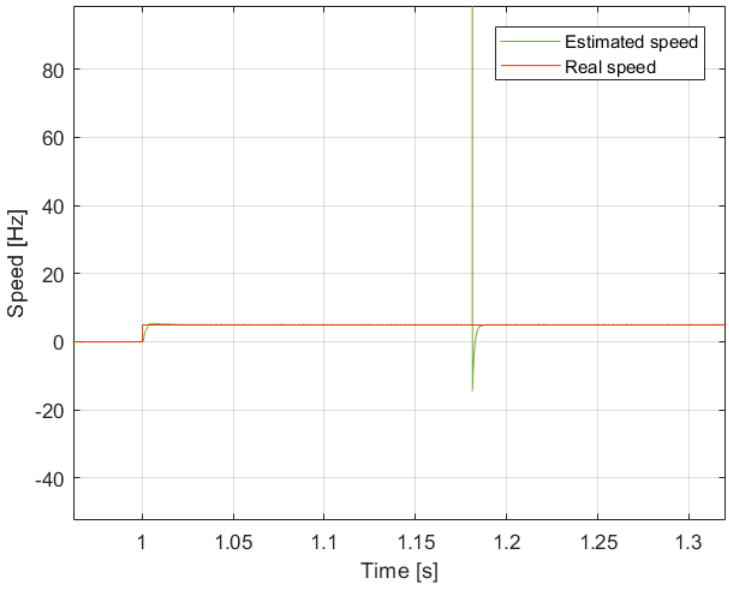

Figure 3.14: Spikes in speed estimation

quency has been created: it takes as input the current and previous values of the two angular positions, obtained by means of unitary delays, and detects the instants at which those are wrapped to 0^o. Doing so, by means of logic operators, allows to compensate of $\pm\pi$ the angular error and avoid the spikes. This method applies both to the cascade PLL and the discrete time triggered differentiation. The obtained results are shown in figure 3.15 for speed estimation up to 30Hz, thus well above the limit at which the observer-based control should take over.

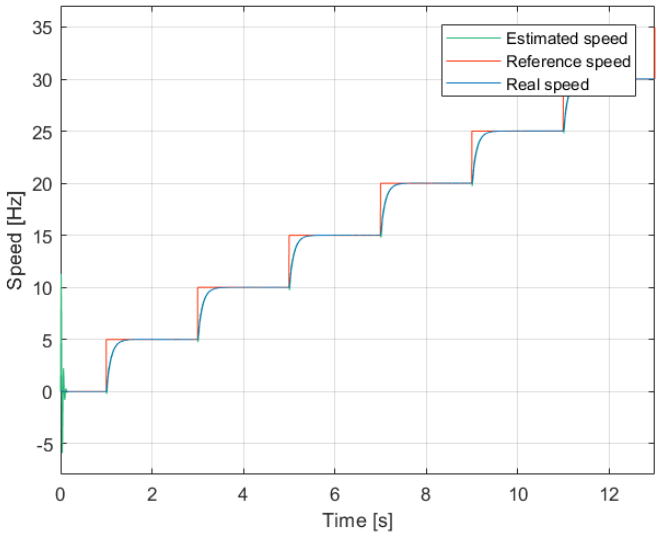

(a) *Overview*

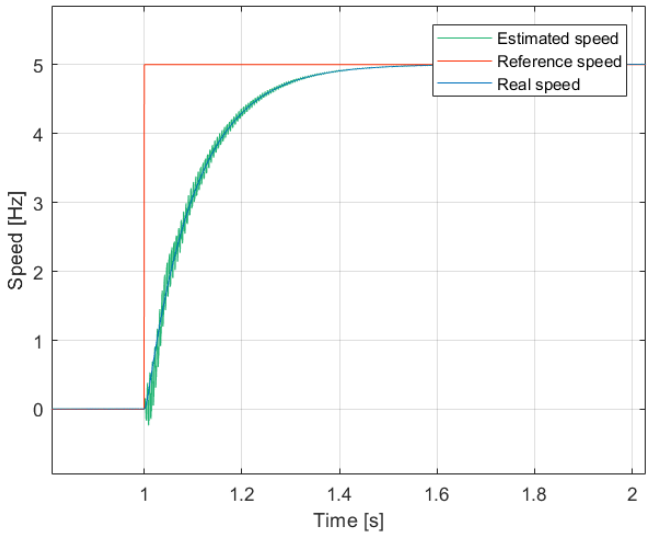

(b) *Transient focus*

Figure 3.15: Speed estimation with HF injection

3.2.4 Sensorless implementation

The above studies have been performed in parallel to a classical control assuming to have a rotational transducer providing the correct informa-

tion about rotor position and speed. The results assessed how the saliency-based estimator manages to correctly retrieve the rotor electrical quantities with low error. Therefore the last step that should be performed is a simulation of the sensorless control over the machine, using the data obtained trough the estimator. To this purpose, the control scheme reported in figure 3.6 has been modified according to sensorless operation and is shown in figure 3.17. By comparison one can notice how the position and speed feedbacks from the motor motel are not used anymore in favor of the newly introduced estimated quantities, thus the currents fed as feedback to the inner loop come from a Park transform over the estimated rotor position. Mind that the control scheme follows a precise temporization:

- At time $t = 0s$ the HF injection is activated and the estimated rotor position is found;
- At time $t = 0.5s$ the estimated rotor position is eventually corrected with the polarity information;
- At time $t = 0.6s$ the speed estimation is switched on;
- At time $t = 1s$ the control is switched on and subsequently any speed-set point can be sent.

This temporization is set for several reasons. Firstly, for the control to not influence the initial angle estimation: if the control was switched on, even with a zero-speed set point, at $t = 0s$, it would regulate the speed of the rotor (not perfectly still due to the HF injection), introducing fundamental currents that might degrade the estimation. Secondly, in order to add the eventual compensation only when both the estimated position and demodulated polarity information are settled. Thirdly, in order to have a precise speed estimation in case a compensation was added to the estimated position due to the polarity identification: since the estimation is performed

by means of a cascade PLL, in case a compensation was added, the error would undergo something similar to the "spike" problem described above; to avoid this the integrator of the PLL is pre-charged to the estimated rotor position and released only when the compensation has been added. This also assures a smooth initial transition for the speed estimation, thanks to the fact that the fictious position is close to the estimated one and big error jumps are avoided. Fourthly, to allow the control to start acting only when all the sensorless-obtained quantities are at steady state and no transient is still active in the machine.

A simulation of the sensorless operation is reported in figure 3.16. It shows how the saliency estimator manages to correctly estimate the position at standstill and in stationary conditions, while it suffers sudden setpoint changes. This also reflects on the speed estimation which is worst during transients. It is important to notice that even very steep ramps are far better that a step change of the setpoint for the sensorless operation of the IPM. Finally, four remarks should be highlighted; at first one should remember that the parameter tuning of the control scheme has not been changed, thus the sensorless control manages to reach the same performances of the "sensored" one. Secondly, the IPM model on which the control is operating also includes the non-linearity of the d-axis inductance, which itself introduces a degradation of the control and the estimation: given that the same pass-band filers employed in the previous simulation are used, one should notice that the position estimation error is slightly larger. This might lead to the choice of an increase of the pass-band towards lower frequencies to decrease the error at higher speeds, but it is not the choice I have followed, rather preferring small errors at standstill. At third, it is important to remark that the tuning of both PLLs have been enlarged in order to be faster during sensorless operation. One should therefore pay attention to not increasing too much the speed of the loops, for not introducing higher order

harmonics which would bring instability into the system.

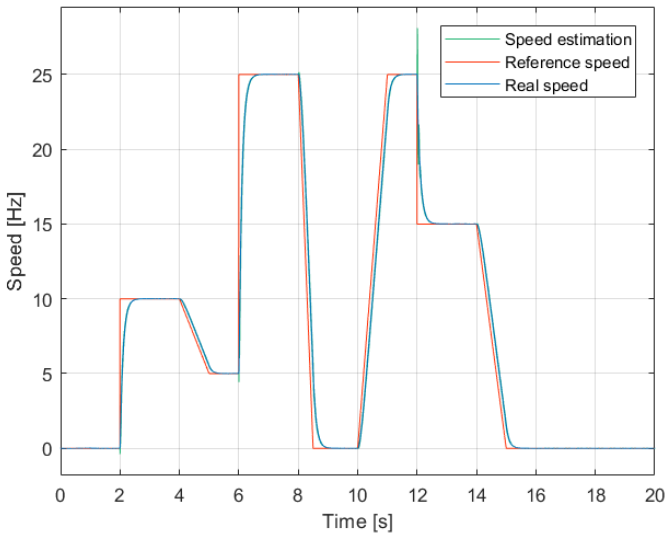

(a) *Speed behavior*

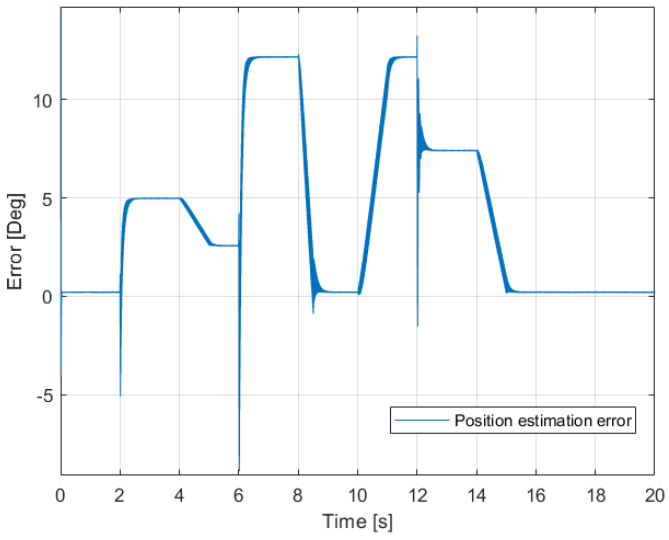

(b) *Position error*

Figure 3.16: Sensorless operation at standstill and low speeds with the saliency estimator

Finally it should be noticed that even trough the outer speed loop has been

de-activated, the inner current loops are active. This means that the current regulators should be tuned to have a pass-band insensitive to the high frequency injection, otherwise they would regulate those currents to 0 introducing small fundamental voltages and currents that may ruin the estimation. In this case the simulation have been ran with those regulators active in order to degrade the estimation on purpose for simulating a "wort-case" scenario in which inverter non-linearities come into play, for assessing the robustness of the estimation method. Of course the estimation could only increase its accuracy if also the inner current loops were deactivated.

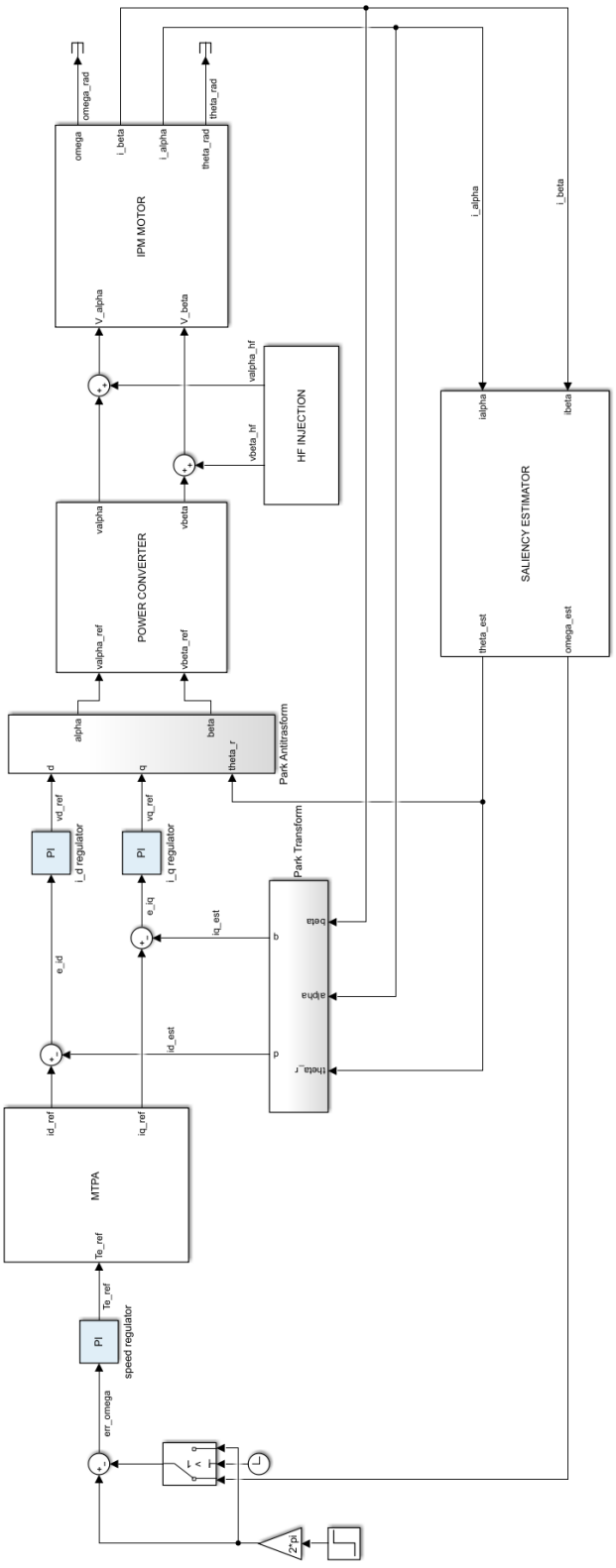

Figure 3.17: Sensorless control scheme

3.3 Sensorless control at medium to high speeds

In this section the algorithm implemented for the identification of the rotor position and speed at medium to high speeds will be developed. The choice fell on the one described in section 2.3.1, and in particular the virtual flux observer depicted in figure 2.9.

3.3.1 Observer design and simulation

The flux observer adopted for retrieving the position of the rotor at medium to high speeds is fed with only stator voltages and currents and can reconstruct the desired information with very good accuracy trough the introduction of a fictious rotor flux. This is built starting from the motor characteristic torque equation and by making use of the $\alpha\beta$ currents transformed onto the estimated dq coordinates. The rotor speed is obtained by triggered discrete time differentiation of the position, with the method described in the previous section to avoid spikes due to the wrapping of the rotor position. The most remarkable thing about this observer is that it makes use of pure integrators in the voltage model to reconstruct the stator flux: this is acceptable in simulation, but one muse recall that a pure integral action is not able to reject the continuous component of a signal with non-zero mean. This could cause a drift of the integral action, especially during the flux-establishing in the machine and during speed transient. To overcome this issue, one could thing on employing a low-pass filter, whose ability to reject the continuous component increases with the increase of its pass-band, but it also introduces delays in the signal processing and limitation in the operational speed-range. Therefore, it has been chosen not to implement a low pass filter at first and go with the pure integrator; to support this choice one should recall that the voltage model containing the integrators is not in open-loop but contains a feedback which should already

help to compensate drifts and offsets. The mentioned feedback is based on a current model of the motor, employing the virtual flux and the estimated rotor position.

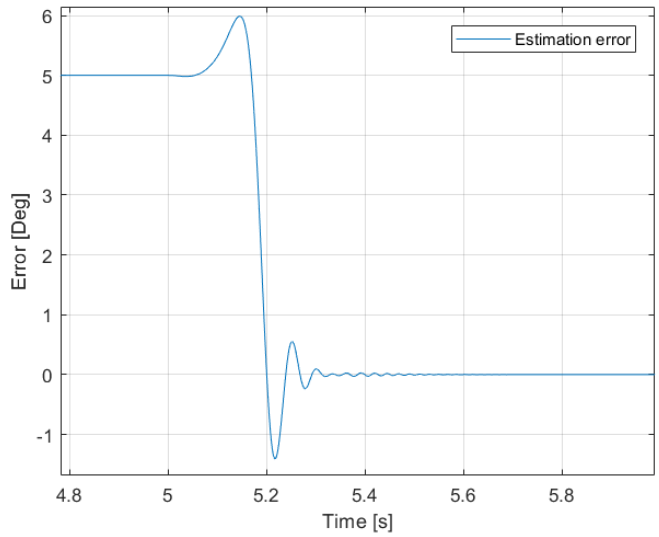

(a) *Position estimation error*

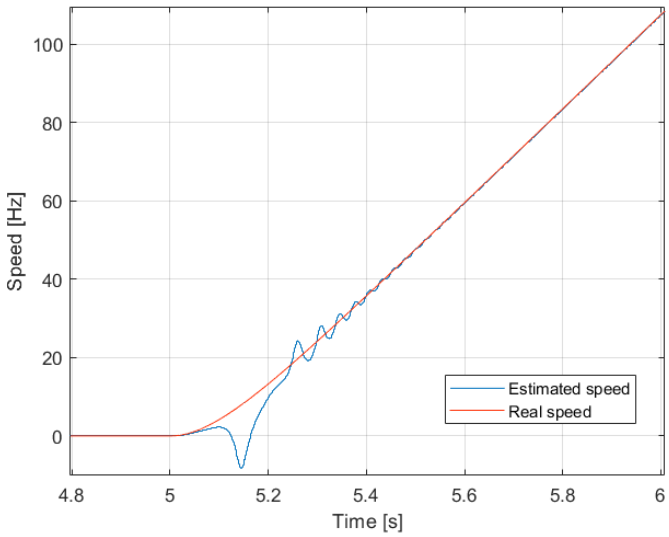

(b) *Speed estimation*

Figure 3.18: Observer behavior without initial position feeding

Since at zero or very low speeds there is barely null magnetization of the rotor, resulting in a very little magnetic flux, the above described observer has no information to work on and is not able to correctly estimate the rotor position. Since the initial estimation is intrinsically 0^o, the observer only works if the real position is aligned to it, which is very unlikely. An example of estimation with a real rotor position different from 0^o is reported in figure 3.18, together with its estimated speed. It is clear how there is an initial transient which causes oscillations in the estimation that take time to vanish. This reflects on the speed estimate which is really poor and cannot be used for a sensorless control below 20Hz. This lower speed limit has been validated by repeating several simulations with different initial angular positions.

It is therefore proven that the usage of an algorithm which provides an initial estimation of the real rotor angle is crucial for the correct operation of this observer. One has therefore two choices: to feed the V-I estimator with the real rotor position or with the estimation coming from the saliency-based algorithm. In order to be coherent with the aim of this theris the first option has been discarded; figure 3.19 shows a simulation in which the rotor position is retrieved at standstill by the saliency estimator and fed to the V-I observer. Then the injection is switched on and the sensored control is activated in order to allow the motor to follow a speed ramp. It is interesting to notice how the flux estimator, which is running in parallel to the control, manages to estimate the rotor position since very low speeds thanks to the initial position feeding.

One can notice from figure 3.19 that the convergence of the observer's estimated position to the initially fed estimation is fast and that the speed estimate is performed with nearly 0 error. Furthermore, the effect of the initial estimation error of the saliency-based observer tends to vanish rapidly as the speed increases, showing an excellent estimation capability of the vir-

tual flux observer. Finally, note that the flux observer estimated position contains an oscillation due to the voltage and current high frequency components, which disappears instantaneously when the injection is turned off.

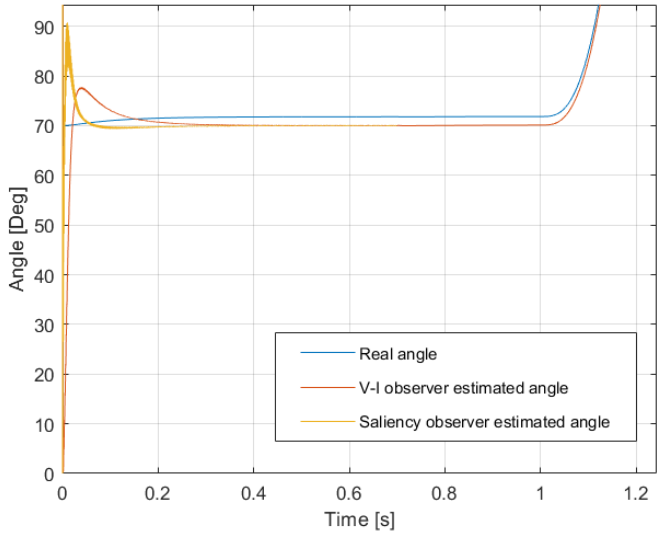

(a) *Angle estimation*

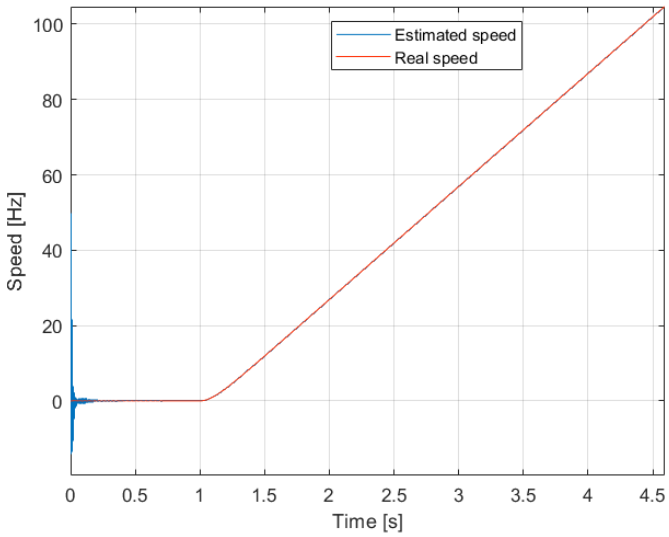

(b) *Speed estimation*

Figure 3.19: Observer behavior with initial position feeding

3.3.2 Sensorless implementation

As done for the saliency-based estimator, also the flux observer has been set up in parallel to a "sensored" control and only consequently implemented sensorless. To make the two estimation methods cohoperate in a sensorless control one has three choices: the first one is to start the machine with the feedback provided by the saliency estimator and wait for the flux observer to reach stability before switching to its estimation; the second is to feed the position estimated at standstill to the flux estimator and operate the sensorless control with the latter since low speeds; the third is to still feed the estimated position from the saliency observer to the flux observer, but to start the machine with the signal injection activated and switch the estimation method "on the run". The first method is of course discarded because its effectiveness, as shown in figure 3.18 is very poor and the switching cannot be performed below 20Hz, rotational speed at which the saliency-based method is already losing efficiency. The second method seems the most attractive due to its simplicity: it is in fact only necessary to find the real rotor position, feed it to the observer at standstill and then run the motor. Anyway, the third one is surely more precise and reliable since at low speeds very little magnetic flux is present and the virtual flux observer, even if aligned with the real rotor position, is not robust and a load applied to the machine could ruin the estimation. In figure 3.20 the behavior of the flux observer fed with an initial position estimation and used for the sensorless feedback is shown. Thus it is here shown only the case of machine started directly with the feedback coming from the flux estimator, since the case of switching "on fly" will be analyzed together with the complete control scheme in the next sections.

The temporization of the scheme is as follows:

- At time $t = 0s$ the HF injection is activated and the estimated rotor position is found; at the same time the estimated position is overwrit-

ten into the flux observer, which starts settling on that;

- At time $t = 0.4s$ the estimated rotor position is eventually corrected with the polarity information;
- At time $t = 0.5s$ the signal injection is de-activated and the overwriting is stop, meaning that the flux observer is now working on its own;
- At time $t = 1s$ the control is switched on and subsequently any speed-set point can be sent.

This is nearly the same described in section 3.2.4 for the operation of the saliency-based estimator from which to retrieve the initial position. Only one temporization is added for overwriting the initial position in the flux observer, which, thanks to the retroaction, settles to a correct estimation. Once this is performed, the overwriting is disabled and the control is switched on from standstill with the only estimation coming from the virtual flux observer. Again, this is not the best achievable operation in terms of robustness but is reported to show that it could work. An improvement will be described in the next section with the correct switching logic between the two estimators. Note that the injection in this case is turned off simultaneously to the end of the position overwriting in order to achieve a less oscillatory position and speed estimation. Figure 3.20 shows the sensorless behavior of the control scheme using the information coming from the virtual flux observer.

As expected no big difference from the "sensored" case are highlighted, since the basic flux observer is well known to provide a very good estimation and the enhancing with the current feedback improves its performances. From figure 3.20(a) it can be noted the effect of the high frequency injection on the estimation, that gets clearer once it is deactivated. The error graph is reported to highlight this phenomenon and the fact that when the control brings the rotor in movement the estimator manages to retrieve the

position with 0 error, even during speed transients.

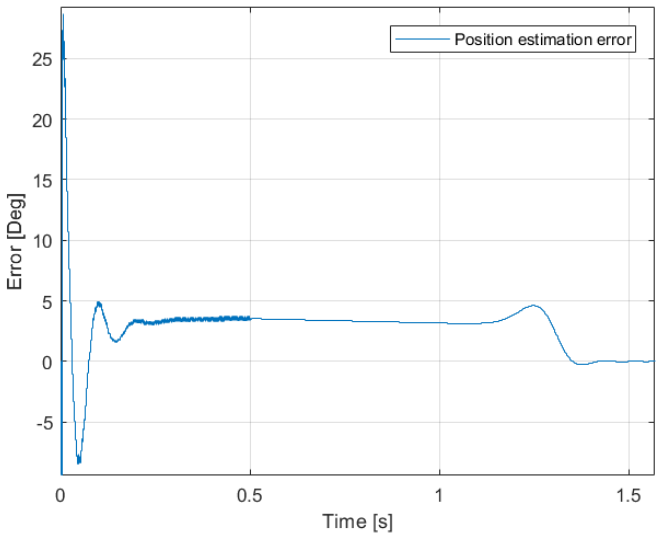

(a) *Angle estimation error (only initial significative segment)*

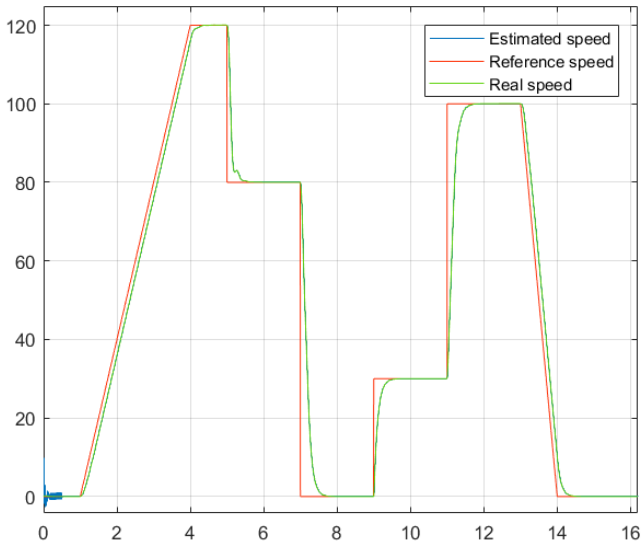

(b) *Speed estimation*

Figure 3.20: Sensorless operation from standstill to high speeds using V-I estimator

From the speed graph one can notice that the estimated speed coincides with the real one perfectly even without using a Kalman filter to retrieve it, but simply differentiating the position information. It is important to highlight that this estimator manages to stick to the correct position and speed even when the latter is decreased back to 0 and successively increased again, making the high frequency injection useful only when it is turned on at first or when some external cause moves the rotor when at standstill.

3.4 Whole speed range sensorless control

After assessing the performance of the two sensorless control methods at different speeds alone, one last step consists in merging the techniques in order to achieve a wide speed range control capable of driving the IPM motor from standstill to the base speed. In order to do so the major critical issues are represented by the transition between the two estimations and the hooking of one estimator to another in not-usage condition. This means that for increasing speed, the flux observer must be initially fed with the position information coming from the saliency observer in order to achieve a correct estimation and a smooth transition. On the other hand, during deceleration transients, the HF-based observer has to re-start working and, due to the stop of HF injection at higher speeds, it is critical for it to correctly retrieve an estimation because of the non-zero speed and the presence of fundamental currents.

As for the first issue, a naïve solution has been implemented: there are two switches that commutate from one estimation to another based on the speed estimation provided by the flux observer. The switching condition is set to be an hysteresis with thresholds 10Hz for acceleration transients and 0.2Hz for deceleration ones. In parallel to this another switch has been introduced with the aim of cutting the signal injection and therefore avoid

useless acoustic noises when unnecessary.

Concerning the overwriting of the initial rotor position into the V-I observer, again a switch has been introduced in order to overwrite the position feedback, which in turn will be translated in a current one, with the correct estimation at standstill. This switch is driven by the speed estimation of the HF-based observer, which commutates from one position to another at a speed of 5Hz. This choice is lead by the fact that, once the flux observer has aligned its estimation with the other estimator and gets unhooked, a transient in position and speed estimation rises because of the different pass-bands employed. Thus, since the speed estimation from the flux observer is the one used to drive the whole switching mechanism, it is left some time to settle before its usage.

As said before, once the rotor speed has gone over 10Hz the HF injection gets cut-off and therefore the estimation provided by the saliency estimator is of any use. When the motor is eventually stopped, the HF injection is reactivated, but due to the presence of fundamental currents and the motion of the rotor, it is hard for the corresponding estimator to retrieve dynamically a correct estimation.

To solve this issue the PLL has been modified as in figure 3.20: a switch

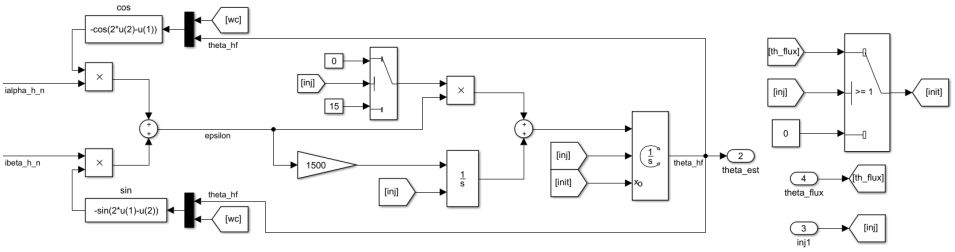

Figure 3.21: Modified PLL for re-hooking the estimation

driven by the presence of the signal injection forces the PI gain to 0 and shuts it off during not-estimating transient for avoiding the residual charging of proportional and integral actions. Furthermore, the integrator pro-

viding the position estimation is set to track the information provided by the flux observer. When the injection is re-activated during deceleration, the initial feedback is the real position of the rotor and the PI starts working without accumulated error.

At last a simulation in which the motor is driven from standstill up to the base speed is reported in figure 3.22. It is shown that the sensorless control manages to follow quite closely a speed setpoint either in increasing and decreasing speed conditions. Furthermore, one can notice that the saliency-based estimator can manage to retrieve the rotor position when it is approaching zero-speeds, thus providing the correct position even when the motor is stopped. The angle estimation error is similar to the one shown in the previous sections when analyzing the two estimators alone.

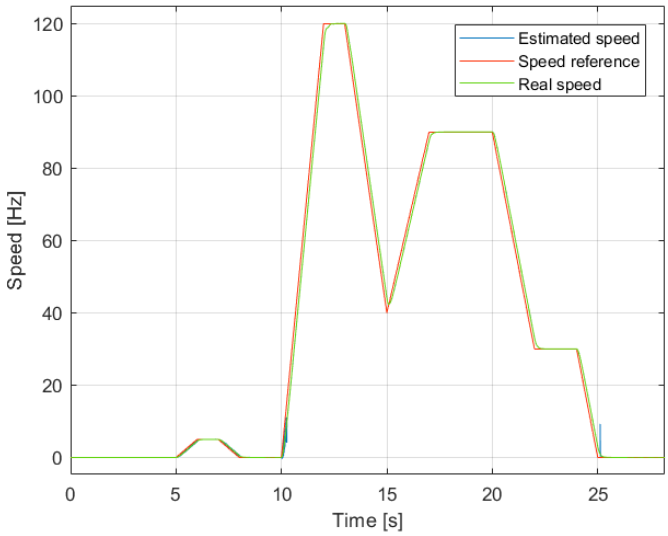

(a) *Speed tracking*

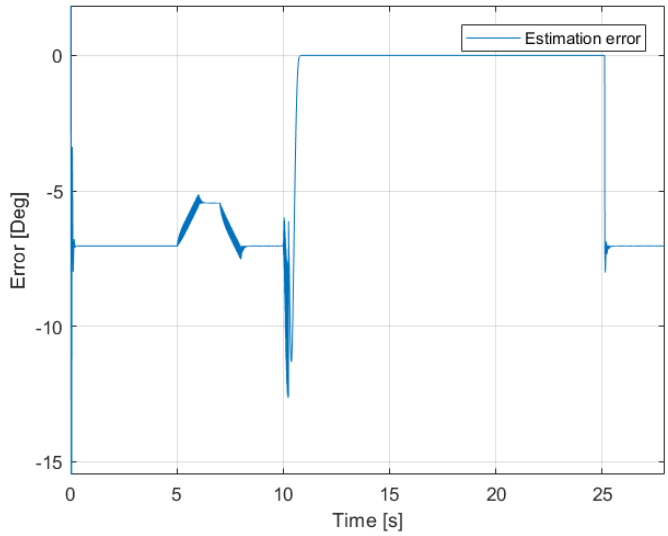

(b) *Angle estimation error*

Figure 3.22: Whole speed range sensorless control

The overall control scheme implementing the described solutions is reported in figure 3.23.

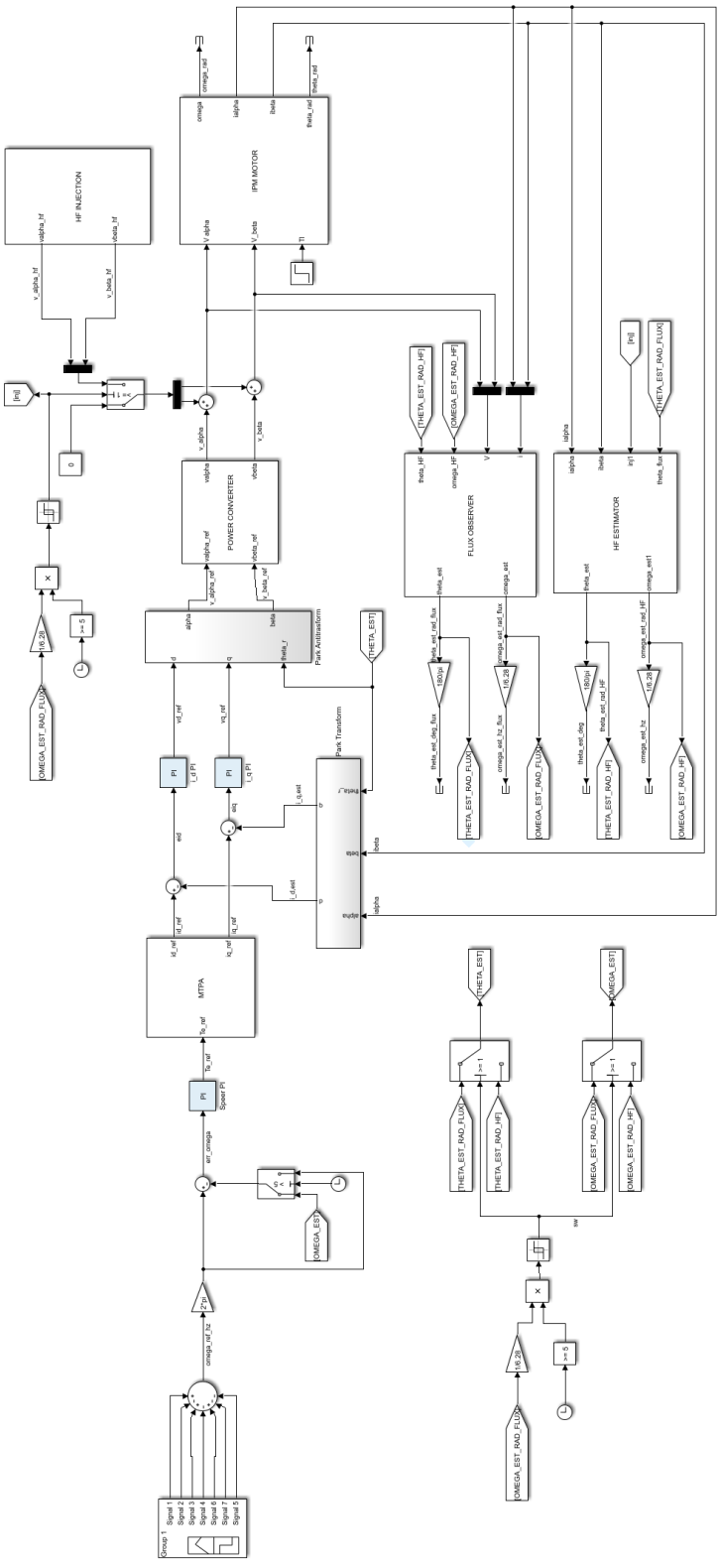

Figure 3.23: Wide speed range sensorless control scheme

Chapter 4

EXPERIMENTAL RESULTS

The aim of this chapter is to describe the setup used for the practical implementation of the sensorless techniques previously simulated, together with a description of the experiments conducted and the results obtained in running a sensorless control over the IPM motor.

4.1 Hardware setup

A schematic representation of the hardware components used to perform experimental verification of the above introduced methods is shown in figure 4.1.

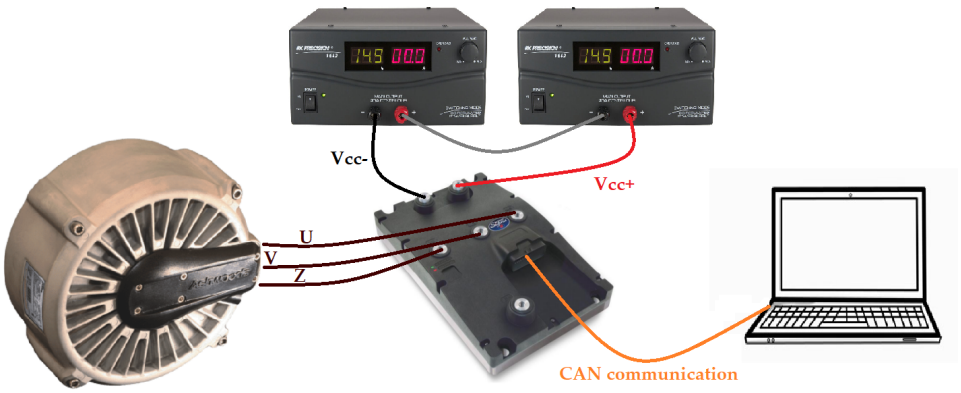

Figure 4.1: Hardware setup functional block diagram

It includes the following items:

- Two 12V, 250A power converters that supply the inverter;
- The SuperSigma2 traction controller by DMC [33], consisting of both programmable software and inverter with rated voltage 48V and maximum current 250A.
- The IPM-L33 motor by Ashwood [34], a three phase synchronous machine with the following characteristics:

Table 4.1: Motor parameters

Symbol	Description	Value
R_s	Winding resistance	8.7[mΩ]
L_d	*d*-axis inductance	100[μH]
L_q	*q*-axis inductance	130[μH]
Ψ_m	Magnetic flux linkage	9.1[V]@1000rpm
V_n	Rated voltage	48[V]
$I_{s,max}$	Maximum phase current	250[A]
ω_{max}	Maximum speed	6000[rpm]
n_p	Number of pole pairs	4
T_n	Rated torque	20[Nm]
T_p	Peak torque	34[Nm]@250A
P_n	Rated power	7[Kw]
P_p	Peak torque	12[Kw]
η	Peak efficiency	94[%]

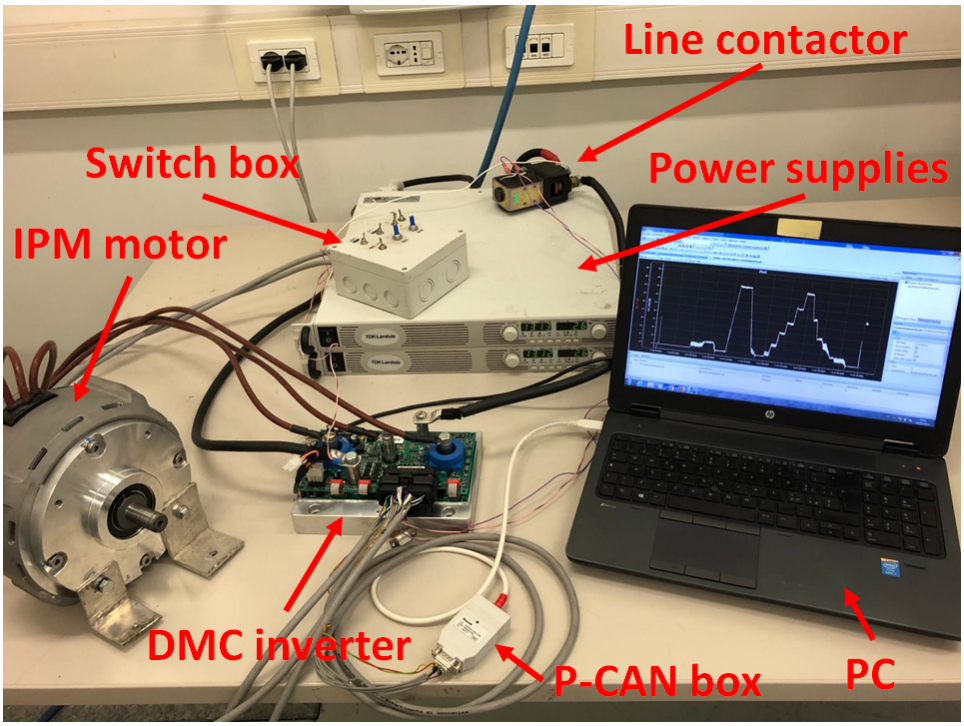

Figure 4.2: Experimental setup

Several considerations have to be done about this configuration and in general about the hardware used. At first one should notice that the power converters employed, even if connected in series, can only provide a 24V supply, thus just half of the motor rated voltage: this means that the range of speed reachable by the machine is strongly limited by this configuration. Also, not being the converters able to absorb power, one should care about the braking stage of the motor, which generates back-currents that drive the converter in protection mode. Secondly, a CAN communication is used to retrieve data out of the control logic: a CAN interface for Windows has been employed, allowing to manage CAN message, quantity scaling and to provide a scope for the acquired data. Those information have been exported trough *.csv* files and elaborated in Matlab environment. Regarding the CAN communication, it must be said that the message rate is set to be $10ms$, thus only allowing to gather slowly varying or continuous signals;

to this means faster signals have been software-stored at the current control loop speed (125μs) and then sent via CAN messages a-posteriori. Third, the programmable logic embedded on the SeperSigma 2 employs a fixed-point microprocessor. This leads to the problem of integer number programming and *per unit* scaling of the variables, on whose a brief overview will be given in the following subsection.

4.1.1 Integer programming and per unit scaling

The problem of integer number programming arises when the microprocessor employed can not handle floating point (or rational) numbers in a sufficiently fast way to guarantee real-time operation. Of course, the floating-point operation can be performed into an initialization phase, but the control loops must be coded with integer number operations. Given that a microprocessor can easily handle 16 bit quantities, one should set a "base number" which corresponds to the unity and retrieve the rational numbers by comparison with this quantity. Usually a power of 2 is chosen as base number to make the handling even faster for the microprocessor. The range and resolution of this transformation are so defined:

$$\mathrm{RANGE} = -\frac{2^{\mathrm{nbit}-1}}{\mathrm{nbase}} \div \frac{2^{\mathrm{nbit}-1}}{\mathrm{nbase}} \qquad \mathrm{RES} = \frac{1}{\mathrm{nbase}} \tag{4.1}$$

for example, if a base number of 2^{14} was chosen, one could represent numbers within the interval $[-2; 2]$ having a resolution of 0.00006104. If one wants to translate a rational number into the fixed-point representing system, it is enough to multiply it by the base number.

Given the above explanation one more problem arises: the range or representation is limited. In fact, with 16 bit one could represent numbers between $[-32768; 32767]$, while with fixed-point scaling the range hugely reduces. To overcome this issue the concept of *per unit* (p.u.) is introduced: the idea behind it consists in scaling all the quantities referring to a base

(maximum) value, in order to come up with rational numbers contained into the range given by the fixed-point scaling. This method has the limitation of not being capable to handle too big quantities with high precision, as the resolution limits the representation accuracy.

4.2 Experimental tests with no load

In order to validate the techniques developed in this thesis the above mentioned hardware setup was used to implement them and draw conclusions on the practical aspects thay may influence the estimation. At first the high frequency voltage injection and the saliency-based estimator have been implemented and let run on they own with the motor at standstill. The next step was to switch on the control and verify if that estimator could provide good results even at low speeds. At third the virtual flux observer was implemented and, fed with the initial real rotor position, was tested to verify if it could provide a good estimation. Finally, the whole-speer range sensorless control has been ran with the knowledge from the previous experiments.

4.2.1 Standstill position estimation with high frequency signal injection

The first step in the implementation of the sensorless control was to add the signal injection. Since the maximum sampling frequency of the ADC available was 8kHz, the maximum injection frequency was set to be 800Hz in order to be able to capture at least 10 point per sinusoid. An increase of the injection frequency above that threshold would mean to poorly reconstruct the generated current, resulting a worst position and speed estimation. To assure a larger margin and a better accuracy, the tests were initially conducted injecting a 10V voltage signal at 400Hz in the synchronous ref-

erence frame. This led to reconstruct the resulting currents with 20 point per period, which was considered enough. A preliminary Fourier analysis was performed to verify that the generated currents are at the expected frequency.

From figure 4.3 it is clear that the high frequency voltage injection produces

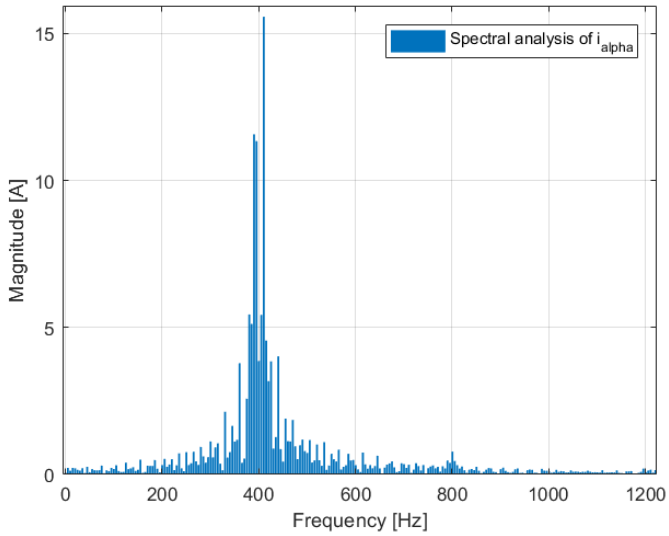

Figure 4.3: Fourier analysis of the α-axis current

the expected results, with the high frequency current that also contains the even order harmonics harmonics produced by the inverter non-linearities and the multiple saliencies phenomenon.

To assess that those high frequency currents actually contain the desired information several experiments were carried out at different rotor position and the results, reported in figure 4.4, show how the phase shift between the α and β currents stretches the current circle towards the real rotor orientation. In view of the polarization signal extraction one should also notice that the produced ellipse is not symmetric with respect to the origin, but points toward the correct d axis.

After verifying that there is actually a signal to be extracted, the demod-

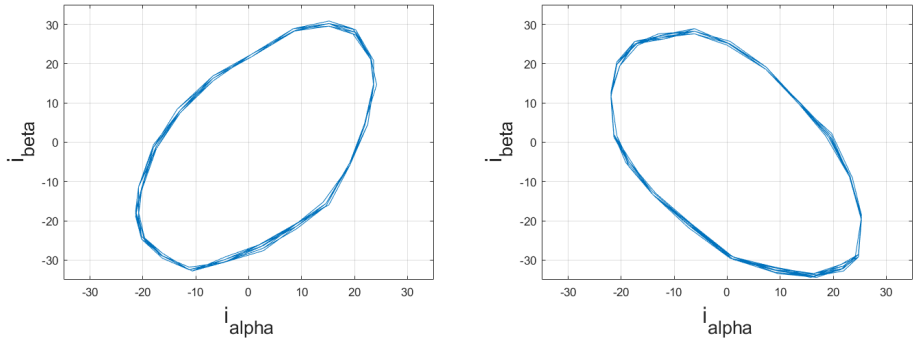

(a) $\theta_o = 65^o$ (b) $\theta_o = 310^o$

Figure 4.4: Current ellipse generated by inductance difference

ulation algorithm described in the previous chapter has been written in C-code onto the microprocessor. All the continuous-time integrators and filters were discretized with the Tustin (trapezoidal) method. At first only the position information without the polarity information was extracted to assess whether the signal at 400Hz was enough to retrieve a low-error position estimation. In the very first version of the algorithm a first order high-pass filter with 50Hz cut-off frequency was used to separate the negative and positive current components. This choice was supported by the Fourier analysis of the currents rotated to a frame synchronous with the signal injection, showed in figure 4.5.

It is evident how, rotating the motor currents to a frame rotating synchronously with the injection, the positive component shifts in DC, while the negative component appears as rotating at two times the injection frequency. Thus, the high-pass filtering of this signal simply consists in removing the current offset. This can be seen in figure 4.6, together with the fact that, since the positive component carries most of the signal's power, once the current is rotated back to a stationary frame its amplitude is noticeably reduced. This supports the injection of a voltage equal to 60% the motor rated voltage: if a lower amplitude signal was injected too little residual

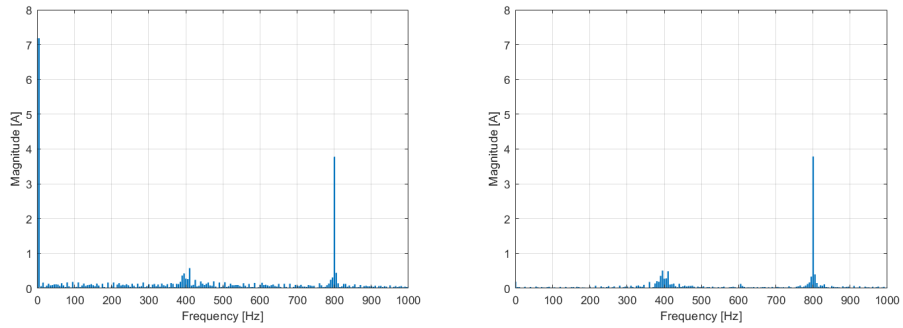

(a) *unfiltered current* (b) *filtered current*

Figure 4.5: Fourier analysis of the α current rotated to a synchronous injection frame

information after the filtering process would be present, resulting in a loss of accuracy of the identification algorithm due to the usage of a fixed-point microprocessor with *per unit* scaling.

At this stage, by means of the demodulation algorithm described in sec-

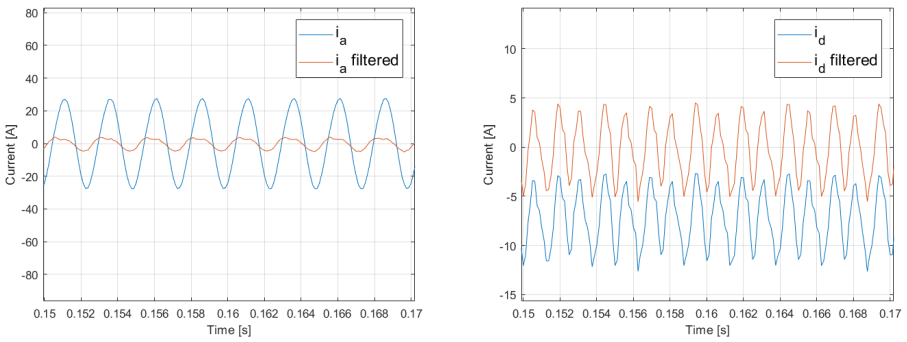

(a) α-*axis current before and after filtering* (b) *d-axis current before and after filtering*

Figure 4.6: Comparison between currents before and after high-pass filtering

tion 2.2.1 and tested in simulation, it was possible to already provide a standstill estimation of the rotor angle. The proportional and integral gains of the PLL were tuned experimentally in order to achieve a satisfying fast response, accepting a small over-elongation and avoiding an oscillating behavior.

Before showing the experimental results, it is worth analyzing also the polarity identification signal, in order to give a complete demonstration of the identification method. Figure 4.7 shows the α axis current rotated to the estimated angle frame, togheter with the resulting polarity signal.

When the estimated angle corresponds to the real one, thus the injection

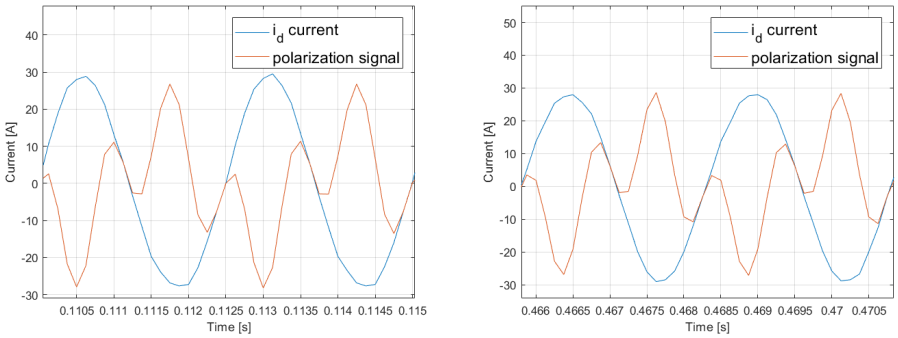

(a) *Correct angle estimation* (b) *Opposite angle estimation*

Figure 4.7: Signal's peak difference in polarity detection procedre

is being performed along the correct d axis, the current has higher positive peaks, while when it is performed on the opposite direction, due to the 180 degrees error, the negative peaks have greater magnitude. This is also highlighted in table 4.2.

Table 4.2: Peak values of figure 2.7

	(a) Correct estimation		*(b) Wrong estimation*	
Signal	**Higher peak**	**Lower peak**	**Higher peak**	**Lower peak**
d-axis current [A]	29.5	-27.6	27.9	-28.9
Polarity signal [A]	26.5	-28	26.5	-28

This is the proof that the signal contains the polarity information. The latter is extracted by highlighting this magnitude difference, multiplying a fictiously generated cosine signal that also inverts the peak magnitude information, and low-pass filtering the resulting sinusoidal waveform: if the filtered signal is negative, the angle has been estimated correctly, otherwise a correction of 180° must be added to the estimation.

Two problems arose with this algorithm; the first one consisted in the us-

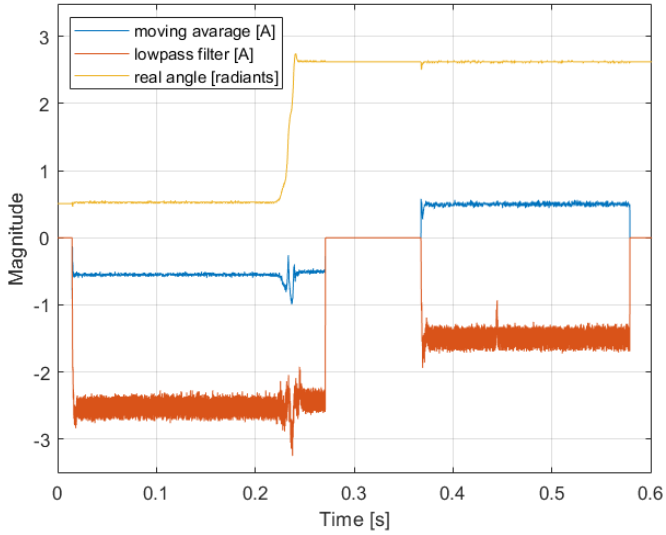

Figure 4.8: Comparison between filtered and moving averaged polarization signal

age of the lowpass filter: since the current at 400Hz is multiplied with a 400Hz cosine signal, the polarization signal travels at a speed of 800Hz and can thus be acquired with only 10 points per period. As it can be seen from figure 4.7, the polarization signal is not very clear and the outcome of the lowpass filter depends on where the samples are taken along the sinusoidal waveform, not resulting in a clear positive/negative separation and pushing towards the introduction of a different dividing threshold. To overcome this issue the filter was substituted with a moving average, which provides a much better separation and takes also less computational requirements.

The second problem consists in the fact that the filtered (or moving averaged) signal is not perfectly stable but undergoes variations when the rotor is moved or when vibrations affect the motor shaft. Since the magnitude of the useful signal, shown in figure 4.8, is very small, its variations are very likely to cause the crossing of the polarity identification threshold, leading to a discontinuous correction of the estimated angle which undergoes jumps of 180°. This problem has been avoided by not giving the estimated angle as feedback to the estimator and endlessly correcting it with the polarization signal but correcting the estimation just once and feed back the compensated estimation to the saliency estimator, which manages to hook on it and provide a correct estimation without further compensation. This method also allows to de-activate the polarity identification algorithm after few instants, leading to a more robust real-time performance.

Finally, the performance of the saliency-based estimator can be seen in figure 4.9: the algorithm manages to retrieve correctly the rotor position in the first and fourth quadrant, while it needs the compensation in the second and third ones. The tests consisted in starting the identification algorithm when the rotor was at 30° and 92°, respectively figure *(a)* and *(b)*, and rotate it by hand counter-clockwise of 360°, before restoring its original position with a clockwise rotation. One can notice that the estimation dynamically follows the rotor orientation with nearly constant estimation error, which is also a good starting point for moving estimation.

Figure 4.10 shows the average estimation error at standstill for two different injection frequencies, 400 and 200Hz. This comparisons is interesting since it highlights the hardware limitation for the estimation: the limited numbers of samples (20 per period in the first case, 40 per period in the second one) and the useful filtered current magnitude resulting form the injection (two times greater in the second case, thus with higher precision in *per unit* handling) make the difference.

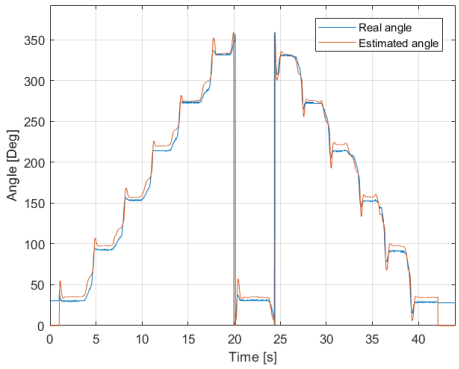

(a) 30° *starting angle*

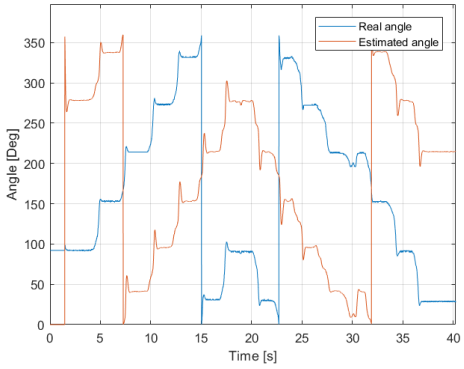

(b) 92° *starting angle, not compensated*

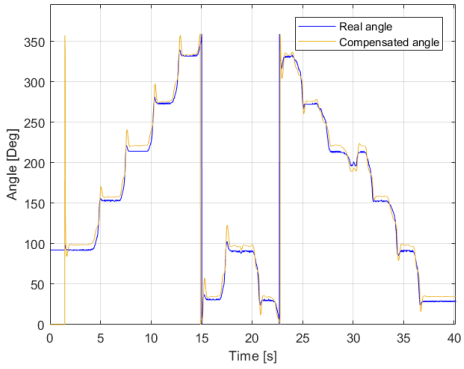

(c) 92° *starting angle, compensated*

Figure 4.9: Estimation of the rotor angle at standstill at different imposed steps; *(a)* without necessity of polarity correction, *(b)* with necessity of polarity correction not performed, *(c)* performed polarity correction

In fact with a 400Hz injection a mean error of 5° is committed, while with a 200Hz injection there is only a mean error of 2°. In the following the 400Hz injection has been employed even if it carries a larger estimation error, because in practical implementation this little error difference doesn't produce a much different control behavior. Furthermore, in view of a moving position estimation, it is better to have a higher frequency injection in order to be able to correctly filter off the fundamental current component, as explained in section 3.2.2.

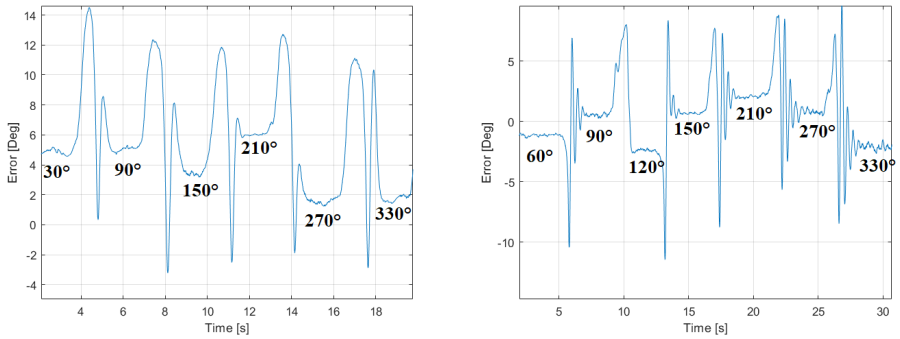

(a) 400Hz *injection* (b) 200Hz *injection*

Figure 4.10: Estimation error for *(a)* 400Hz, *(b)* 200Hz injction at several imposed angular positions

4.2.2 Moving position and speed estimation with high frequency signal injection

Once the position at standstill has been correctly detected, the motor is brought with the sensored control at different rotational speeds to investigate what happens to the position signal. Recall that the polarity has been compensated as feedback when at standstill, thus it will not be investigated anymore, assuming that the algorithm manages to hook on the correct *d*-axis orientation.

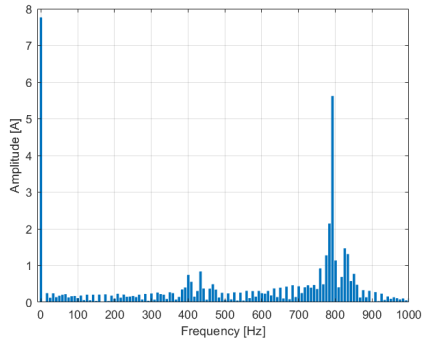

(a) *Spectrum at* 5Hz, 75rpm

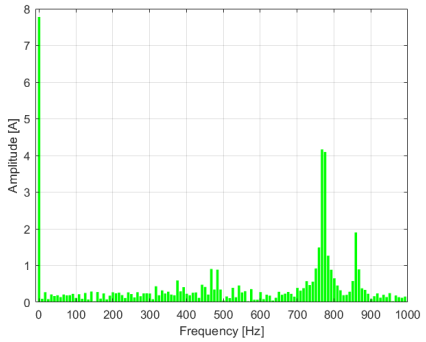

(b) *Spectrum at* 15Hz, 225rpm

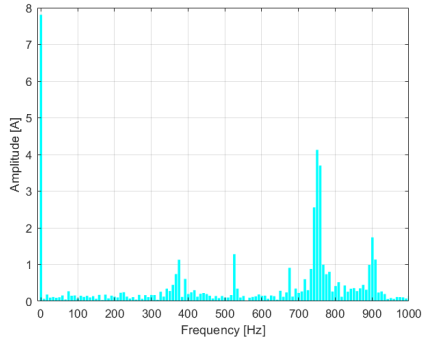

(c) *Spectrum at* 25Hz, 375rpm

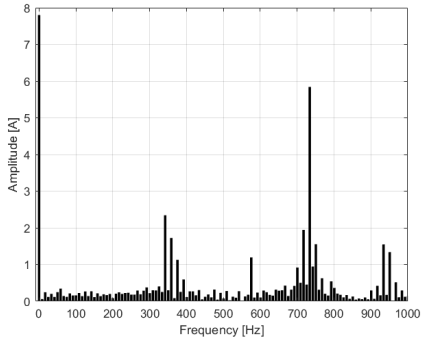

(d) *Spectrum at* 35Hz, 525rpm

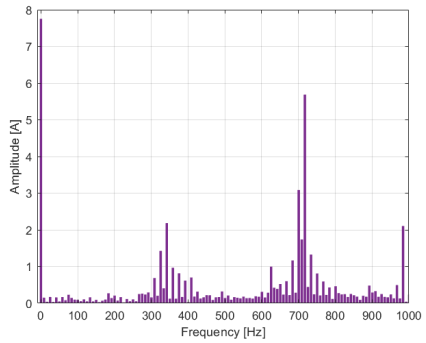

(e) *Spectrum at* 45Hz, 675rpm

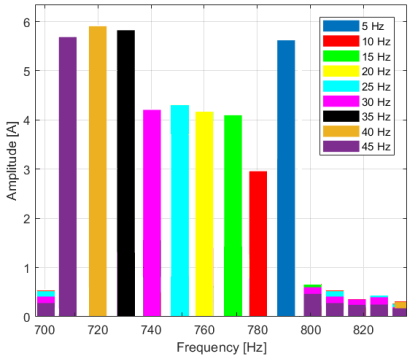

(f) *Focus on negative sequence*

Figure 4.11: Fourier analysis of the α current rotated to a synchronous injection frame for several rotational speeds

A Fourier analysis has been performed once again to verify that the high frequency current, once transformed onto axes rotating at the injection frequency, exhibits the expected frequency components. Figure 4.11 reports the superimposed Fourier analysis for rotating frequency from 5 to 45Hz, from which it is evident that there are three main groups of components; the first one is in DC and corresponds to the positive sequence of the carrier current, the second one is slightly above 400Hz, it is representative of the fundamental currents and rotates at $(\omega_c + \omega_r)$, while the third one is below 800Hz and represents the negative sequence component rotating at $2(\omega_c - \omega_r)$. Of course, there are also harmonics groups at even multiples of the latter component.

It it remarkable to remember that those tests were performed with no load applied to the motor, thus the amplitude of the injected current is much higher that the fundamental. This corresponds to a good estimate because those fundamental components do not bother it. When it will come to loaded experiments it is expected to have a worsening of the estimation because the high-pass filter with cut-off frequency 50Hz employed will not manage to eliminate them.

Anyway, since at the moment the motor is driven with no load, the estimation error, reported in figure 4.12, is barely influenced by this phenomenon, which is slightly visible at rotating frequency of $30 - 45$Hz where, due to the higher torque required to overcome the friction losses, the resulting fundamental currents are slightly higher in magnitude and degrade the estimation.

As for the speed estimation, it has been retrieved by simply differentiating the position signal. Since the outcome contains a lot of noise, it has been low-pass filtered in order for the control to see a more clear feedback signal and avoid as much as possible torque ripple. The problem of the spikes produced by the wrapping method is easily avoidable with the integer pro-

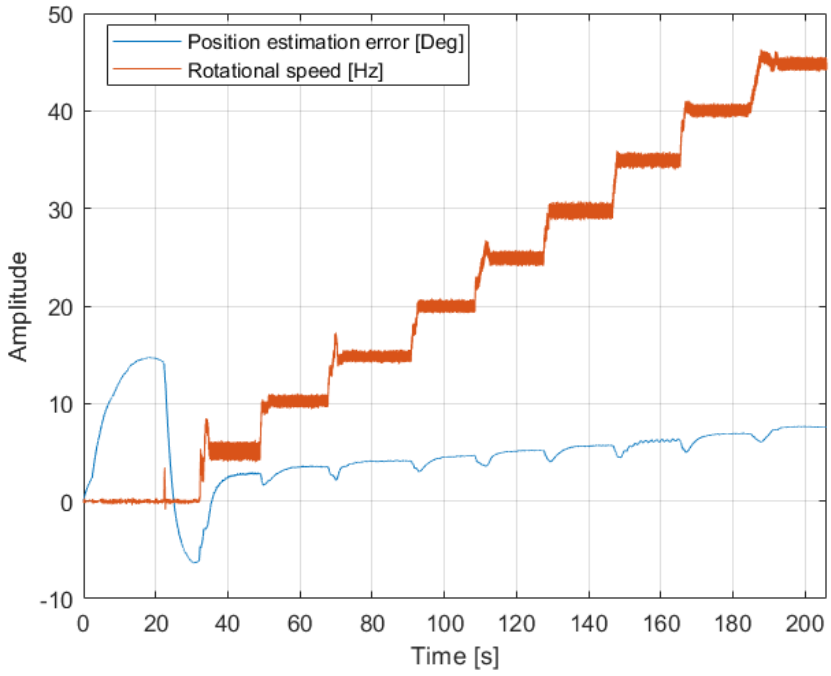

Figure 4.12: Estimation error at increasing speeds

gramming method and *per-unit* scaling.

Sensorless implementation

The conclusion of this set of experiments consists in driving the motor with the position and speed feedback provided by the saliency estimator. To this means the Park transforms make use of the estimated angle, out of which the speed used to close the outer loop is driven. Figure 4.13 shows how the control manages to follow closely a speed setpoint, with a very small position estimation error. The only modification with respect to the sensored control has been the tuning of the PLL's gains, which were increased in order for it to be more reactive to steep increases and decreases of speed. This was balanced by a corresponding increase of the noisiness of the estimation, which was anyway considered acceptable since the control system was made more robust.

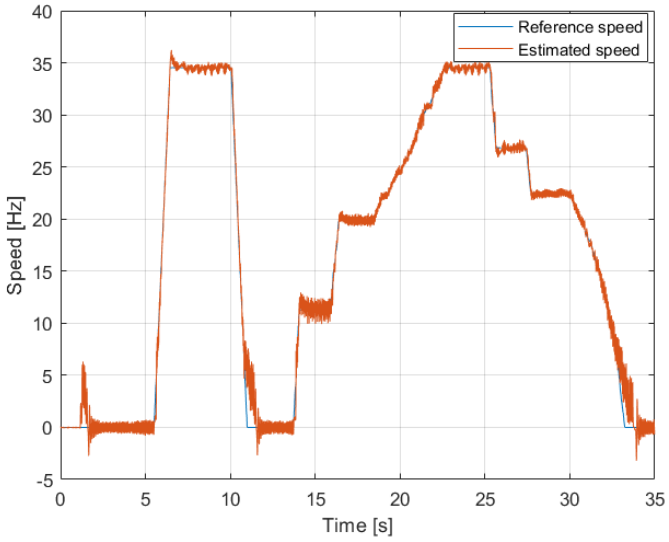

(a) *Sped tracking*

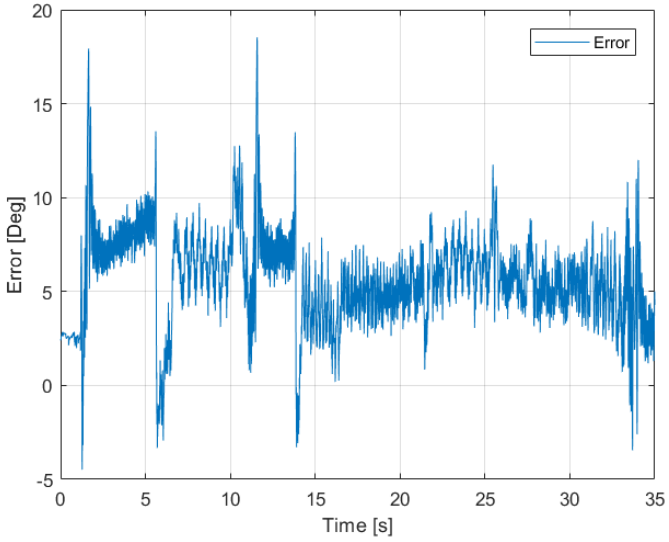

(b) *Position estimation error*

Figure 4.13: Sensorless drive at low speeds using the HF injection based estimator

4.2.3 Position and speed estimation with virtual flux observer

It has been demonstrated that, at least in no-load conditions, the saliency-based estimator can drive the motor without requiring a physical position information. On the other hand, this method produces a very annoying acoustic noise, which is unacceptable for industrial applications. The implementation of the virtual flux observer is then necessary and will be investigated hereafter. Both V-I observers introduced in section 2.3.1 have been tested in order to assess whether one could provide better results that the other. At first the "virtual flux" observer, with the compensation feedback provided by the comparison between the real and reconstructed motor currents was implemented. To assure a stable behavior the current error is only amplified by a proportional gain, since there is another integral action in the flux-model and is well known that two integrators in a loop cause instability. Furthermore, their effect would be to integrate too much the noise introduced by the motor currents, causing a worsening of the estimation. Of course one could think of substituting the integration in the flux-reconstruction model with a low-pass filter, but, since at standstill the current variations are very slow, this would not introduce any improvement unless to set a very low cutting frequency, which would result in having something very similar to the integrator. Concerning the second observer, the one with the corrective feedback provided by the flux comparison, the block scheme of figure 2.10 has been manipulated in order to hide the presence of the integrator. The resulting transfer function reads:

$$\hat{\Psi}_{\alpha\beta} = \frac{s}{s+g}\left(\frac{V_{\alpha\beta} - Ri_{\alpha\beta}}{s}\right) + \frac{g}{s+g}\tilde{\Psi}_{\alpha\beta} \tag{4.2}$$

It can be noticed that the integration of the back-EMF is weighted by an high-pass filter, thus providing a correct estimation at high speeds or during fast transients. On the other hand, the flux reconstructed trough the magnetic model is weighted by a low-pass filter, which assures a correct

compensation at low-speeds, standstill and low-dynamic conditions.
Since neither of the observers can retrieve the correct position at standstill, they are fed with the estimation coming from the saliency estimator, in order to be coherent with the spirit of this thesis. Again a temporization is introduced: when the motor is switched on, the high frequency injection kicks in and the V-I observers are hooked on the estimation provided by the saliency-estimator. After several seconds the injection is deactivated and the V-I observers are left free to estimate the position by themselves. Alternatively, one experiment has been carried out not deactivating the signal injection.

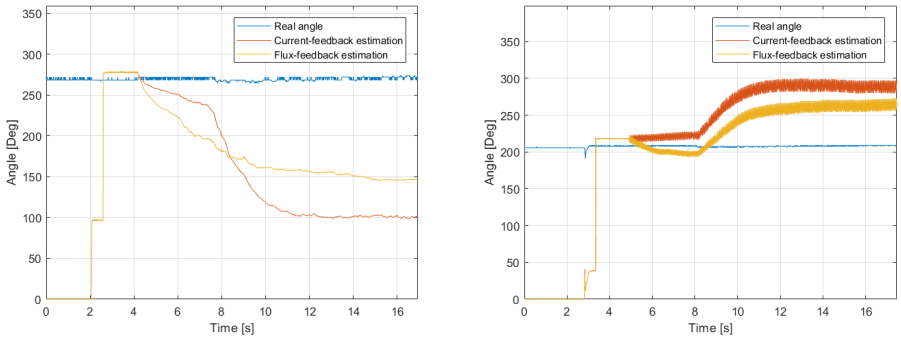

(a) *Unhooking while disactivating injection* (b) *Unhooking with active injection*

Figure 4.14: Standstill estimation comparison between V-I estimators

Results reported in figure 4.14 show as expected that at standstill they cannot stick to the correct angle estimation but slowly drift away because of the integration of the noisy back-EMF. The V-I observer employing the flux feedback manages to provide a better estimation, but this is still insufficient for a sensorless driving of the motor from standstill.
To assess whether they can be used when the rotor is in motion, the sensored control has been re-introduced and the motor is driven at several rotational speeds. Figure 4.15 shows that since there is few movement, and

subsequently some back-EMF, the two observers manage to reconstruct the flux correctly, providing a very good estimation.

This test were carried out with inactive signal injection since it will be used

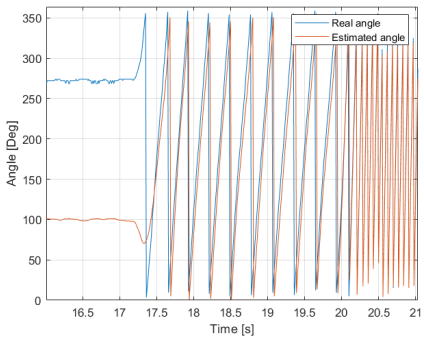

(a) *Estimation from "Current-feedback" V-I estimator*

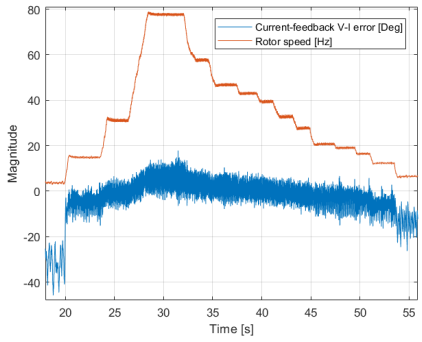

(b) *Associated estimation error at different speeds*

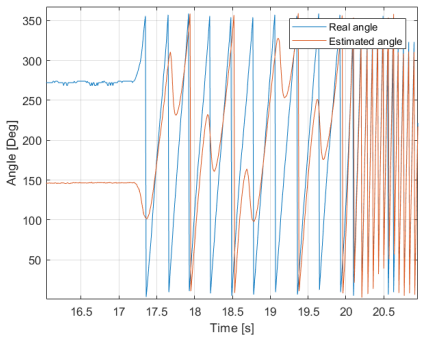

(c) *Estimation from "Flux-feedback" V-I estimator*

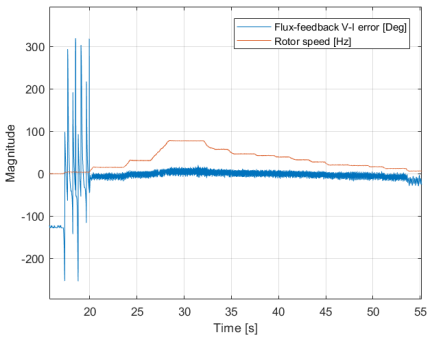

(d) *Associated estimation error at different speeds*

Figure 4.15: Moving estimation comparison between V-I observers

only at standstill and very low speeds (below $5 \div 10$Hz). The mean angle estimation error is found out to oscillate inside the range $[-8; +6]$, which is considered an acceptable result for driving the motor sensorless. It is necessary to remark that the current-feedback observer, employing the pure integration of the back-EMF, manages to retrieve the rotor position, with some error of course, even at very low speeds, while the flux-feedback one

only works above the threshold defined by the filters cutting-frequency. Even though this may seem limiting, the final choice fell on the second observer, since at very low speeds the signal injection will be used. One more test has been performed, consisting in tuning this cutting frequency to very high values close 100Hz: the results showed how in that case the lowpass filtering applied to the reconstructed flux prevails over the highpass filter applied to the integral action, leading the observer to stick on the initially fed position. On the other hand, of course, this high cutting frequency limits the bandwidth of the observer which could only work at very high frequencies. Results are not reported for this since is of any practical use.
Due to the limitation arising at standstill it was not possible to run safe experiments introducing a sensorless control based solely on the flux observers: the control can in fact manage to keep stability only with position estimation errors of 25° at maximum, which the V-I observer cannot guarantee at standstill. The decision thus fell on trusting the results of the sensored experiments and proceed to the whole speed range implementation.

4.2.4 Complete sensorless control

As in simulation the last step consists of merging the two estimation techniques to obtain a sensorless control which can drive the motor from standstill to very high speeds. To this means the issues introduced in section 3.4 were faced in practical implementation. It is actually easier to overcome them when writing C-code because the feedback can be always provided by the position calculated from the V-I oserver. This estimation is overwritten at low speeds with the one coming from the high-frequency injection estimator, with an hysteresis threshold based on the rotational speed. The obtained control scheme has been tested in both low speed operation, threshold crossing in both accelerating and decelerating conditions and high speed operation.

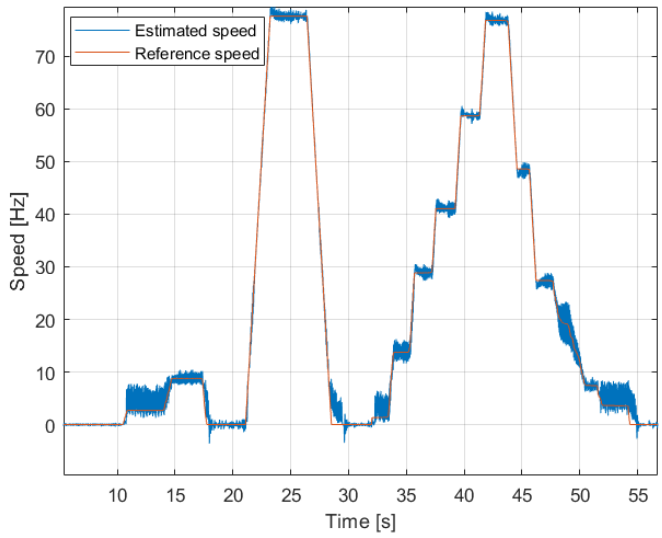

(a) *Speed tracking*

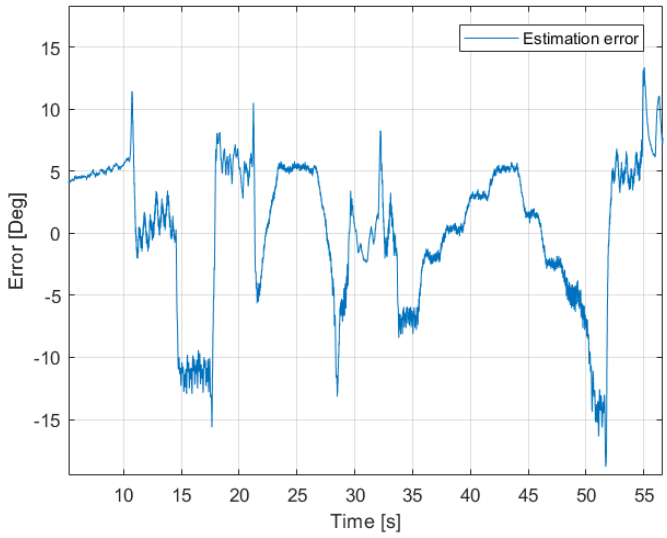

(b) *Angle estimation error at different speeds*

Figure 4.16: Whole speed range sensorless control performance

Furthermore a "start-and-stop" experiment was performed to evaluate the re-hooking performance of the saliency-based estimator. Figure 4.16 shows

the reference speed tracking capability of the whole speed range sensorless control, together with the associated position estimation error.
For this final implementation the "flux-feedback" V-I observer has been used and it is interesting to notice how the position estimation error always stays between the 10° boundaries. This results in a very stable and robust control. Furthermore, since the high-frequency injection is de-activated when the rotor speed goes above 10 Hz, the driving of this motor produces barely null acoustic noise, which is probably one of the critical problem for an industrial application. At last one should notice that when the rotor is being decelerated and the signal injection is re-activated the saliency-based estimator manage to retrieve the correct rotor position with the correct polarity: this means that when the speed is brought back to zero the V-I observer, which would normally loose the position information, gets re-hooked on a correct estimation and can thus be used again for a sensorless control when an acceleration demand is requested by the user.

4.3 Loaded experimental tests

After assessing the behavior of the sensorless control in unloaded conditions, it is fundamental to verify the developed application can robustly provide some torque. To this means the motor is linked to a dynamometer controlled in torque, brought to a certain speed and loaded by increasing the torque setpoint of the brake. Tests have been performed both in the low speed and high speed regions to assess that the sensorless control can robustly operate both under the saliency estimator and the V-I observer. The experimental configuration is shown in figure 4.17.

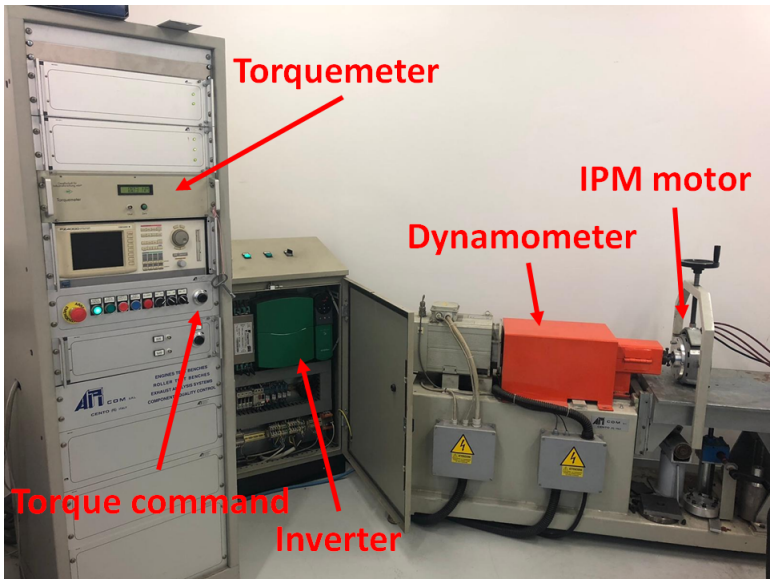

Figure 4.17: Experimental setup for loaded experiments

4.3.1 Low speed loaded experiments

To follow the logic scheme of this thesis the first tests were performed with active high frequency injection and the position estimation was performed by the saliency observer. At first a consideration about the demodulation of the high frequency currents generated should be done: as highlighted in section 4.2.2 the extraction of the useful saliency information contained in the negative sequence current component is done by means of an high-pass filter with a pass-band of 50Hz.

Figure 4.18 shows the spectrum of the current on the α-axis under load conditions rotated to the injection frame. Comparing this spectrum with the one of figure 4.11 it is evident how the fundamental component, located around 400Hz is of highly greater magnitude due to the torque production. It is naïve to understand that the simple high-pass filter employed in unloaded conditions can not manage to filter off that component and that the estimation can not be performed without adjusting the demodulation. To this mean a Butterworth band-pass filter has been designed with passing

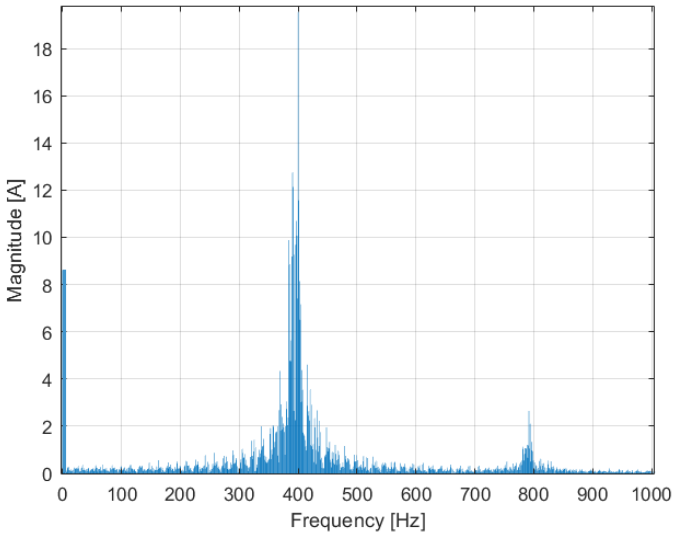

Figure 4.18: Spectrum of the α current rotated to the injection frame under load conditions

bandwidth $740 \div 840$Hz, in order for it to have the best performance at $5 - 10$Hz rotational speed. The bandwidth is very narrow but increasing it is not necessary since the high frequency injection and related estimator should work only at very low speeds. First and second order filters were

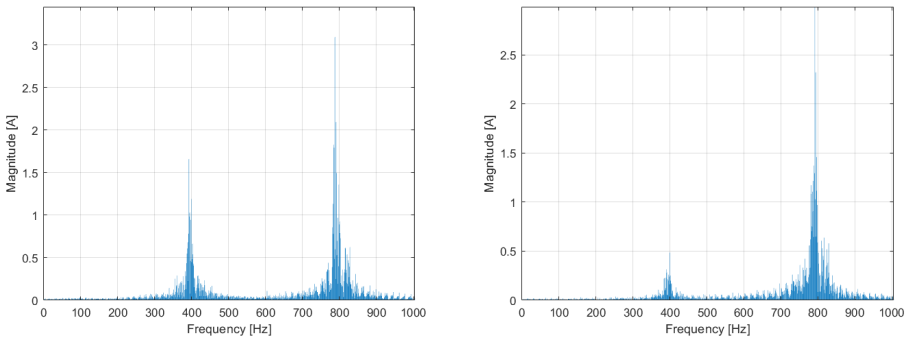

(a) *First order* (b) *Second order*

Figure 4.19: Band pass filters effect comparison

tested at 5Hz rotational speed and the results are shown in figure 4.19: it can be noticed that the fundamental component is highly reduced with

the first order filter, which could already be enough. Employing the second order filter assures an higher system robustness in view of the barely complete fundamental signal elimination: in fact, even if the speed was increased above 30Hz with the negative sequence signal falling out of the pass-band getting attenuated, the fundamental component would be anyway of smaller magnitude and would not ruin the estimation. Figure 4.20 reports the performance of the signal extraction process with the second order band pass filter for a for a rotating speed of 150rpm.

Another criticality of the saliency estimator highlighted by the load ex-

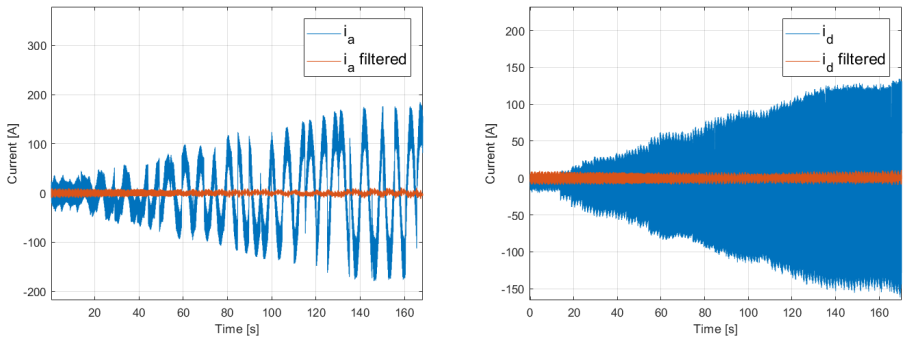

(a) *α-axis current before and after filtering* (b) *d-axis current before and after filtering*

Figure 4.20: Comparison between currents before and after second order band-pass filtering

periments is the PLL performance's dependency on the gains. From the very first experiments, in which an high proportional gain was set, it was noted that the estimator performance was very good at standstill and with small loads, but greatly suffers high loads. This is because the PLL was very "aggressive" with the position estimation, causing sudden upgrades in the angle estimation, which sooner or later would result in a loss of estimation and consequently of the control. To overcome this issue the proportional gain was decreased by one order of magnitude and the estimation resulted smoother at any load, with a little decrease of static performances. Figure

4.21 shows the difference in the estimation for two tests at 5Hz and 14Nm in which the gain was decreased from 1000 to 100. In the first case the estimation is really noisy and the control is lost, while in the second case the estimation is very smooth and the experiment continued up to 20Nm.

Once a satisfying setup was found, four tests were conducted at 5, 10, 20

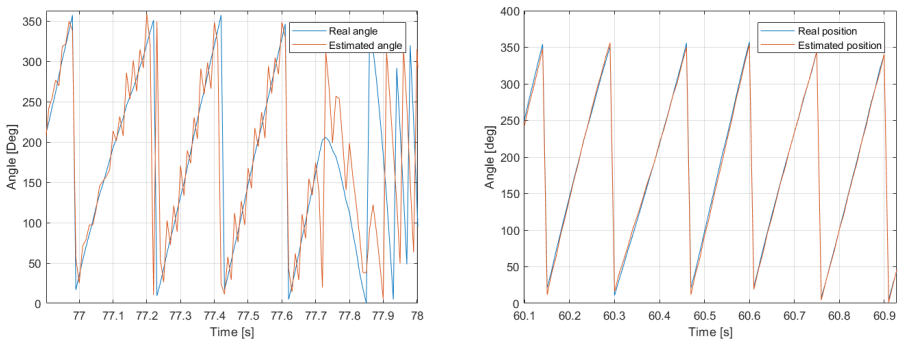

(a) *High proportional action, loss of control* (b) *Small proportional action*

Figure 4.21: Effect of the PLL gain on the angular estimation at 5Hz, 14Nm

and 30Hz (respectively 75, 150, 300 and 450rpm). They were performed by bringing the motor to the desired speed with the developed sensorless speed control and applying a ramp torque with the dynamometer. Results are reported for the 10Hz case in figure 4.22, those for other speeds are the same. They show that the control manages to maintain the reference speed and that it can bear an high resistive torque, up to its nominal value. Finally notice that the angular error is kept very small and only increases when the control is about to lose stability. In the following figures the reconstructed torque is shown because the dynamometer did not allow to export data. Anyway, the real value and the reconstructed ones are very close.

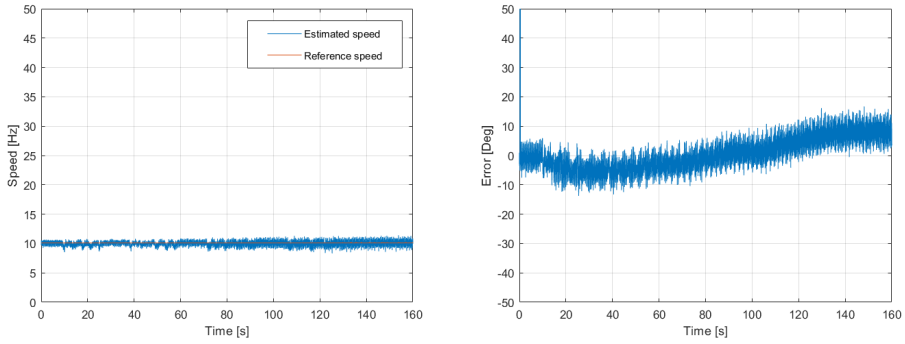

(a) *Speed* (b) *Angular error*

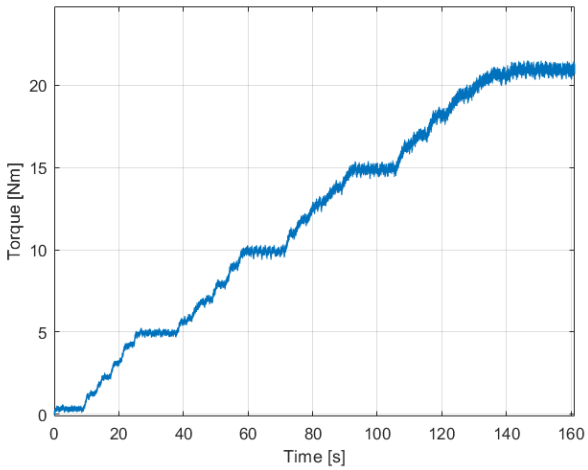

(c) *Torque*

Figure 4.22: Load experiment adopting the saliency estimator at 150rpm with increasing load up to 21Nm

To conclude this set of experiments, the torque production capability at standstill and startup was evaluated. The test consisted in activating the sensorless control with zero reference speed and load the motor with the dynamometer up to 10Nm. Then the sensorless control is used to spin the motor at very low speed and brake it back to zero. Figure 4.23 shows that the experiment succeeded, proving that the sensorless control can provide quite good torque even at standstill.

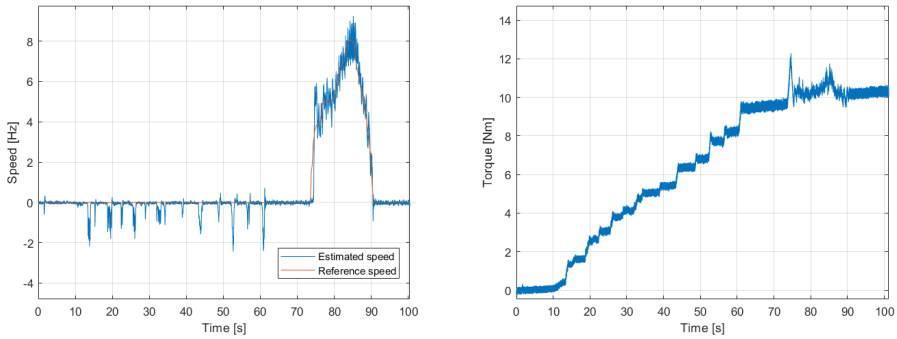

(a) *Speed tracking* (b) *Torque applied*

Figure 4.23: Load test with 10Nm from standstill to 120rpm and back to zero

4.3.2 High speed loaded experiments

At last the V-I observer was tested under load conditions to assess whether the sensorless control could effectively operate in a wide speed range. This set of tests takes into consideration speeds from 10Hz (150rpm) up to 40Hz (600rpm). This range is surely limited by the fact that the motor is fed with a 24V power supply instead of the rated 48V one. As a consequence, the base speed is around 800rpm and the loaded test are conducted below this threshold as the control does not have a flux weakening implemented.
The first experiment has been run under the same condition of the load-free test and failed when the load was at 5Nm. This poor performance was addressed to the parameter dependence of the flux reconstruction and of the magnetic model used as a feedback. In fact those models take into account a constant electrical resistance value, which is known to vary with temperature, further than constant magnetic inductances on the d and q axes. A more accurate test conducted in parallel to this thesis reported how magnetic saturation hugely varies the value of the q-axis inductance, parameter on which the rotor position estimation strongly relies on; its values for dif-

ferent load currents are reported in table 4.3.

Table 4.3: q-axis inductance variation under load conditions

***q*-axis current** [A]	L_q [μH]
3.5	156
15	152
26	150
39	150
51	147
66	141
85	127
109	117
142	104
175	94
193	89

Since the model with constant parameters failed in the flux reconstruction with very low loads, the parameter variation was implemented real time based on the measured current, both in the rotor angle estimation and in the magnetic model. Doing so allowed to achieve far way better performances, such as reaching the motor's rated torque in the whole speed range tested. Mind that the high torque capability of the V-I observer at 10Hz ensures a smooth transition between the two estimation methods even under load. Figure 4.24 shows the torque reconstructed by means of the measured currents and the performance of the estimator, represented by the very small position estimation error and the tight speed setpoint maintenance.

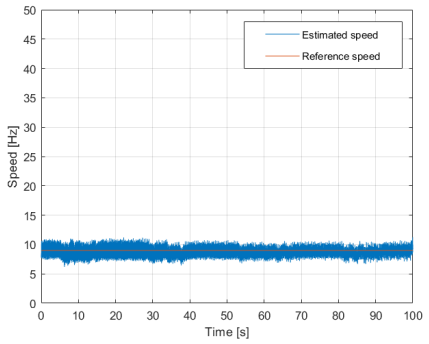

(a) *Speed*

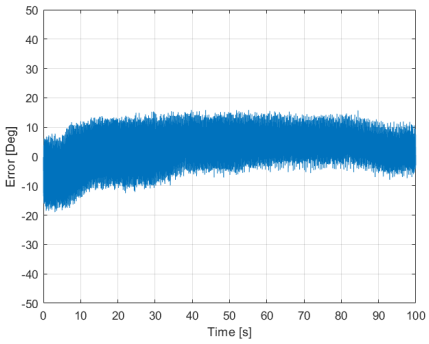

(b) *Angular error*

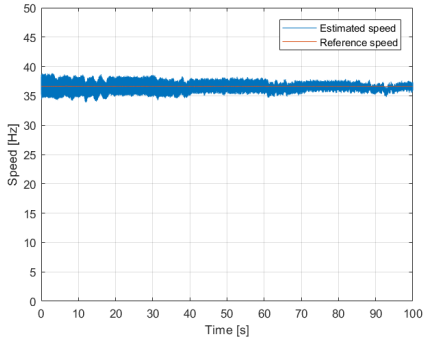

(c) *Speed*

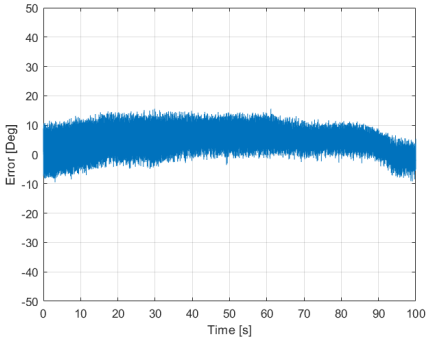

(d) *Angular error*

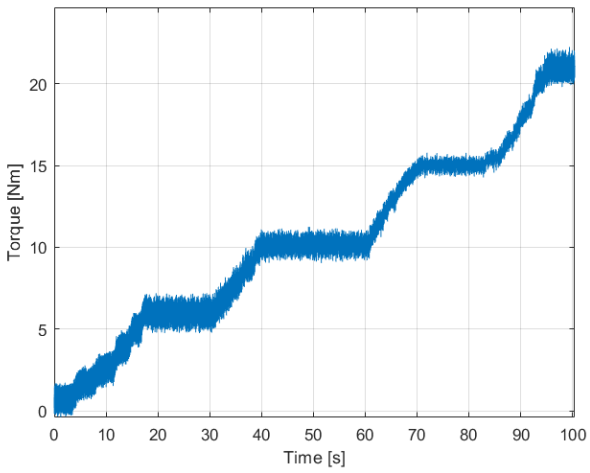

(e) *Torque*

Figure 4.24: Load experiment adopting the V-I estimator at 150rpm (*a* and *b*) and 600rpm (*c* and *d*) with increasing load up to 21Nm

CONCLUSIONS

In this thesis the methods for allowing a sensorless control of an IPM motor have been studied, implemented and experimentally validated. This means that with the developed application it is possible to retrieve the rotor position and speed with the only need of electrical quantities, such voltages applied to the motor and currents generated; the need of any rotational position or speed transducer has been eliminated. This represents a huge advantage in term of space occupied by the motor and motor cost, further than a decrease in system maintenance and longer application life. The techniques developed during this work find their applicability in a wide range of industrial and vehicular applications: hydraulic pumps, marine propulsion, agricultural autonomous vehicles and quadcopters are just few examples of them.

The sensorless drive at medium to high speeds of both Induction Machines and SPM synchronous motors has been widely studies in the past and is a well-known and used technology. Methods for this speed range consist in using either full-order observers based on the complete machine model or simple and more implementable stator flux estimators, which reconstruct the back-EMF to retrieve the rotor position. In this thesis the latter have been further enhanced in order to reconstruct also the rotor flux, which under load conditions differs from the stator one due to the load angle. Furthermore, a feedback in the back-EMF calculation has been introduced for the correction of the well-known drifting problems of the integrators

employed.

Even if the above-mentioned developments are relevant, the major improvement introduced by this thesis is the possibility to retrieve the rotor position at standstill and to drive the motor even at very low or zero speeds. This is possible thanks to an intrinsic characteristic of the IPM motor: the presence of a rotor spatial saliency, meaning that the inductance is different on the rotor axes. This physical characteristic can be exploited with various techniques, such as an high frequency injection of a carrier signal or modification of the basic PWM switching sequence. Since the frequency injection methods seemed the most promising ones, they have been investigated deeply, analyzing the possibility of voltage or current injection on either stationary $(\alpha\beta)$ or rotating (dq) axes frames. Furthermore, the effect of physical non-idealities which could affect the estimation were investigated. The major difference between current and voltage injection is the complexity of the control behind them: in the case of voltage injection, the inverter can directly generate the desired signal, while in case of current injection two regulators should be added to the control scheme to generate the carrier signal. The tuning of the control bandwidth plays a crucial role in both methods: while in the voltage-based one the inner current loops must be kept pretty slow to not regulate to zero the injected signal, in the current-based method the current regulators must be tuned precisely to avoid introducing instability in the control and loss of producible torque. Regarding the kind of injected signal, a sinusoid is generally chosen for simplicity, but square wave-based of impulse-based methods are also present in literature. The last discrimination should be performed on the injection reference frame: if the HF injection is performed on fixed stator axes, the position information will be contained in the phase of the signals coming from the motor since the difference of inductance between the axis will phase modulate them; the injection on a non-stationary reference frame

is generally performed over an estimated direct axis, while the information is contained in the magnitude of the resulting signal in the quadrature one. All those methods suffer of an annoying issue, which is the impossibility to detect the correct rotor orientation; this means that once the angular position has been found there is still an uncertainty of 180^o, given by the symmetry of the rotor. Methods exploiting the presence of permanent magnets were discovered in literature and used to correct the estimation when necessary: they are based on the peak-recognition of the signal generated from the high frequency injection. In fact, since the permanent magnets flux is considered aligned on the *real* direct axis, if a current is injected on that the resulting signal will have greater positive magnitude, while if the signal is injected on the *opposite* direction the generated signal will encounter an obstacle and will have greater negative peaks.

It must be specified that the aim of this development is to create a driving technique which should be scalable, both on the hardware and on the application point of view. This means that the outcome of this work has the aim of being implementable on a large variety or hardware, constraining the computation complexity to be low and the economic requirements for building it very strict. Furthermore, the developed algorithm should work for a very large range of motor sizes, from hundreds of Watt to hundreds of Kilowatts. These constraints perfectly reflect the employed hardware, the SuperSigma2 motion controller by DMC: a low-cost product based on a mosfet inverter and a fixed-point 32 bit microprocessor. Due to the mentioned constraints the application will not have the best obtainable features but will have the great strength to be highly scalable and easily customizable and upgradable.

Given the considerations above, not all the techniques found throughout the literature research have been simulated and implemented. The work particularly focused on an high-frequency sinusoidal voltage injection into

stationary reference frame for standstill or very low speed operation and on a V-I estimator which reconstruct a fictious precise rotor flux with the help of a feedback generated by means of the estimated angle. The methods based on impulse and square wave injection and the ones requiring the modification of the PWM were discarded since they employed several differentiation operations, which contrast with the target hardware performance. Regarding high speed operations, full-order observers were not developed as they rely on a great number of model parameters, hindering the possibility to scale the application on a large variety of motors.

Experimental results performed after the implementation of the above described algorithm show how the sensorless driving of the IPM motor is surely possible even at low speeds: the angular estimation error with the employed configuration (400Hz injection of 60% the motor rated voltage) is bounded in the range $[-10; +10]$ degrees, which is sufficient for providing enough torque for the mentioned applications. The settling time of the algorithm, including the eventual polarity correction, is dependent on the tuning of the Phase Locked Loop employed and has been set to be of few milliseconds. During experimental results it is evident how the estimation behavior is highly dependent on the hardware employed, particularly on the sampling time of the ADC: the 8kHz available only allow the reconstruction of the high frequency signals with 20 points per period, while a higher sampling rate would surely assure better precision and estimation.

Concerning the medium to high speed range, the results obtained from the V-I estimator are very good: it manages to drive the motor until 2000rpm with an angle estimation error in the range $[-5; +5]$ degrees, meaning nearly full torque capability.

Finally, loaded test were performed to assess that the sensorless control can reach the performance of a traditional sensored one. Both the saliency and the V-I estimator manage to provide a really good estimation up to a 20Nm

load, which turns to be motor rated torque production. This result was obtained in a very large speed range, going from standstill to the motor's base speed.

Even if the results obtained were considered very good, there are still a few points which deserve further investigation for this method to be fully reliable and used in industrial applications. Firstly, the speed reconstruction should not be performed anymore with position differentiation, but more sophisticated techniques, like a Kalman Filter should be employed to minimize its variance and thus assure a smoother control action, which would in turn resolve into a longer battery life. Secondly, loaded conditions should be analyzed more carefully since both the saliency-based estimator and the V-I estimator could be made more robust. Static loaded tests have been performed, while dynamic test, such as acceleration and deceleration under load condition should be analyzed deeply.

Bibliography

[1] F. Castelli Dezza, ”Azionamenti brushless_w”, lecture notes, available on http://castellidezza.faculty.polimi.it/wp-content/uploads/Azionamenti-brushless_w.pdf

[2] M. Parisé, ”Electric motor topologies 101”, TM4 blog available on https://www.tm4.com/blog/electric-motor-topologies-101

[3] J. Kang, ”Sensorless control of permanent magnet motors”, Posted from Control engineering magazine Vol. 57 No. 4, April 2010

[4] R. Petrella, "Strategie di controllo del motore brushless", lecture notes, available on http://www.diegm.uniud.it/petrella

[5] D. Raca, P. Garcia, D. Reigosa, F. Briz and R. Lorenz, "A comparative analysis of pulsating vs. rotating vector carrier signal injection-based sensorless control," 2008 Twenty-Third Annual IEEE Applied Power Electronics Conference and Exposition, Austin, TX, 2008, pp. 879-885.

[6] Hyunbae Kim and R. D. Lorenz, "Carrier signal injection based sensorless control methods for IPM synchronous machine drives," Conference Record of the 2004 IEEE Industry Applications Conference, 2004. 39th IAS Annual Meeting., Seattle, WA, USA, 2004, pp. 977-984 vol.2.

[7] C. Caruana, G. M. Asher and M. Sumner, "Performance of HF signal injection techniques for zero-low-frequency vector control of induc-

tion Machines under sensorless conditions," in IEEE Transactions on Industrial Electronics, vol. 53, no. 1, pp. 225-238, Feb. 2006.

[8] L. A. S. Ribeiro, M. W. Degner, F. Briz and R. D. Lorenz, "Comparison of carrier signal voltage and current injection for the estimation of flux angle or rotor position," Conference Record of 1998 IEEE Industry Applications Conference. Thirty-Third IAS Annual Meeting (Cat. No.98CH36242), St. Louis, MO, USA, 1998, pp. 452-459 vol.1.

[9] Shanshan Wu, Yongdong Li and Xuejin Miao, "Comparison of signal injection methods for sensorless control of PMSM at very low speeds," 2007 European Conference on Power Electronics and Applications, Aalborg, 2007, pp. 1-6.

[10] A. Ravikumar Setty, S. Wekhande and K. Chatterjee, "Comparison of high frequency signal injection techniques for rotor position estimation at low speed to standstill of PMSM," 2012 IEEE 5th India International Conference on Power Electronics (IICPE), Delhi, 2012, pp. 1-6.

[11] Y. Yoon and S. Sul, "Sensorless Control for Induction Machines Based on Square-Wave Voltage Injection," in IEEE Transactions on Power Electronics, vol. 29, no. 7, pp. 3637-3645, July 2014.

[12] L. A. S. Ribeiro, M. W. Degner, F. Briz and R. D. Lorenz, "Comparison of carrier signal voltage and current injection for the estimation of flux angle or rotor position," Conference Record of 1998 IEEE Industry Applications Conference. Thirty-Third IAS Annual Meeting (Cat. No.98CH36242), St. Louis, MO, USA, 1998, pp. 452-459 vol.1.

[13] C. Choi and J. Seok, "Compensation of Zero-Current Clamping Effects for Sensorless Drives Based on High-Frequency Signal Injection," Conference Record of the 2006 IEEE Industry Applications Conference Forty-First IAS Annual Meeting, Tampa, FL, 2006, pp. 2466-2471.

[14] J. M. Wang and S. X. Tian, "Analysis of Stator Resistance Effects in Carrier Signal Injection Based Sensorless Control of Permanent Magnet Synchronous Machine", Advanced Materials Research, Vols. 383-390, pp. 5951-5957, 2012

[15] S. Yang, S. Yang and J. Hui Hu, "Design Consideration on the Square-Wave Voltage Injection for Sensorless Drive of Interior Permanent-Magnet Machines," in IEEE Transactions on Industrial Electronics, vol. 64, no. 1, pp. 159-168, Jan. 2017.

[16] G. Zhang, G. Wang and D. Xu, "Saliency-based position sensorless control methods for PMSM drives - A review," in Chinese Journal of Electrical Engineering, vol. 3, no. 2, pp. 14-23, September 2017.

[17] A. Ravikumar Setty, S. Wekhande and K. Chatterjee, "Comparison of high frequency signal injection techniques for rotor position estimation at low speed to standstill of PMSM," 2012 IEEE 5th India International Conference on Power Electronics (IICPE), Delhi, 2012, pp. 1-6.

[18] R. Raute, C. Caruana, J. Cilia, C. S. Staines and M. Summer, "A zero speed operation sensorless PMSM drive without additional test signal injection," 2007 European Conference on Power Electronics and Applications, Aalborg, 2007, pp. 1-10.

[19] Q. Gao, G. M. Asher, M. Sumner and P. Makys, "Position Estimation of AC Machines Over a Wide Frequency Range Based on Space Vector PWM Excitation," in IEEE Transactions on Industry Applications, vol. 43, no. 4, pp. 1001-1011, July-aug. 2007.

[20] Y. Hua, M. Sumner, G. Asher, Q. Gao and K. Saleh, "Improved sensorless control of a permanent magnet machine using fundamental pulse width modulation excitation," in IET Electric Power Applications, vol. 5, no. 4, pp. 359-370, April 2011.

[21] A. Alaei, D. Lee, J. Ahn and S. M. S. Nejad, "Dynamic performance analysis of high frequency signal injection based sensorless methods for IPM synchronous motors," 2018 9th Annual Power Electronics, Drives Systems and Technologies Conference (PEDSTC), Tehran, 2018, pp. 151-156.

[22] P. L. Xu and Z. Q. Zhu, "Comparison of carrier signal injection methods for sensorless control of PMSM drives," 2015 IEEE Energy Conversion Congress and Exposition (ECCE), Montreal, QC, 2015, pp. 5616-5623.

[23] Z. Xu, M. F. Rahman, G. Wang and D. Xu, ”Performance Evaluation of an Integrated Starter-Alternator with an IPM Synchronous Machine under Sensor-less Operation”. Journal of Power Electronics, vol. 12, pp49-57.

[24] G. Foo, S. Sayeef and M. F. Rahman, "Low-Speed and Standstill Operation of a Sensorless Direct Torque and Flux Controlled IPM Synchronous Motor Drive," in IEEE Transactions on Energy Conversion, vol. 25, no. 1, pp. 25-33, March 2010.

[25] F. Parasiliti, R. Petrella and M. Tursini, "Speed sensorless control of an interior PM synchronous motor," Conference Record of the 2002 IEEE Industry Applications Conference. 37th IAS Annual Meeting (Cat. No.02CH37344), Pittsburgh, PA, USA, 2002, pp. 657-664 vol.1.

[26] G. Andreescu, C. I. Pitic, F. Blaabjerg and I. Boldea, "Combined Flux Observer With Signal Injection Enhancement for Wide Speed Range Sensorless Direct Torque Control of IPMSM Drives," in IEEE Transactions on Energy Conversion, vol. 23, no. 2, pp. 393-402, June 2008.

[27] H. A. A. Awan, T. Tuovinen, S. E. Saarakkala and M. Hinkkanen, "Discrete-Time Observer Design for Sensorless Synchronous Motor

Drives," in IEEE Transactions on Industry Applications, vol. 52, no. 5, pp. 3968-3979, Sept.-Oct. 2016.

[28] Jae-Hoon Kim, Sang-soo Lee, Rae-Young Kim and D. Hyun, "A sensorless control using Extended Kalman Filter for an IPM synchronous motor based on an extended rotor flux," IECON 2012 - 38th Annual Conference on IEEE Industrial Electronics Society, Montreal, QC, 2012, pp. 1631-1636.

[29] G. Foo, S. Sayeef and M. F. Rahman, "An Extended Kalman filter for sensorless direct torque controlled IPM synchronous motor drive," 2008 IEEE 2nd International Power and Energy Conference, Johor Bahru, 2008, pp. 271-276.

[30] Yu-seok Jeong, R. D. Lorenz, T. M. Jahns and Seung-Ki Sul, "Initial rotor position estimation of an interior permanent-magnet synchronous machine using carrier-frequency injection methods," in IEEE Transactions on Industry Applications, vol. 41, no. 1, pp. 38-45, Jan.-Feb. 2005.

[31] Dae-Woong Chung, Jun-Koo Kang and Seung-Ki Sul, "Initial rotor position detection of PMSM at standstill without rotational transducer," IEEE International Electric Machines and Drives Conference. IEMDC'99. Proceedings (Cat. No.99EX272), Seattle, WA, USA, 1999, pp. 785-787.

[32] M. L. Bacci, F. furlani, "Interior Permanent Magnet Motors: Parameters Identification and Control", Master Degree thesis for Automation and Control engineering, Politecnico di Milano, A.A. 2015-16.

[33] https://www.dmcde.de

[34] https://ashwoodselectricmotors.com